

Electrical Conductivity of Single Organic Molecules in Ultra High Vacuum



Ellis Pires

Department of Physics and Astronomy

Cardiff University

A thesis submitted for the degree of

Doctor of Philosophy

September 2013

Acknowledgements

Firstly, thanks to my mother, father, and brother for making my formal education possible through their endless practical, financial, and emotional support. For the same reasons, I thank my grandmother and all my extended family, whom I am lucky to have.

I thank my supervisors, Martin Elliott and Emyr Macdonald, for giving me this opportunity and for providing advice and support throughout. Thanks to my friends in the research group; Mark, Samu, Gareth, Neil, Edu, Aathra, Andy, Isam, Watheq, and Rangeen. I also thank my colleagues throughout the department, past and present, for welcoming me as a friend.

Thanks to Matt, Andy, Rohit, and Kye for their continued friendship, and special thanks to Samantha.

Abstract

Measurement of the $I(V)$ characteristics of single molecules is the first step towards the realisation of molecular electronic devices. In this thesis, the electronic transport properties of alkanedithiol (ADT) and alkylthiol-terminated oligothiophene molecules are investigated under ultra high vacuum (UHV) using a scanning tunnelling microscope (STM). Two techniques are employed that rely upon stochastic molecular bridge formation between gold STM tip and substrate; a novel $I(V, s)$ method is proven to be a powerful alternative to the well-known $I(s)$ method. For ADTs, three temperature-independent (180 – 390 K) conduction groups are identified, which arise from different contact-substrate coordination geometries. The anomalous reduction of conductance at small chain lengths reported by other groups for non-UHV conditions is far less pronounced here; all groups closely follow the anticipated exponential decay with chain length, $\beta = (0.80 \pm 0.01) \text{ \AA}^{-1}$, until a small deviation occurs for the shortest molecule. Thus, the likely explanation for the anomalous effect is hydration of thiol groups. The $I(V)$ curves were fitted using a rectangular tunnel barrier model, with parameters in agreement with literature values; $m^* = (0.32 \pm 0.02) m_e$, $\phi = 2 \text{ eV}$. For the oligothiophene molecules, one common temperature-independent (295 – 390 K) conduction group was identified; the conductance decays exponentially with molecular length, with different factors of $\beta = (0.78 \pm 0.15) \text{ \AA}^{-1}$ and $\beta = (0.16 \pm 0.04) \text{ \AA}^{-1}$ for length changes to the alkylthiol chains and thiophene backbone, respectively. An indented tunnel barrier model, anticipated from the physical and electronic structure of the molecules, was applied to fit the measured $I(V)$ curves; $\phi_1 = \phi_3 = 2 \text{ eV}$, $\phi_2 = 1.3 \text{ to } 1.6 \text{ eV}$, $m^* = 0.17 \text{ to } 0.24 m_e$. These UHV measurements provide an important baseline from which to better understand recent reports indicating hydration-dependent, and hydration-induced temperature-dependent, transport properties.

Contents

Contents	i
Publications	iv
1 Introduction	1
1.1 Molecular Electronics	1
1.2 Scanning Probes	2
1.3 Ultra High Vacuum	3
1.4 Thesis Statement	4
2 Theoretical Background	6
2.1 Organic Molecules	6
2.2 Conductance in Mesoscopic Structures	9
2.2.1 Simmons Tunnelling Model	9
2.2.1.1 Image Potential Correction	11
2.2.1.2 Application to Molecular Systems	13
2.2.2 Landauer Transmission Model	15
2.2.2.1 Quantum Scattering Model in 1D	17
2.2.2.2 Single Molecular Level Model	22
2.2.3 Incoherent Transport Mechanisms	25
2.2.3.1 Incoherent tunnelling	25
2.2.3.2 Thermal Hopping	26
2.3 Summary	26

3	Experimental Background	28
3.1	Ultra High Vacuum System	28
3.2	Experimental Preparation	30
3.2.1	Substrate Cleaning	30
3.2.2	Tip Fabrication	31
3.2.3	Molecular Deposition	31
3.3	Scanning Tunnelling Microscopy	32
3.3.1	Scanning Tunnelling Spectroscopy	35
3.3.1.1	Current <i>versus</i> Voltage, $I(V)$	35
3.3.1.2	Current <i>versus</i> Distance, $I(s)$	36
3.3.1.3	Current <i>versus</i> Voltage and Distance, $I(V, s)$	42
3.3.1.4	Current <i>versus</i> Time, $I(t)$	43
3.4	Summary	44
4	Alkanedithiols	45
4.1	Introduction	45
4.1.1	Temperature Dependence	46
4.1.2	Chain Length Dependence	47
4.1.3	Multiple Conduction Groups	48
4.1.4	Summary	51
4.2	Imaging	51
4.3	$I(s)$ Measurements	54
4.3.1	$I(V)$ Characteristics (B Group)	57
4.3.2	Temperature Dependence	62
4.3.3	Chain Length Dependence	62
4.3.4	Break off Distance	65
4.4	$I(V, s)$ Measurements	67
4.5	Discussion	71
4.6	Summary	78
5	Oligothiophenes	80
5.1	Introduction	80
5.1.1	Notable Works	83

CONTENTS

5.1.2	Summary	86
5.2	$I(s)$ Measurements	86
5.2.1	4[T3]4 Characteristics	87
5.2.2	Alkyl Chain Dependence	93
5.2.3	Thiophene Unit Dependence	97
5.2.4	Summary	101
5.3	$I(V, s)$ Measurements	101
5.4	Discussion	105
5.5	Summary	113
6	Conclusions	114
	References	118
	Appendix A	129
	Appendix B	132

Publications

- [i] E. Pires, J. E. Macdonald, M. Elliott, “Chain length and temperature dependence of alkanedithiol molecular conductance under ultra high vacuum”, *Nanoscale*, 5(19), 9397-9403, (2013).
- [ii] A. Vezzoli, I. Grace, E. Pires, S. Higgins, M. Elliott, C. Lambert, R. Nichols, J. E. Macdonald, “Water ‘gates’ both the conductance and the temperature dependence of conductance in single molecule junctions involving oligothiophenes”, Manuscript in progress, (2014).
- [iii] T. Agostinelli, T. Ferenczi, E. Pires, S. Foster, A. Maurano, C. Muller, A. Ballantyne, M. Hampton, S. Lilliu, M. Campoy-Quiles, H. Azimi, M. Morana, D. Bradley, J. Durrant, J. E. Macdonald, N. Stingelin, and J. Nelson, “The role of alkanedithiols in controlling polymer crystallization in small band gap polymer:fullerene solar cells”, *Journal of Polymer Science Part B: Polymer Physics*, 49(10), 717-724, (2011).
- [iv] S. Lilliu, T. Agostinelli, E. Pires, M. Hampton, J. Nelson, and J. E. Macdonald, “Dynamics of crystallization and disorder during annealing of P3HT:PCBM bulk heterojunctions”, *Macromolecules*, 44(8), 2725-2734, (2011).
- [v] A. Guilbert, J. Frost, T. Agostinelli, E. Pires, S. Lilliu, J. E. Macdonald, J. Nelson, “Influence of bridging atom and side chains on the structure and crystallinity of cyclopentadithiophene-benzothiadiazole polymers”, *Chemistry of Materials*, DOI: 10.1021/cm403410w, (2013).

- [vi] S. Lilliu, T. Agostinelli, M. Hampton, [E. Pires](#), J. Nelson, and J. E. Macdonald, “The influence of substrate and top electrode on the crystallization dynamics of P3HT:PCBM blends”, *Energy Procedia*, 31(0), 60-68, (2012).
- [vii] S. Lilliu, T. Agostinelli, E. Verploegen, [E. Pires](#), M. Hampton, M. Al-Hashimi, M. Heeney, M. Toney, J. Nelson, and J. E. Macdonald, “Effects of thermal annealing upon the nanomorphology of P3HS:PCBM blends”, *Macromolecular Rapid Communications*, 32(18), 1454-1460, (2011).
- [viii] T. Agostinelli, S. Lilliu, J. Labram, M. Campoy-Quiles, M. Hampton, [E. Pires](#), J. Rawle, O. Bikondoa, D. Bradley, T. Anthopoulos, J. Nelson, and J. E. Macdonald, “Real-time investigation of crystallization and phase-segregation dynamics in P3HT:PCBM solar cells during thermal annealing”, *Advanced Functional Materials*, 21(9), 1701-1708, (2011).
- [ix] A. Guilbert, L. Reynolds, A. Bruno, A. MacLachlan, S. King, M. Faist, [E. Pires](#), J. E. Macdonald, N. Stingelin, S. Haque, and J. Nelson, “Effect of multiple adduct fullerenes on microstructure and phase behavior of P3HT:fullerene blend films for organic solar cells”, *ACS Nano*, 6(5), 3868-3875, (2012).

Chapter 1

Introduction

1.1 Molecular Electronics

Miniaturisation of electronic components is essential for the continued advancement of technology, and this necessity is driving interest in the field of “molecular electronics” – wherein single molecules are considered for the active and passive components in devices.

Aside from offering electronic components with very small physical dimensions, the field of (organic) molecular electronics is attractive for other reasons. Firstly, an inordinate variety of complex organic molecules with different electronic properties can be devised and synthesised, cheaply, uniformly, and on an industrial scale. Secondly, the phenomenon of molecular self-assembly could potentially be harnessed to readily fabricate highly-ordered molecular devices; this may eventually present an alternative or complementary method to the expensive, problematic, photolithographic silicon-etching techniques currently employed to create transistor arrays. Finally, the properties of certain molecules can change in response to physical, chemical, and biological stimuli; allowing for applications that are not possible with traditional silicon electronics, such as certain types of sensors [1, 2].

Many molecular electronic components have been discussed in the literature;

there are both theoretical proposals and experimental proof of concepts [3, 4]. Important examples of such components include diodes [5, 6], transistors [7–9], and conductance switches for the purposes of memory and logic devices [10–15]. These breakthroughs are important steps toward the realisation of self-contained, stable, potent molecular electronic devices. However, this goal is very distant and there are many basic problems and questions that need to be addressed.

The electronic transport properties for even the simplest molecular systems are still poorly understood; conductance mechanisms need to be identified experimentally, and the effects of subtle changes to variables like chemical structure, molecular conformation, and environmental and interfacial conditions need to be investigated, thoroughly. The measurements then need to be related to rigorously-defined theoretical models. However, coupling a molecule between electrodes in a stable, reproducible manner is no trivial task. Therefore, many experimental methods for molecular conductance measurements are currently stochastic in nature and the results are often difficult to interpret. Hence, there is also a lot of work that needs to be done in the development of novel, reliable measurement techniques.

1.2 Scanning Probes

Scanning probe microscope (SPM) techniques, particularly scanning tunnelling microscopy (STM) and spectroscopy (STS), have become invaluable tools for studying the electronic properties of nanoscale objects. In STM, a conducting atomically sharp tip is brought in close, controlled contact with a conducting sample surface, and the tunnelling current that flows between the two is measured; the current is sensitive to the local density of states in the sample and the tip. The substrate surface and molecules thereon can be imaged, nominally, with atomic resolution, and the electronic properties can be probed (STS).

STM and STS measurements can be performed in a non-invasive manner or, alternatively, it is possible to take measurements after deliberately manipulating target particles; atoms, molecules, nanoparticles *etc.* The latter case is extremely

useful for the development of molecular electronics; if a single molecule is trapped between the tip and the sample surface, then its electronic transport properties between electrodes can be characterised. Since the scanning tunnelling microscope is extremely versatile, this characterisation can be performed under a huge variety of conditions: in different media, such as liquids, gases, and vacuum; at different temperatures and pressures; and with electrodes of differing conducting materials.

The main disadvantages to STM and STS are the necessity that tip and substrate be electrically conducting, as well as sharp and flat, respectively. Moreover, trapping a molecule between the tip and sample is not straight-forward and often requires numerous measurements and a statistical analysis. Nevertheless, the scanning tunnelling microscope remains unrivalled for the purposes of studying single molecule systems.

1.3 Ultra High Vacuum

Ultra high vacuum (UHV) describes the pressure range of roughly 10^{-9} mbar and lower. To achieve and maintain these pressures, even small-volume UHV chambers usually require continuous pumping (for example, by turbomolecular, diffusion, or ion getter pumps) [16]. Moreover, the chambers and components therein must be constructed from materials that have very low vapour pressures, which excludes the use of many plastics and metals and leads to high production and maintenance costs. In UHV, atmospheric contaminants such as water vapour and organic compounds are minimised. Experiments performed under such conditions are extremely important for helping to distinguish the intrinsic properties of a system from those induced by external environmental factors. However, despite their importance, reports in the literature on the electronic transport properties of single molecules under UHV are very scarce. (This is possibly due to the expense and difficulty of building, maintaining, and operating UHV systems.) Thus, there is still much more work that needs to be carried out in this area.

1.4 Thesis Statement

In this thesis, STM point-contact techniques (including a new method) are used under UHV to measure the electronic transport properties of single alkanedithiol and thioester-terminated oligothiophene molecules. Despite the structural simplicity of the former species, there are still open questions that a systematic study under UHV, otherwise absent from the literature, might be able to address. Moreover, the oligothiophenes in question are structurally dependent upon alkane(di)thiols; thus full characterisation of the latter should provide a rigorous basis for studying the former by allowing the transport effects from the non-conjugated and conjugated components to be separated. The electronic transport properties of the oligothiophenes are currently poorly characterised, but some early studies indicate very interesting hydration state, illumination, temperature, and chain length dependences; these characteristics potentially make the molecules viable candidates for single molecule devices and sensors. A systematic study of the electronic transport properties of these molecules under UHV, where the aforementioned environmental variables can be strictly controlled, is essential. (Furthermore, polythiophenes are of significant interest in the field of organic photovoltaics, and therefore characterisation of the transport properties of such monomer units may be instructive in this area.) For both molecular systems, a robust statistical analysis is required to overcome variations in individual molecular measurements.

Chapter 2 outlines the necessary background theory for understanding charge transport through nanoscale systems and Chapter 3 details the relevant experimental measurement procedures employed for these investigations and for other investigations reported in the literature. Chapter 4 expounds the results obtained for the alkanedithiol system; focussing on the dependence of the electronic transport upon molecular chain length, temperature, and contact geometry; and places them in context with regards to other literature studies. Chapter 5 presents the measurements on the oligothiophene system and draws upon Chapters 2 and 4, as well as upon the few reported studies elsewhere, for analysis and interpretation. Furthermore, the results are compared to very recent and interesting measure-

1. INTRODUCTION

ments, under different environmental conditions, conducted by other parties involved in the collaborative research group. Chapter 6 summarises the conclusions of the thesis and discusses important work that needs to be carried out in the future.

Chapter 2

Theoretical Background

In this chapter, the relevant background theory for understanding the experimental results of this thesis is outlined. A short introduction into organic molecules and their electronic structures is presented, before a discussion on the electronic transport models and mechanisms for mesoscopic systems.

2.1 Organic Molecules

The electronic structure of a molecule can be modelled to a first approximation by adopting the linear combination of atomic orbitals (LCAO) approach [17]. Molecular orbitals are found by looking for quantum superpositions of compatible atomic orbitals that are solutions to the Schrödinger equation. Atomic orbitals are assumed to be compatible, and interact significantly, only if they have similar spatial symmetry and energy. They are assumed to interact in only two extreme ways: constructively, when in phase, giving bonding orbitals; and destructively, when out of phase, giving antibonding orbitals. With bonding orbitals, the electron density between nuclei increases, leading to an increased attraction between nuclei and giving the electrons a potential energy lower than that of their separate atomic orbitals. With antibonding orbitals, the opposite case is true, resulting in molecular orbitals with a potential energy higher than those of the constituent atomic orbitals. The number of molecular orbitals is then equal to the number of individual atomic orbitals. These are filled in accordance with Hund's rules

2. THEORETICAL BACKGROUND

up to the highest occupied molecular orbital (HOMO), with the next level up defining the lowest unoccupied molecular orbital (LUMO). The HOMO-LUMO gap is analogous to the band-gap of a bulk semiconductor. The exact energy and spatial distribution of the molecular orbitals (and the size of the HOMO-LUMO gap), depends highly upon the structure of the molecule.

In saturated molecules, like alkanes, each carbon atom forms four sp^3 hybridised σ bonds between neighbours. Electrons are highly localised between atoms such that the bonds are strong *i.e.* the molecular bonding orbital is much deeper in potential energy than the uncoupled sp^3 orbitals (Figure 2.1a). The energy difference between the bonding (σ) and antibonding (σ^*) states is then large, resulting in a large HOMO-LUMO gap. Thus, such molecules should be expected to behave as electrical insulators.

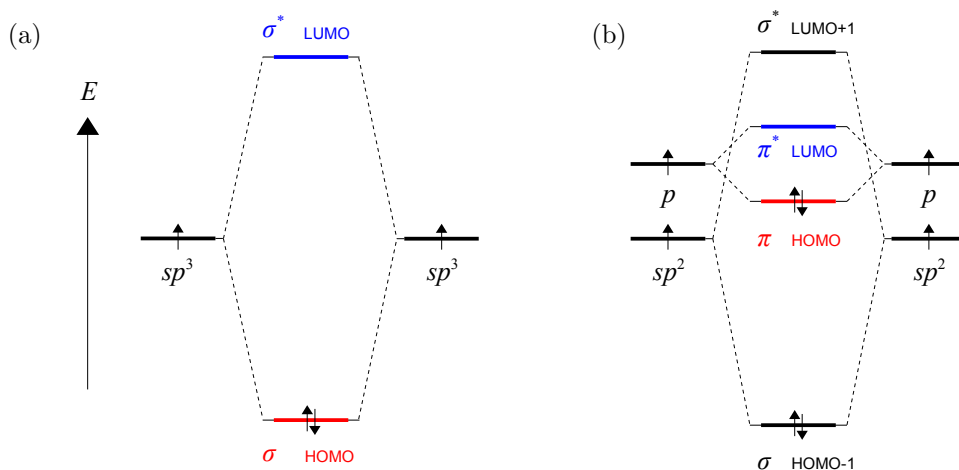


Figure 2.1: A simplified electronic energy level diagram for the molecular orbitals of a) an alkane and b) an alkene. The HOMO-LUMO gap for the alkane is determined by the energy difference between the σ bonding and antibonding (σ^*) states, whereas that for the alkene, with the conjugated system, is determined by the relatively small energy difference between the π bonding and antibonding (π^*) states [17].

With unsaturated molecules, such as alkenes, each carbon atom forms three sp^2 hybridised σ bonds between neighbours in a plane, and one partially filled

2. THEORETICAL BACKGROUND

unhybridised p orbital remains perpendicular to this plane. The latter orbitals overlap with each other above and below the σ bonds forming a connected system of π bonds across the backbone of the molecule, wherein the electrons are delocalised; this is referred to as a conjugated system. The π bonds are weaker than both sp^2 and sp^3 σ bonds, and the energy difference between the bonding and antibonding states (π and π^* , respectively) is much smaller. This relative weakness arises because there is substantially less overlap between component p orbitals due to their out-of-plane orientation. Moreover, the uncoupled p orbitals are higher in potential energy than either uncoupled hybrid orbital. As a result of these two effects, the HOMO and the LUMO for the molecules are defined by the π and π^* orbitals, instead of the σ and σ^* orbitals, respectively. The HOMO-LUMO gap for the molecules is therefore much smaller (Figure 2.1b) than that of their saturated analogues.

By applying the Schrödinger equation to a particle in a one-dimensional box, it can be shown that as the physical extent of a conjugated system increases, the HOMO-LUMO gap size decreases; the energy difference between any two allowed levels, n_i and n_j , for a particle of mass m inside a box of length L is given by

$$\Delta E = \frac{(n_j^2 - n_i^2)\hbar^2\pi^2}{2mL^2}. \quad (2.1)$$

Equation 2.1 suggests that the HOMO-LUMO gap size will approach zero as the box size tends towards infinity. However, in most situations, the equation is an oversimplification. In molecules with significant bond length alternation *e.g.* the single-double bond alternation in alkenes, a periodic perturbing potential must be introduced into the particle in a box model, which results in convergence towards a finite gap size for box sizes approaching infinity (~ 2 eV for polyalkenes) [17, 18]. Molecules with large conjugated systems and small HOMO-LUMO gaps should be expected to be thermodynamically favourable electron conduits, ideal for nanoscale charge transport. Moreover, it has been suggested that electron flow in these conjugated systems can potentially be manipulated by the induction of molecular conformational changes, leading to switches [19].

2.2 Conductance in Mesoscopic Structures

The Simmons tunnelling model [20, 21] and the Landauer transmission formalism [22–24] for nanoscale conductance are discussed in this section. The analytical expressions, derived by Simmons, for the transmission through a rectangular barrier in different voltage regimes; low, intermediate and high, are outlined. Also, the effect of the image potential on a rectangular barrier is discussed, along with the strengths and limitations of the model. The Landauer formalism of transport is outlined, and the quantum mechanical transfer matrix approach to approximating the transmission through an arbitrary shape one-dimensional barrier is discussed. Also, the single molecular energy level model for transmission is outlined. Finally, some incoherent transport mechanisms are discussed.

2.2.1 Simmons Tunnelling Model

This model describes the quantum mechanical tunnelling current density flowing through a thin, one-dimensional barrier, sandwiched between infinite parallel plate metallic electrodes – each with a continuous density of states. The probability, $T(E_s)$, that an incident electron will be transmitted through a barrier of height, $U(s)$, and width at the Fermi level, $\Delta s = s_2 - s_1$, can be described by the widely-used, semi-classical, Wentzel-Kramers-Brillouin (WKB) approximation [20]:

$$T(E_s) = \exp \left\{ -\frac{4\pi}{h} \int_{s_1}^{s_2} [2m_e U(s) - E_s]^{\frac{1}{2}} ds \right\}, \quad (2.2)$$

where $E_s = m_e v_s^2/2$ is the energy component of the electron in the s -direction. Using this as a starting point and by considering the net flux of electrons from one electrode to the other, under an applied bias V , an expression for the current density, J , flowing through the general-shaped barrier, of height above the Fermi level of the electrodes $\phi(s) = U(s) - E_F$, can be shown to be;

2. THEORETICAL BACKGROUND

$$J = J_0 \left\{ \bar{\phi} \exp(-C\bar{\phi}^{\frac{1}{2}}) - (\bar{\phi} + eV) \exp[-C(\bar{\phi} + eV)^{\frac{1}{2}}] \right\}, \quad (2.3)$$

$$J_0 = \frac{e}{2\pi h(\eta\Delta s)^2},$$

$$C = \frac{4\pi\eta\Delta s\alpha(2m_e)^{\frac{1}{2}}}{h},$$

where η is a numerical constant, usually close to unity, arising from integration [20]. This equation can be applied to any shape potential, but uses the average barrier height above the Fermi level, $\bar{\phi}$, to make a rectangular approximation.

Consider the application of Equation 2.3 to an already rectangular potential *i.e.* where $\bar{\phi} = \phi_0$ and $\Delta s = d_0$, at $V = 0$. For low biases only, $V \simeq 0$, the barrier is assumed to be completely undistorted, allowing the approximation;

$$J = \frac{3e^2V\alpha(2m_e\phi_0)^{\frac{1}{2}}}{2h^2d_0} \exp(-\beta d_0), \quad (2.4)$$

$$\beta = \frac{4\pi\alpha(2m_e\phi_0)^{\frac{1}{2}}}{h}.$$

Here, α is a parameter that has been inserted to modify the equation to allow for different charge carrier effective masses; $m^* = \alpha^2 m_e$ [25].

The application of an intermediate bias, $eV < \phi_0$, will raise the Fermi level of one electrode with respect to the other and, assuming the potential is dropped linearly, will distort the rectangular barrier into a trapezoid. The average barrier height can then be approximated as $\bar{\phi} = \phi_0 - eV/2$, but the distortion is not large enough to alter the barrier width at the Fermi level, $\Delta s = d_0$, such that Equation 2.3 can be written as;

2. THEORETICAL BACKGROUND

$$J = \frac{e}{2\pi h(d_0)^2} \left\{ \begin{array}{l} \left(\phi_0 - \frac{eV}{2} \right) \exp \left[-\frac{4\alpha\pi(2m_e)^{\frac{1}{2}}}{h} \left(\phi_0 - \frac{eV}{2} \right)^{\frac{1}{2}} d_0 \right] \\ - \left(\phi_0 + \frac{eV}{2} \right) \exp \left[-\frac{4\alpha\pi(2m_e)^{\frac{1}{2}}}{h} \left(\phi_0 + \frac{eV}{2} \right)^{\frac{1}{2}} d_0 \right] \end{array} \right\}. \quad (2.5)$$

In the high bias regime, $eV > \phi_0$, the trapezoidal distortion is very large, such that the average barrier height can be approximated as $\bar{\phi} = \phi_0/2$. Moreover, the distortion has become so large that it reduces the barrier width at the Fermi level to approximately $\Delta s = (d_0\phi_0)/eV$. Inserting these expressions into Equation 2.3 yields;

$$J = \left(\frac{e^3 V^2}{4\pi h \phi_0 (d_0)^2} \right) \left\{ \begin{array}{l} \exp \left[-\frac{4\pi\alpha(m_e)^{\frac{1}{2}}(\phi_0)^{\frac{3}{2}}d_0}{ehV} \right] \\ - \left(1 + \frac{2eV}{\phi_0} \right) \exp \left[-\frac{4\pi\alpha(m_e)^{\frac{1}{2}}(\phi_0)^{\frac{3}{2}}d_0}{ehV} \left(1 + \frac{2eV}{\phi_0} \right)^{\frac{1}{2}} \right] \end{array} \right\}. \quad (2.6)$$

This case is referred to as field emission or Fowler-Nordheim tunnelling; where the high electric field enhances the tunnelling rate, such that it ceases to scale linearly with applied bias. If the bias becomes very high, $eV > (\phi_0 + E_F)$, then the second term in Equation 2.6 can be neglected.

2.2.1.1 Image Potential Correction

The image potential is the electrostatic potential experienced by a charge due to the polarisation it induces on the surface of a conductor. This effect can be very important when performing scanning probe measurements, particularly when the tip is close to the surface and tunnelling barriers are narrow. The image potential will reduce the average height and width of a rectangular tunnelling barrier by rounding off the edges, as illustrated in Figure 2.2. The new potential profile can be modelled fairly accurately by a simple hyperbolic function [20, 21, 26, 27];

2. THEORETICAL BACKGROUND

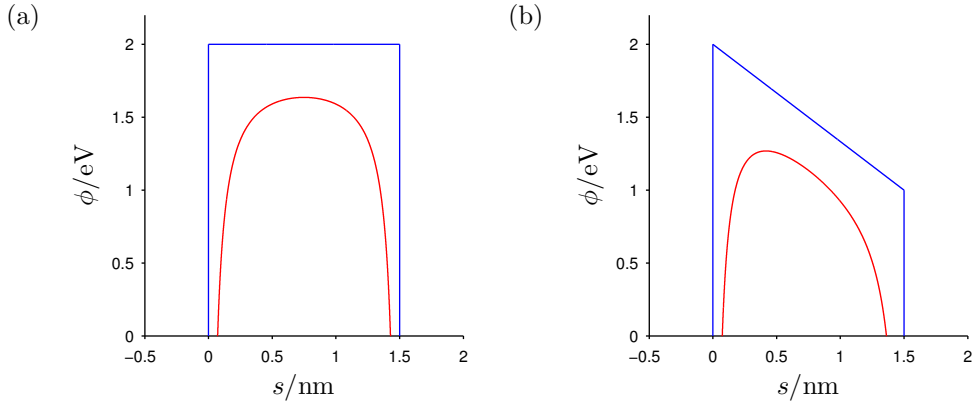


Figure 2.2: a) The blue line shows a rectangular tunnelling barrier, of height 2 eV and width 1.5 nm, under zero applied bias. The red line shows the barrier after it has been corrected to account for the effects of the image potential, according to Equation 2.7. b) The same situation as a), except the barriers are under an applied bias of 1 V. The image potential reduces the average height and width of the barriers.

$$\phi(s) = \phi_0 - \frac{eVs}{d_0} - \frac{1.15k(d_0)^2}{s(d_0 - s)}, \quad (2.7)$$

$$k = \frac{e^2 \ln 2}{16\pi\epsilon_0\epsilon_r d_0}.$$

As mentioned in Section 2.2.1, this potential must be approximated to a rectangular barrier. This can be achieved by integrating Equation 2.7 between the limits of the barrier at the Fermi level (s_1 and s_2), and subsequently dividing the result by the width of the barrier at the Fermi level ($\Delta s = s_2 - s_1$);

$$\bar{\phi} = \phi_0 - eV \frac{s_1 + s_2}{2d_0} - \left[1.15k \frac{d_0}{s_2 - s_1} \right] \ln \left[\frac{s_2(d_0 - s_1)}{s_1(d_0 - s_2)} \right]. \quad (2.8)$$

The limits s_1 and s_2 can be obtained by finding the real roots of Equation 2.7. These can be approximated as [20];

2. THEORETICAL BACKGROUND

$$s_1 = \frac{1.2kd_0}{\phi_0}, \quad (2.9)$$

$$s_2 = \begin{cases} d_0 \left[1 - \frac{9.2k}{3\phi_0 + 4k - 2eV} \right] + s_1; & eV < \phi_0, \\ d_0 \left[\frac{\phi_0 - 5.6k}{eV} \right]; & eV > \phi_0. \end{cases} \quad (2.10)$$

Equations 2.8, 2.9, and 2.10 can now be substituted into Equation 2.3, using the appropriate expression for s_2 given the bias regime, to produce expressions for the current density through a rectangular barrier that include the effects of the image potential. It should be noted that this is a static, as opposed to a dynamic, image potential model. It can be considered valid for systems where the electron plasma frequency in the electrodes is large compared to the inverse tunnelling times of the charges, such that the electron plasma can respond to polarisations very quickly *e.g.* Au-alkanedithiol-Au [28].

2.2.1.2 Application to Molecular Systems

It should be anticipated that the Simmons model is only valid for describing molecular bridge systems in which the dominant transport mechanism is coherent tunnelling. In this process, tunnelling occurs in one step (the charges are never localised on the bridge) and the phase of the charge wavefunction before the event is related to the phase after the event. This form of tunnelling is likely to be the case for systems involving large band gap molecules, where the molecular energy levels are far removed from the Fermi level of the electrodes. In such cases, the average barrier height, $\bar{\phi}$, determined from fitting $I(V)$ curves with Equation 2.3, might be interpreted as a measurement of the distance in energy to the nearest current mediating molecular orbital; the HOMO or LUMO, depending upon electron or hole transport, respectively. However, the rectangular approximation hides details of the molecular electronic structure and is likely to be unrealistic in many cases.

Presumably, the barrier width, d_0 , should correspond to the length of the

2. THEORETICAL BACKGROUND

molecule, or to a close approximation thereof, depending on the setup geometry. Equation 2.4 suggests an exponential decay in current with barrier width; $I \approx I_0 \exp(-\beta d_0)$, where the decay constant, β , is proportional to the square root of the barrier height, ϕ_0 . This decay constant is used widely to characterise tunnelling systems. Interestingly, for molecular bridges with large HOMO-LUMO gaps (5 – 10 eV), the tunnelling is often much more far reaching, with experimentally observed values of β being much smaller than predicted by this model [29, 30]. The discrepancy is often explained by invoking the phenomenon of “superexchange” – in which the electronic structure of a molecule somehow mediates and enhances tunnelling rates, despite the charges never being localised in the molecular states [31, 32]. Even with superexchange, coherent tunnelling will usually only contribute significant amounts to the current if the bridge is very small (< 3 nm) [33]. The transport should be temperature-independent to a first order approximation, but a temperature dependence can still be observed in certain systems due to temperature-dependent distributions of molecular conformers [34] or from the temperature-dependent Fermi-Dirac distributions.

The model has a further shortcoming when applied to single molecule bridges insofar as it describes the current density flowing through a planar system; an effective area must be considered in order to obtain absolute current values. It is not immediately obvious what the “area” of a molecule between electrodes means physically, and whether the assumptions made in the model still hold for these nanoscale dimensions. Therefore, the relation may be expected to be better oriented towards describing single monolayer, rather than single molecule, systems. Furthermore, there is evidence that suggests Equation 2.3 begins to break down for narrow barriers (< 2 nm) or low electrode work functions [26]. Also, the validity of approximating the numerical correction factor, η , to unity has been questioned [26].

In short, the Simmons relations may give a good quantitative agreement with experimental results in some cases but, in general, a more rigorous, fully quantum mechanical model is required for describing conduction through molecular systems.

2. THEORETICAL BACKGROUND

2.2.2 Landauer Transmission Model

In this formalism, the conductance of a mesoscopic object is modelled by considering the transmission arising from the coherent scattering across it. Consider a quasi one-dimensional object connected to two large perfectly metallic reservoirs via two narrow ballistically conducting leads; Figure 2.3.

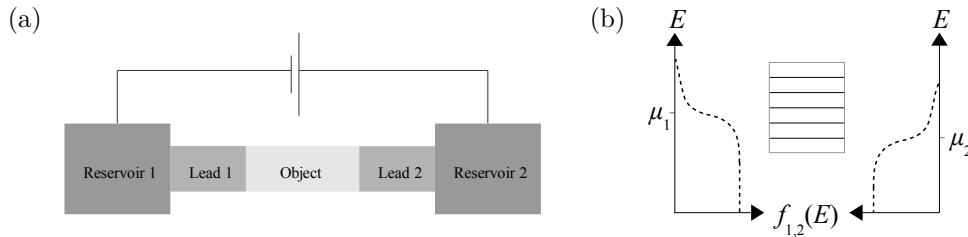


Figure 2.3: a) A quasi one dimensional object connected to two large metallic reservoirs, which are held at chemical potentials of μ_1 and μ_2 by ballistically conducting leads, and b) the corresponding energy level diagram for the setup, showing the energy channels in the object and the energy distributions of electrons in the leads at a finite temperature. After Reference [22].

The dimensions of the object are such that a transverse confining potential exists, resulting in a finite number of well-separated transverse modes; $M(E)$ below an energy E . By contrast, the transverse modes, also known as energy channels, in the reservoirs are assumed to be continuous. Under the assumption of ‘reflectionless’ contacts, reflections for carriers exiting from the narrow conductor to the large reservoirs are neglected. It follows that the Fermi level of a lead will be approximately equal to the electrochemical potential of the adjacent reservoir; μ_1 or μ_2 , and the fractional occupancy of the states will be described by the Fermi-Dirac distribution;

$$f_{1,2}(E) = \frac{1}{1 + \exp [(E - \mu_{1,2})/kT]}, \quad (2.11a)$$

$$\mu_1 - \mu_2 = eV. \quad (2.11b)$$

The density of electrons in the first lead is given by $2g(E)f_1(E)dE$, where

2. THEORETICAL BACKGROUND

$g(E) = \sqrt{m_e}/(h\sqrt{2E})$ is the density of states per unit volume for a one-dimensional system. Multiplying this expression by the carrier velocity, $v(E) = \sqrt{2E/m_e}$, the charge per carrier, e , the average transmission probability per mode, $T(E)$, and the total number of modes $M(E)$, and integrating over all energy, will yield an expression for the total current carried from the first lead to the second;

$$I_1 = \frac{2e}{h} \int_{-\infty}^{\infty} T(E)M(E)f_1(E)dE. \quad (2.12)$$

The expression for the current flowing from the second lead to the first, I_2 , is similar. If it is assumed that $T(E)$ is the same in both directions, which is valid if inelastic scattering is neglected [22], then the net current flowing through the object is given by $I_1 - I_2$;

$$I = \frac{2e}{h} \int_{-\infty}^{\infty} \bar{T}(E)[f_1(E) - f_2(E)]dE, \quad (2.13)$$

$$\bar{T}(E) = T(E)M(E).$$

This is the temperature- and bias-generalised Landauer equation [22–24].

In the low-temperature regime, the Fermi-Dirac distributions (Equation 2.11a) are reduced to step functions, and the integral in Equation 2.13 is evaluated between μ_1 and μ_2 . Also, for low applied biases, the integral is confined to the vicinity of the Fermi level so that $T(E)$ and $M(E)$ may be assumed to take the constant values $T(E_F)$ and $M(E_F)$, respectively. Under these conditions, the current can now be written as;

$$I = \frac{2e}{h}(\mu_1 - \mu_2)\bar{T}(E_F), \quad (2.14)$$

and, using Equation 2.11b, the conductance ($G = I/V$) is expressed by the two-probe Landauer formula;

2. THEORETICAL BACKGROUND

$$G = G_0 \bar{T}(E_F), \quad (2.15a)$$

$$G_0 = \frac{2e^2}{h}. \quad (2.15b)$$

If the mesoscopic object is a ballistic conductor *i.e.* the mean free path of the electrons in the object is much less than the object's length, then the transmission probability for all channels is unity, and it follows from Equations 2.15a and 2.15b that the conductance will be an integer multiple, $M(E_F)$, of G_0 ; the so-called quantum of conductance. This behaviour has been observed in gold break junctions, where the conductance of a gold bridge (between two gold electrodes) decreases by G_0 every time the thickness of the bridge is reduced by one atom [35]. Thus, even a system involving a perfect conductor will exhibit a resistance of approximately $(13/M(E_F))$ k Ω . This is a quantum mechanical resistance that arises from the contacts due the discrepancy between the infinite number of channels in the reservoirs and the finite number in the leads; in going from the former to the latter, the current must be redistributed to the limited number of current carrying channels, causing a bottleneck effect.

Equations 2.13 and 2.15 are useful starting points for modelling the charge transport across mesoscopic bridges. However, the difficulty of defining the transmission function still remains, and approaches for doing this are discussed in the following sections.

2.2.2.1 Quantum Scattering Model in 1D

Consider a beam of particles of mass, m^* , and energy, E , incident upon a rectangular barrier of height, V , with one side at $s = a$ and the other at $s = 2a$. The solutions to the time-independent Schrödinger equation [36] in each of the three regions (in front, inside, and behind the barrier) are;

2. THEORETICAL BACKGROUND

$$\Psi_s = \begin{cases} A_L e^{iks} + B_L e^{-iks}; & s < a, \\ A_1 e^{\eta s} + B_1 e^{-\eta s}; & a < s < 2a, \\ A_R e^{iks} + B_R e^{-iks}; & s > 2a, \end{cases} \quad (2.16)$$

where

$$\eta = \begin{cases} \sqrt{\frac{2m^*(V-E)}{\hbar^2}}; & 0 < E < V, \\ i\sqrt{\frac{2m^*(E-V)}{\hbar^2}} = i\xi; & E > V > 0, \end{cases} \quad (2.17)$$

and

$$k = \sqrt{\frac{2m^*E}{\hbar^2}}. \quad (2.18)$$

The coefficients A_L , B_L , A_1 , B_1 , A_R , and B_R are currently undetermined, but the latter most of which can be set to zero, without loss of generality, if there are no further non-zero potentials to the right hand side of the barrier causing reflections. These coefficients can be related from continuity of the wavefunction and its derivative at the barrier boundaries;

$$\begin{aligned} A_L e^{ika} + B_L e^{-ika} &= A_1 e^{\eta a} + B_1 e^{-\eta a}, \\ ik(A_L e^{ika} - B_L e^{-ika}) &= \eta(A_1 e^{\eta a} - B_1 e^{-\eta a}), \end{aligned} \quad (2.19)$$

$$\begin{aligned} A_1 e^{2\eta a} + B_1 e^{-2\eta a} &= A_R e^{2ika} + B_R e^{-2ika}, \\ \eta(A_1 e^{2\eta a} - B_1 e^{-2\eta a}) &= ik(A_R e^{2ika} - B_R e^{-2ika}). \end{aligned} \quad (2.20)$$

Equations 2.19 and 2.20 can be re-expressed in matrix form [37];

2. THEORETICAL BACKGROUND

$$M[a, ik] \begin{pmatrix} A_L \\ B_L \end{pmatrix} = M[a, \eta] \begin{pmatrix} A_1 \\ B_1 \end{pmatrix}, \quad (2.21)$$

$$M[2a, \eta] \begin{pmatrix} A_1 \\ B_1 \end{pmatrix} = M[2a, ik] \begin{pmatrix} A_R \\ B_R \end{pmatrix}, \quad (2.22)$$

with

$$M[s, \beta] = \begin{pmatrix} e^{\beta s} & e^{-\beta s} \\ \beta e^{\beta s} & -\beta e^{-\beta s} \end{pmatrix}. \quad (2.23)$$

It is now readily apparent that A_L and B_L are related to A_R and B_R as follows;

$$\begin{pmatrix} A_L \\ B_L \end{pmatrix} = M^{-1}[a, ik] \left(M[a, \eta] M^{-1}[2a, \eta] \right) M[2a, ik] \begin{pmatrix} A_R \\ B_R \end{pmatrix}, \quad (2.24)$$

and the transmission, $\bar{T} = (A_R/A_L)^2$, can be calculated, exactly, by considering the (1,1) element of this equation.

Equation 2.24 can be extended to describe coherent tunnelling through sequential rectangular barriers. Thus, it is possible to calculate, numerically, the transmission through an arbitrary potential by approximating it to N rectangular barriers; the m^{th} of which having height V_m (with η_m and ξ_m) and all of which having width a (Figure 2.4). In this case, Equation 2.24 generalises to [37];

$$\begin{pmatrix} A_L \\ B_L \end{pmatrix} = M^{-1}[a, ik] L M[(N+1)a, ik] \begin{pmatrix} A_R \\ B_R \end{pmatrix}, \quad (2.25)$$

where

$$L = \prod_{m=1}^N K[ma, \eta_m] = \begin{pmatrix} P & Q \\ R & S \end{pmatrix}, \quad (2.26)$$

$$K[ma, \eta_m] = M[ma, \eta_m] M^{-1}[(m+1)a, \eta_m]. \quad (2.27)$$

2. THEORETICAL BACKGROUND

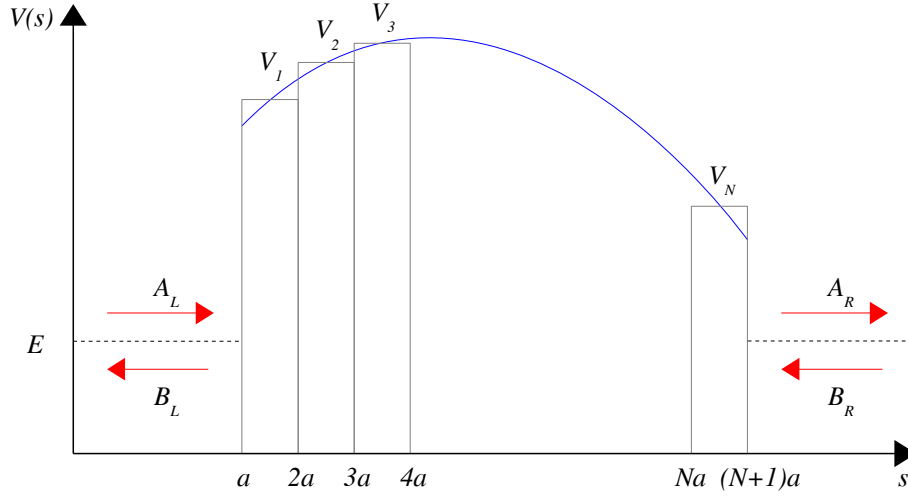


Figure 2.4: An arbitrary potential barrier approximated to a series of rectangular potential barriers. The quantum mechanical transmission through the former can be calculated numerically by considering the successive tunnelling through the latter. After Reference [37].

The K matrices are real for both real and imaginary values of η_m and, from Equations 2.23 and 2.27, can be shown to be;

$$K[ma, \eta_m] = \begin{cases} \begin{pmatrix} \cosh(\eta_m a) & -\frac{1}{\eta_m} \sinh(\eta_m a) \\ -\sinh(\eta_m a) & \cosh(\eta_m a) \end{pmatrix}; & 0 < E < V_m, \\ \begin{pmatrix} \cos(\xi_m a) & -\frac{1}{\xi_m} \sin(\xi_m a) \\ \sin(\xi_m a) & \cos(\xi_m a) \end{pmatrix}; & E > V_m > 0. \end{cases} \quad (2.28)$$

Again, evaluating the (1,1) component of Equation 2.25 and rearranging, the transmission can be expressed as;

$$\bar{T}(E) = \left(\frac{A_R}{A_L} \right)^2 = \frac{4}{(P+S)^2 + (Qk - R/k)^2}. \quad (2.29)$$

The equations outlined in this section were implemented in Python and For-

2. THEORETICAL BACKGROUND

tran, by Dr Martin Elliott, to allow for the calculation of the transmission through an arbitrary-shape scattering potential, for a given energy, applied bias, and effective carrier mass. If the transmission is calculated as a function of energy, $\bar{T}(E)$, then it can be integrated in accordance with the Landauer equation (Equation 2.13) to determine the current-voltage characteristics for the system. The code for this program is listed in Appendix A.

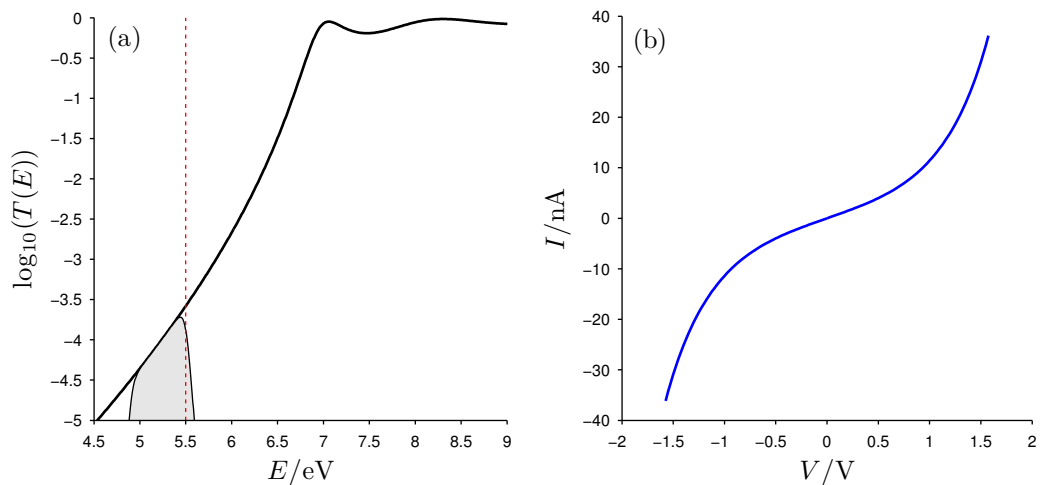


Figure 2.5: a) The computed transmission function for a hyperbolic barrier, described by Equation 2.7, with $\phi_0 = 2.0$ eV, $d_0 = 1$ nm, $\epsilon_r = 2.1$, and $V = +0.6$ V. However, since ϕ_0 should be measured as the barrier height above the Fermi level, the whole barrier has been translated upward in energy by the addition of 5.5 eV, which is the Fermi level of gold measured from the band bottom [38]. Thus, the chemical potential of the first (left) lead, μ_1 , was set to 5.5 eV and that of the second lead, μ_2 , was shifted down to $5.5 - 0.6 = 4.9$ eV under the positive applied bias. The temperature and carrier mass were 300 K and m_e , respectively. The function $T(E)[f_1(E) - f_2(E)]$ was integrated (shaded area), in accordance with the Landauer equation (Equation 2.13), to calculate the current at the given bias; this was repeated for different biases to build up a full $I(V)$ curve; b).

As an example, the program was applied to a hyperbolic barrier, described by Equation 2.7; the results are shown in Figure 2.5. It should be noted that when calculating the transmission, the program has no information about filled or empty states, so will give non-zero transmission values even at energies far

2. THEORETICAL BACKGROUND

below the chemical potentials of the two leads. Information about occupancy is only provided upon integration with the Landauer equation from the Fermi-Dirac functions. Also worth mentioning are the damped, sinusoidal ripples in the transmission for energies greater than the barrier height. The transmission maxima are close to unity (each successive maximum getting closer). Equating Equation 2.29 to unity and making use of Equations 2.28 and 2.17 will show that, for a single rectangular barrier of width a and height V , these peaks occur at $\xi a = n\pi$, where n is an integer *i.e.* the half-wavelength of the particles is an integer multiple of the barrier width [36]. This relationship still holds to a very good approximation if a and V are replaced with the average width and height, respectively, of the hyperbolic barrier discussed in this example (Figure 2.5).

2.2.2.2 Single Molecular Level Model

Consider a system in which a mesoscopic object presents only a single energy level, ϵ , capable of mediating current. This simplistic situation is often justified in the context of molecular systems where the applied bias is low, and transport is therefore dominated by the molecular level closest to the Fermi level.

If the channel is in isolation, then its density of states, $g_\epsilon(E)$, can be described by a delta function at ϵ . However, upon coupling to the reservoirs, having chemical potentials μ_1 and μ_2 , there will be some spatial overlap between the wavefunctions of the continuous reservoir states and the discrete channel state; this results in an energy broadening effect on the latter. The channel is effectively redistributed over the immediate energy-space, experiencing a loss at the fixed energy ϵ , but a gain over a range of energies. The channel becomes an almost continuous density of states, which is often best described by a Lorentz distribution [39];

$$g_\epsilon(E) = \frac{\gamma/2\pi}{(\gamma/2)^2 + (E - \epsilon)^2}. \quad (2.30)$$

The full-width at half-maximum height of the distribution, γ , gives a measure of the total energy broadening, and can be thought of as the sum of the broadening

2. THEORETICAL BACKGROUND

contributions from coupling to each of the reservoirs; $\gamma = \gamma_1 + \gamma_2$. Each broadening contribution is proportional to the strength of the coupling of the bridge to the relevant electrode, which is highly dependent upon the precise details of the junction in question. It is instructive to write an expression defining the asymmetry of the coupling;

$$\kappa = \frac{\gamma_1}{\gamma} = 1 - \frac{\gamma_2}{\gamma}. \quad (2.31)$$

If $\kappa = 1$ or $\kappa = 0$, then the bridge is only coupled to one contact, and the applied voltage is dropped entirely across the other. If $\kappa = 0.5$, the coupling is perfectly symmetrical, and the bias is split evenly across the two contacts.

Each reservoir will attempt to bring the channel states into equilibrium with its own electrochemical potential; the first will try to enforce a population of $f_1(E)$, whereas the second will try to enforce a population of $f_2(E)$ (Equation 2.11a). Thus, this difference of agenda between the two reservoirs results in the flow of current; one reservoir will pump electrons into the channel states whereas the other will drag electrons out of the channel states. If there is no difference between the chemical potentials of the two reservoirs then no current will flow. The terms γ_1/\hbar and γ_2/\hbar may be interpreted as the rates at which an electron placed into the channel will escape into the respective reservoirs. If each term is weighted by the difference between the steady state population of the channel and the population of the respective reservoir, then expressions for the net flux across each contact can be derived. After equating these two net flux terms, and accounting for the broadened density of channel states, the transmission can be shown to be given by [39];

$$\bar{T}(E) = 2\pi g_\epsilon(E) \frac{\gamma_1 \gamma_2}{\gamma_1 + \gamma_2},$$

or, by making use of Equations 2.30 and 2.31;

2. THEORETICAL BACKGROUND

$$\bar{T}(E) = \frac{\kappa(1 - \kappa)\gamma^2}{(\gamma/2)^2 + (E - \epsilon)^2}. \quad (2.32)$$

Equation 2.32 can now be inserted into Equation 2.13, the generalised Landauer equation, to calculate the current-voltage characteristics for a one-level system described by the parameters ϵ , γ , and κ ; a script was written in Python for this purpose. Figure 2.6 illustrates example results of calculations using this model. The transmission tends to unity when the energy of the incident particles is equal to that of the molecular level, and then drops off rapidly or slowly for energies either side of this if the coupling is weak or strong, respectively. The resonant transport is reflected in the $I(V)$ curves with weaker coupling; a rapid increase in current can be observed when the applied bias is such that $T(E)[f_1(E) - f_2(E)]$ begins to encompass the transmission peak.

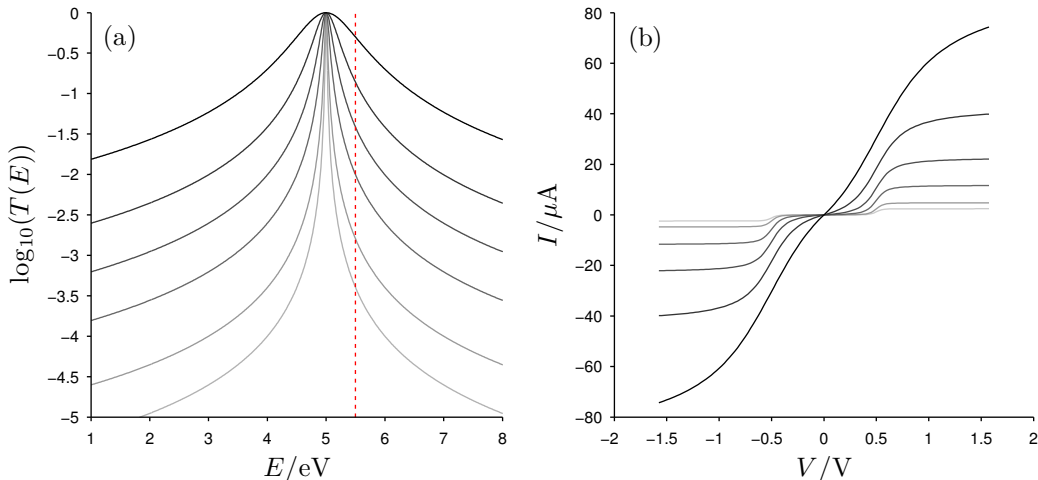


Figure 2.6: Example results of calculations based on the single molecular energy level model (Equation 2.32), with the following fixed parameters; $\mu_1 = 5.5$ eV, $\epsilon = 5.0$ eV, $\kappa = 0.5$, and $T = 300$ K. a) The transmission functions, and b) the corresponding $I(V)$ curves, are shown for varying coupling strengths; $\gamma = 0.02, 0.04, 0.10, 0.20, 0.40, 1.00$ eV, light grey to dark grey (or lowest to highest), respectively.

Clearly, this model will not be accurate for some systems, particularly those

2. THEORETICAL BACKGROUND

with many molecular levels close to the Fermi level that are capable of mediating current. Moreover, it is also likely that the energy broadening of the molecular levels will be dependent upon the applied bias, such that the transmission is actually a function of voltage as well as energy. The potential, and hence, density of states and transmission, of the channel should also be expected to be modified by electrons entering into it, so that a self-consistent solution is required [39]. However, despite its shortcomings, the simple model outlined here is extremely helpful for describing current flow through many molecular systems.

2.2.3 Incoherent Transport Mechanisms

The coherent tunnelling and scattering models, discussed in Sections 2.2.1 and 2.2.2, are appropriate for describing the charge transport through some molecular systems, but do not always describe the full situation. Other charge transport mechanisms need to be considered, and some of these are briefly discussed in this section.

2.2.3.1 Incoherent tunnelling

If the electronic structure of the bridge is such that it can be characterised by a series of potential wells close to the Fermi energy of the electrodes, then charges can tunnel onto the bridge and traverse it by sequential tunnelling steps through successive potential barriers. At each step, the charge is localised on the molecule, residing in a potential well for a finite time (temporarily increasing the charge of the bridge). Depending on phonon scattering rates, this localisation can lead to a disturbance in the phase of the wavefunction of the charge such that it loses coherence with its initial phase; hence, the term incoherent. The process can be modelled by treating the bridge as a series of linked sites, and by considering the rate of tunnelling to and from each site (a tight-binding approach). The transmitted current depends upon the number of links on the chain and, by extension, derives a bridge-length dependence which is usually a very weak exponential decay. This makes the process much more far reaching (tens of nanometres) than coherent tunnelling. To a first approximation, incoherent tunnelling is not temperature dependent and its rate scales linearly with low voltages [33].

2.2.3.2 Thermal Hopping

If the bridge is again characterised by a series of potential wells, it may be possible for electrons to traverse it by thermally hopping over each barrier. The transport rate for such a process will be weighted by a Boltzmann factor, $\exp(-E_B/k_B T)$, where E_B is the activation energy of the barriers and T is the temperature. Unlike the incoherent tunnelling process, thermal hopping will only occur if the thermal motion of nuclei on the bridge results in a favourable molecular geometry *i.e.* one that reduces barrier heights between sites. Therefore, if the molecule is unable to change its configuration because, for example, it is fixed to a rigid substrate, then thermal hopping processes may be nullified. The transmission probability for this mechanism exhibits an inverse relationship with bridge length, meaning it is very long range. The transport scales linearly with low voltages and is heavily dependent upon temperature [33].

2.3 Summary

A short introduction into the electronic properties of organic molecules was given, before transport models for mesoscopic systems were outlined. The Simmons model, based upon the semi-classical WKB approximation of transmission, was described. Three different analytical expressions for three different bias regimes were reached, and then the effect of the image potential was included. The model is very useful in certain circumstances but, ultimately, the coarse approximations employed mean that i) it hides much of the underlying physics, and ii) it will often break down under the extreme conditions involved in molecular bridge systems *e.g.* narrow barriers, high biases, and small areas. The Landauer formalism was then discussed; where current flow in mesoscopic systems is a coherent scattering problem and relies upon the determination of an energy dependent transmission function. Two different models for calculating this transmission function were discussed. The first approach treats the molecule as an arbitrary one-dimensional quantum mechanical tunnelling barrier and calculates the transmission through it, numerically, by approximating it to a series of rectangular barriers and by employing a transfer matrix approach. This approach is appropriate for insulating

2. THEORETICAL BACKGROUND

molecules, in which the molecular energy levels are out of reach of the chemical potentials of the electrodes. The second approach considers the transmission for a system in which there is a single molecular energy level capable of carrying current in the vicinity of the chemical potentials of the electrodes. Python scripts have been written for both models. Finally, discussion was leant to incoherent transport mechanisms, such as thermal hopping.

Chapter 3

Experimental Background

In Chapter 2, the background theory necessary for understanding the electronic structure of organic molecules and the charge transport through such nanoscale objects was discussed. In this chapter, the experimental techniques used to obtain the results of this thesis are provided. There is a brief description of the ultra high vacuum (UHV) apparatus and sample preparation procedures, followed by a discussion of the principles of scanning tunnelling microscopy (STM) and scanning tunnelling spectroscopy (STS), with focus on single molecule conductance measurement techniques and the subsequent data analysis.

3.1 Ultra High Vacuum System

The experiments reported in this thesis were conducted using the Omicron UHV [40] system at Cardiff University [41] (Figure 3.1). The system contains a variable temperature scanning probe microscope (Omicron VT SPM); X-ray and ultraviolet sources, as well as an electron detector for photoelectron spectroscopy; a low energy electron diffraction (LEED) optic [42]; an argon ion gun (ISE 10) for sample sputtering; and a heater, capable of direct current heating or radiative heating using a pyrolytic boron nitride (PBN) ceramic element, for sample annealing. After baking the chamber, a base pressure between 10^{-9} and 10^{-10} mbar can be achieved using a turbomolecular pump and a titanium sublimation pump and, subsequently, can be maintained by an ion getter pump [16].

3. EXPERIMENTAL BACKGROUND



Figure 3.1: The Omicron ultra high vacuum system at Cardiff University, nanophysics laboratory, 2013.

Samples can be loaded into the main analysis chamber via a small fast-entry lock chamber; this must be pumped for several hours (by a turbomolecular pump) to reach UHV pressures after having been vented to atmosphere. When inside the analysis chamber, the samples can be moved to the various instruments using the manipulator arms, or placed on the sample carousel for long term storage. Under UHV, atmospheric contaminants such as oxygen, water vapour, and organic compounds are minimised, making conditions ideal for sample storage and study. By comparison to experiments performed in ambient conditions, UHV experiments can help to distinguish the intrinsic properties of a system from those arising from environmental factors.

3.2 Experimental Preparation

In this section, the typical process of readying a sample for UHV STM-based single molecule conductance (SMC) measurements are outlined. Details and parameters may vary slightly between different individual experiments, but the preparation procedure is largely the same in each case.

3.2.1 Substrate Cleaning

All of the experiments were conducted using either Au(111) single crystals, or Au(111)/mica substrates. The majority of experiments were performed using the latter, and these were purchased from PHASIS [43]. The epitaxially-grown gold layers had a quoted purity of 99.99% and a thickness of 200 nm. The primary advantage to using gold as a substrate is that it is largely inert and so will not readily oxidise under ambient conditions. For a similar reason, but also to achieve bridge systems with symmetric electrodes (to eliminate the effects of chemical asymmetry), gold STM tips were employed for the molecular conductance measurements; the tip preparation procedure is outlined in Section 3.2.2.

The substrates were subjected to a standard acetone and isopropanol rinsing procedure to remove organic contaminants before being blown dry with nitrogen gas to avoid surface tide marks. The samples were then inserted into the UHV chamber to undergo a process of argon ion sputtering and annealing. Firstly, they were annealed for approximately 1 hour at temperatures of 650 °C or 350 °C for single crystal and mica substrates respectively; this was to help remove physisorbed [42] atmospheric contaminants. After being allowed to cool, the substrates were ion sputtered for around 15 minutes to remove chemisorbed contaminants. The ion gun filament emission current was 10 mA and the beam energy was 1 keV; under these settings, the absolute beam current striking the sample manipulator was usually measured to be around 2.0 μA . Under the cavalier assumption of a uniform, circular beam of diameter 10 mm [44], the current density striking the sample surfaces can be calculated to be of the order of 0.025 μAmm^{-2} . After sputtering, the samples were then annealed again to encourage surface ordering. Since annealing encourages impurities from the bulk to diffuse

3. EXPERIMENTAL BACKGROUND

to the surface, several more sputter-anneal cycles are required to obtain clean, atomically flat surfaces, particularly for single crystals.

3.2.2 Tip Fabrication

Gold STM tips for conductance measurements were prepared by electrochemically etching 0.5 mm gold wire (99.99%) in an equivolumar mixture of HCl and ethanol, at 2.4 V [45]. Molecular resolution imaging could not be achieved using these tips, likely because gold is soft and the atoms are very mobile. Instead, tungsten tips were used for the purposes of imaging, and these were prepared by electrochemically etching 0.5 mm tungsten wires in 2 M aqueous solutions of NaOH, at 10 V [46]. After the etching was complete the tips were usually coated with a white residue, presumably tungsten oxide, which was removed by a thorough rinsing with deionised water (18 M Ω cm).

3.2.3 Molecular Deposition

As mentioned in Chapter 2, the manner in which the molecule makes contact with the electrodes plays a vital role in determining the electronic transport properties of the bridge system. In the presence of gold, thiol (-S-H) and thioester (-S-COCH₃) groups on organic molecules have been shown to undergo a bond cleavage process, resulting in the formation of thiolate (-S-) groups and subsequently strong S-Au covalent bonds (leading to self-assembled molecular monolayers [47]). These bonds are expected to provide an efficient electronic coupling to the gold (and other metallic) electrodes, and thus have been widely employed as molecular crocodile clips at the ends of molecules during molecular conductance investigations [35, 48–50]. However, other anchoring groups such as carboxylic acids, pyridines, and amines have also been used for this purpose and have been found to be effective [51].

The two molecular species studied in this investigation were α,ω -alkanedithiols, purchased from Aldrich, and thioester-terminated oligothiophenes (Figure 5.1), synthesised by the research group of Richard Nichols and Simon Higgins at the University of Liverpool [52]. Clean substrates (Section 3.2.1) were removed

3. EXPERIMENTAL BACKGROUND

from the UHV chamber, transported through air, and then submerged in low concentration molecular solutions; 5×10^{-5} M with respect to a toluene or dichloromethane solvent, for 20 minutes. The low concentrations and short submersion times were chosen in order to achieve low surface coverages so that the conductance measurements would reside in the single molecule regime [47]. After rinsing in pure solvent for 60 seconds (to remove excess, weakly bound molecules) and blowing dry with dry nitrogen, the readied samples were transported, again through air, and loaded back into the UHV chamber. Experiments could be performed on the samples over periods of several days as it was established that single molecule conductance measurements did not change over this time.

3.3 Scanning Tunnelling Microscopy

In STM, an atomically sharp, conducting tip (Section 3.2.2) is brought very close (< 50 Å) to a conducting or semiconducting surface (such that the electron wavefunctions in the two experience significant overlap). After applying a potential difference across the junction, the quantum mechanical tunnelling current flowing across the junction is monitored. Piezo-electric elements are used to adjust the position of the tip, both laterally ($x - y$) and vertically (s), with subatomic precision [42]. Images can be constructed by raster scanning the tip over the surface and recording the s -position (height) required to maintain a constant tunnelling current, which is regulated by a feedback loop. Alternatively, the height can be kept constant and modulations in the tunnelling current can be mapped in a similar way.

If the gap between the tip and the sample is treated as a simple potential barrier to charge flow, then the current can be described using the Simmons model (Section 2.2.1). Equation 2.4 suggests that the current decays exponentially with barrier width *i.e.* tip-sample separation (and that it decays exponentially with the square root of the barrier height). This relationship means that STM is extremely surface sensitive, probing only the top one or two sample surface layers. Furthermore, the vertical resolution is incredibly high (~ 0.01 Å); a change in tip-sample separation of 1 Å will typically change the tunnelling current by an

3. EXPERIMENTAL BACKGROUND

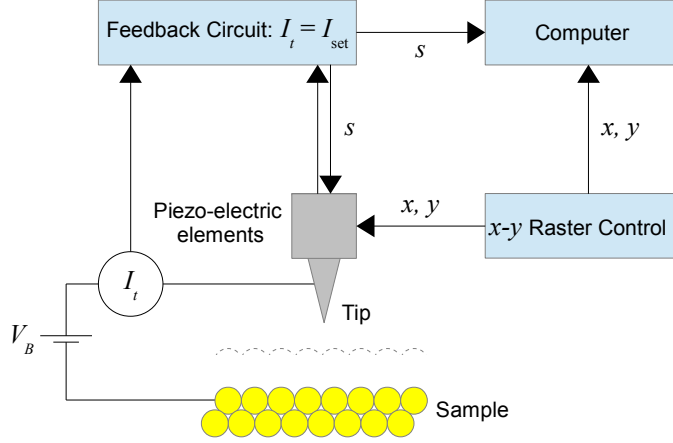


Figure 3.2: Schematic diagram of an STM in constant-current imaging mode. A quantum mechanical tunnelling current, I_t , flows between the biased (V_B) conducting tip and sample. A feedback loop seeks to ensure that the measured tunnelling current is equal to the predefined setpoint current, I_{set} , by applying a voltage to a piezo-electric element to adjust the height, s , of the tip. The tip is raster scanned in the plane of the sample surface (x - y) and an image is built up using the values of s required to maintain the current setpoint at each location.

order of magnitude. The lateral resolution of STM is determined by the geometry of the tip; in the ideal situation where the tip is terminated by a single atom, this will be approximately 1 \AA .

By employing Bardeen's tunnelling theory [53, 54], Tersoff and Hamann showed that the tunnelling current is proportional to the local density of states (LDOS) of the sample at the Fermi level at the position of the tip [55]. To reach this conclusion, the following assumptions were applied: i) tunnelling is weak enough so that first-order perturbation theory [56] can be used and electron-electron interactions can be neglected; ii) states in the sample and states in the tip are nearly orthogonal and their occupation probabilities are independent of each other and do not change over time, regardless of tunnelling; iii) the density of states in the metallic tip is constant; and iv) temperatures and applied biases are low. (The

3. EXPERIMENTAL BACKGROUND

latter is required in order to retain the validity of the WKB approximation). Hence, it is important to remember that the observed image corrugation in STM is often not simply related to topographic surface variations, especially in the case of semiconductors where charges are highly localised. Features that are invariant between positive and negative applied biases of equivalent magnitude are likely to be purely topographic in nature.

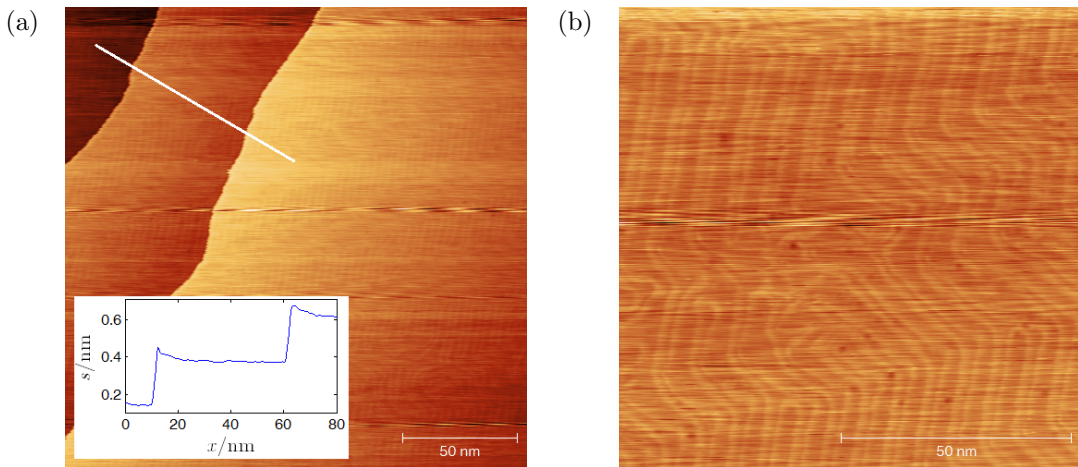


Figure 3.3: a) Large area and b) small area scanning tunnelling microscope images of an annealed Au(111)/mica surface taken using a tungsten tip, with the Omicron VT SPM system at Cardiff University. In both images, the well-known herringbone surface reconstruction can be observed [57]. Inset in Figure a) is a line profile that traverses the three observable terraces. The average step height, 0.237 nm, is in good agreement with the theoretical monatomic step height for Au(111); 0.236 nm [58].

Experiments were performed using an Omicron VT SPM in STM mode, in the UHV system discussed in Section 3.1. Shielding from vibrational and electromagnetic noise was provided via a spring isolation system and by the walls of the chamber, respectively. The system was equipped with two current amplifiers; 0.0015 to 3.3 nA (low current) and 0.18 to 333 nA (high current). The lower limits here are imposed by background current noise and were determined experimentally. The tip-sample bias is variable in the range ± 10 V. The temperature of the samples on the STM stage could be raised to a theoretical maximum of 1500 K by direct current heating or 750 K by a PBN resistive heater element,

3. EXPERIMENTAL BACKGROUND

and lowered to 120 K or 40 K using liquid nitrogen or helium, respectively. The device was controlled by MATRIX v3.0 software, again developed by Omicron Nanotechnology [40]. Both $I(V = \text{voltage})$ and $I(s = \text{distance})$ spectroscopic modes (discussed in Section 3.3.1) were available as standard, along with the option for custom scripts.

3.3.1 Scanning Tunnelling Spectroscopy

The scanning tunnelling microscope (Section 3.3) is extremely versatile and its applications extend far beyond imaging. The fact that the microscope probes the LDOS of a sample can be harnessed to investigate the surface electronic structure. By measuring the tunnelling current (or differential of the current with respect to bias) as a function of a certain parameter *e.g.* applied bias or tip sample separation, much information about the electronic properties of a system can be extracted. Moreover, the high precision of the STM, allowing for such subtle endeavours as atomic and molecular manipulation, means that such spectroscopic modes can be readily applied to investigate the electronic properties of individual molecules. In this section, STS techniques and their application to single molecule samples are outlined. All of the techniques discussed share the common principle of wiring up molecules between STM tip and substrate and then using the two as electrodes.

3.3.1.1 Current *versus* Voltage, $I(V)$

In $I(V)$ spectroscopy, the feedback loop is switched off and the tunnelling current is measured as a function of applied bias at a constant piezo height. The resulting $I(V)$ curves can be modelled using the theory outlined in Chapter 2 and reveal information about the electronic structure of whatever lies between tip and substrate. A statistical analysis is usually necessary, requiring the procurement of many curves. If consecutive traces are being taken, it is appropriate to ramp the voltage in a triangular wave between the positive and negative limits to avoid abrupt changes in the electric field, but also to detect any asymmetries that may exist between the two ramp directions.

3. EXPERIMENTAL BACKGROUND

3.3.1.2 Current *versus* Distance, $I(s)$

The majority of work in this thesis is based around experiments using the $I(s)$ technique [48]. In this method, the tip is taken out of feedback and the tunnelling current is monitored as a function of tip-sample separation, at a fixed bias. Typically, a current setpoint of 300 – 500 pA was acquired before the feedback loop was disengaged and the tip was driven down toward the substrate (by 0 – 1 nm) until the high current amplifier (> 333 nA) was saturated. It was then retracted by a distance slightly greater than the length of the molecular species in question, at speeds between 0.1 to 15.0 nms⁻¹, and the tunnelling current was measured as a function of this distance.

If this measurement is performed over a bare surface then an $I(s)$ curve of the form of an exponential decay should be expected, according to Equation 2.4. However, in the presence of molecules on the surface, plateaus in the current may be observed in the $I(s)$ traces and, in the literature [50], these are attributed to the formation and subsequent destruction of molecular bridges between tip and sample. Figure 3.4 shows an example curve that exhibits such a current plateau and a toy model has been applied to help illustrate how it arises. In this model, the total current flowing between tip and sample is treated as the sum of the contribution from direct tunnelling between tip and sample and from that flowing along the molecule. The direct tunnelling contribution decays exponentially with distance, whereas the molecular contribution remains constant (assuming the molecule is rigid). Eventually, with distance, the decaying exponential becomes washed out and the total current tends toward the constant contribution from the molecule, before the junction is broken and the current abruptly drops. The noise on the plateau is assumed to arise from variations in the atomic arrangement of the molecular contacts.

This model should not be taken too seriously, but clearly it manages to produce the qualitative appearance of current plateaus and goes some way toward helping explain how they arise. Essentially, it involves describing the total transmission as an average between the direct tunnelling contribution and the molec-

3. EXPERIMENTAL BACKGROUND

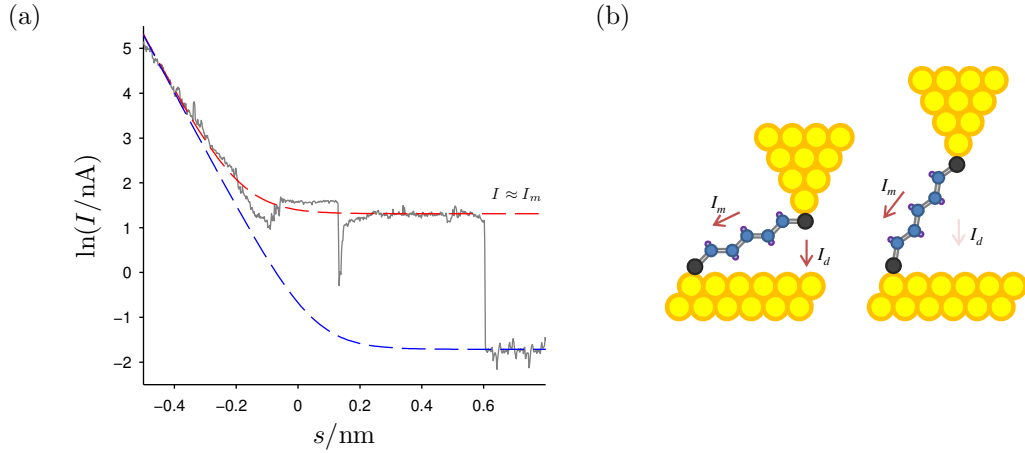


Figure 3.4: a) An example $I(s)$ curve above a 1,6-hexanedithiol sample (with a tip bias of +0.1 V) that demonstrates a current plateau, thought to be indicative of molecular bridge formation and b) a cartoon representation of the situation. A simple model has been applied to the curve to help conceptualise how the plateau arises; the total current flowing is considered to comprise the sum of a molecular contribution, I_m , and a contribution from direct tunnelling between tip and substrate, I_d . The former remains constant with retraction distance, whereas the latter decays exponentially. The red dashed line is of the form $A \exp(-\beta s) + I_m$ and the blue dashed line, representing the case where no bridge is formed, is of the form $A \exp(-\beta s) + c$, where $c = 0.18 \text{ nA}$ is the amplifier noise level. After a short distance, I_d becomes greatly diminished and the total current converges toward I_m . The molecule eventually breaks off resulting in an abrupt drop in the total current.

ular contribution. The tunnelling contribution can be described by the Simmons model (Section 2.2.1) or by any other appropriate model that involves tunnelling through a barrier (Section 2.2.2.1) and diminishes with retraction distance (barrier width). The transmission curve for the molecular contribution can take many forms *e.g.* Equation 2.32; as long as it remains constant with retraction distance the model will produce current plateaus. Often there are reports of current plateaus at integer multiples of a fundamental value [35, 48, 50, 59]. These are attributed to molecular bridges consisting of many molecules in a parallel arrangement. The model can be readily adapted to account for this by weighting the transmission from the molecular contribution accordingly.

Bridge formation is a stochastic event, subject to fluctuations, meaning that

3. EXPERIMENTAL BACKGROUND

statistical analysis is required to obtain true molecular conductance values for the arrangement. Therefore, at different regions above the sample surfaces, several thousand consecutive curves were usually recorded. Typically, about 1 – 3% of the curves demonstrated evidence of molecular bridge formation and these were selected, by a lenient automated gradient analysis program and subsequently by eye, and binned into logarithmic histograms. If the histograms are constructed by dividing the current scale of $I(s)$ curves into intervals, then plateaus in statistically significant numbers will produce current peaks that allude to the molecular conductance values of the system. For each molecular system, this process was repeated for different biases and temperatures; spanning ranges of ± 1.6 V and 180 – 390 K, respectively. The gradients of the linear regions of the $I(s)$ -constructed $I(V)$ curves (Section 3.3.1.1) were measured to obtain single molecule conductance (SMC) estimates. Two-dimensional histograms, either current *versus* distance (Figure 3.5a), or conductance *versus* absolute tip-sample separation distance, are also often useful for interpreting data sets and are employed in this thesis.

In some cases, curve selection was not necessary and peaks could be observed even after binning an entire data set into a single histogram (an all-data histogram). However, this was not the case in general and heavy selection was usually required. An alternative method for the construction of histograms is to only bin the current value measured at the end of a plateau (such that there is only one current value per curve), instead of binning the entirety of the curve. This method can be useful for reducing histogram background noise in the cases where the “plateaus” are sloped, short, or noisy, but it can sometimes reduce the peak signal and increase uncertainty margins if the selection rate is very low. However, it has been shown elsewhere that the two analysis methods can produce equivalent SMC estimates [60–62]. Logarithmic histogram bins allow features to be observed over the full current range simultaneously. Moreover, having narrower bins at lower currents prevents peaks at these values from being lost amidst the amplifier noise peak. There is no definitive method for determining the optimum number of bins to use in a histogram and experimentation is always necessary; however, a good starting number is the square root of the total number of counts.

3. EXPERIMENTAL BACKGROUND

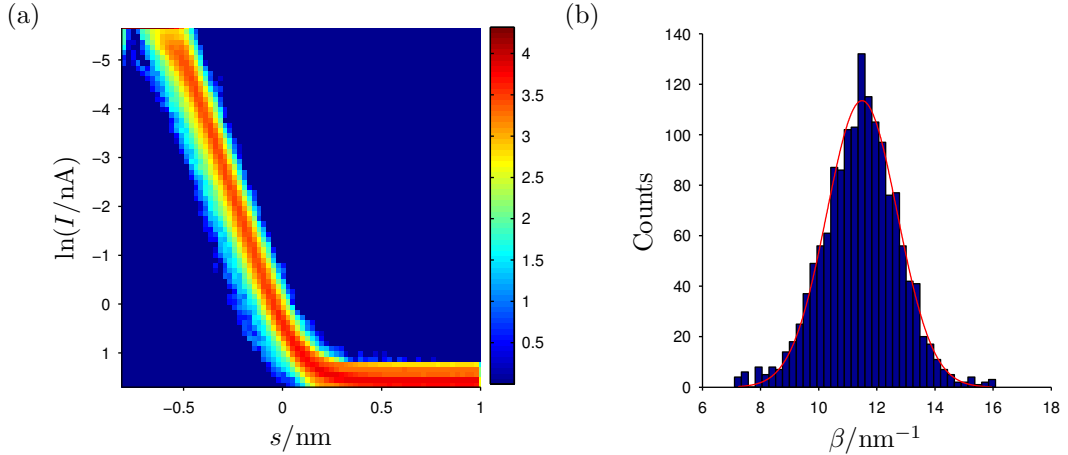


Figure 3.5: a) An area density plot (the colour scale is the common logarithm of the counts in each two-dimensional bin) for an $I(s)$ curve set (1500) taken above clean Au(111)/mica, using the high current adapter. The applied bias, current setpoint, and approach distance from the current setpoint were 0.1 V, 500 pA, and 0.8 nm, respectively. Aside from noise, the curves are largely featureless and show no signs of current plateaus, fitting closely to exponential decays. b) Histogram of the gradients of the linear fits to the linear portions of the curves, fitted with a Gaussian distribution; the best estimate of the peak position suggests $\beta = (11.5 \pm 0.1) \text{ nm}^{-1}$ (Equation 2.4).

In order to fully interpret $I(s)$ spectra, the tip-sample separation must be determined in absolute terms. This can be achieved by assuming that the measured conductance corresponds to G_0 (Equation 2.15b) at the point of mechanical contact between tip and sample ($s_0 = 0$), and then decays away from this exponentially with distance; $G = G_0 \exp(-\beta s)$ (Equation 2.4). The absolute distance above the surface, s_0 , for a bias, V , and current setpoint, I , is expressed as

$$s_0 = -\frac{1}{\beta} \ln \left(\frac{I/V}{G_0} \right). \quad (3.1)$$

Thus, it is necessary to obtain an estimate of β for each system in question (and repeatedly check it throughout an experiment). This can be done by selecting $I(s)$ traces that show no evidence of molecular bridge formation, taking their natural logarithms, and then measuring the gradients of the linear regions. If

3. EXPERIMENTAL BACKGROUND

this is done for many such curves, a statistical approach can be adopted. As an example, Figure 3.5 shows the featureless $I(s)$ curve set obtained over a bare gold sample, along with the histogram of the gradients used to obtain the best estimate of β for the system.

Given the experimental conditions, the average value of $\beta = (11.5 \pm 0.1) \text{ nm}^{-1}$ suggests an initial tip-sample separation of $(0.84 \pm 0.01) \text{ nm}$ before the approach; this implies that even after the 0.8 nm approach the two are still slightly short of mechanical contact. For all of the experiments in this thesis, a careful calibration process was performed to ensure that the tip was as close as possible to the surface without crashing into it. Before each experiment, a preliminary set of $I(s)$ traces was measured, during which the approach distance from the initial setpoint was altered, slowly and incrementally, until the curves saturated the high current amplifier yet still overlapped with one another other *i.e.* they all had similar current values at given values of s (apart from the few that exhibited plateaus). The point of significant mechanical contact could be observed when, past a certain approach distance, the traces abruptly ceased to overlap with each other and began to shift back and forth along the s -axis by large amounts. This occurs because the tip and surface are altered upon impact and retraction – changing the separation distance between the two during successive measurements. Thus, care was taken to avoid this regime. In cases, the initial tip-sample separation may seem very small; however, since the calibration was always performed, it is believed that significant mechanical contact (enough to distort the tip) was usually avoided. It is this point that distinguishes the $I(s)$ method from the STM break junction technique (STM BJ) [59]. In the latter case, the tip is deliberately crashed into the surface by a substantial amount, forming a gold-gold junction. Upon retraction the junction is cleaved and molecular bridges can form in the gap. Even though the difference between the STM BJ and $I(s)$ methods is subtle, the conductance values measured by the two techniques can be profoundly different for the same molecular system [48, 59]; values measured by the STM BJ technique are often larger. This difference is elaborated upon in Chapter 4 when discussing the alkanedithiol species, but it is thought to be attributed to different levels of electrode roughness induced by the two different techniques, leading to

3. EXPERIMENTAL BACKGROUND

different observation probabilities of certain molecular binding group-substrate coordination geometries [50, 60, 61, 63].

A comparison needs to be made between the experimentally determined value of β and the expected value for clean Au(111). The bulk work function of clean Au(111) ranges between 5.1 and 5.5 eV [64, 65], yielding an expected value of $\beta = (23.5 \pm 0.5) \text{ nm}^{-1}$ from Equation 2.4 with $\alpha = 1.0$. Using the same equation, the experimental value of $\beta = (11.5 \pm 0.1) \text{ nm}^{-1}$ implies an effective average barrier height of $(1.26 \pm 0.2) \text{ eV}$, or $(2.45 \pm 0.2) \text{ eV}$ after the effects of the image potential have been removed using Equation 2.8 with an estimated average value of $d_0 = 0.65 \text{ nm}$ (mean absolute tip-sample separation measured from linear regions of the curves). Clearly, even after accounting for the image potential, the barrier is still far lower than the expected value for a clean surface. In fact, again assuming that the measured barrier was distorted by the image potential, the measured value of β would require a value of $\alpha = (0.725 \pm 0.015)$ *i.e.* a carrier mass of $(0.525 \pm 0.025) m_e$. Mangin *et al.* observed similar behaviour for gold nanogaps produced by electromigration of nanowires under low vacuum (10^{-5} mbar); average barrier heights of $< 2 \text{ eV}$ are reported and the effects of the image potential are again insufficient to account for such low values [66]. Other groups have also reported similar reductions in work function in air [67], water [68], and electrolyte solutions [69]. The proposed explanations for the reductions include surface contamination by water, oxygen, and organic molecules, as well as surface defects. With regard to the latter, local barrier heights as low as 0.1 eV have been measured in the surface locations where there are missing rows of gold atoms, even under very clean conditions [70]. Thus, it is possible that in this experiment the surface was rough *i.e.* had many defects, or was contaminated despite being under UHV and having undergone cleaning (Section 3.2.1). Some contamination from exposure to atmosphere could have remained after cleaning or accumulated in the short time between cleaning and measurement; monolayers can accumulate quickly even at UHV pressures [42]. Since the molecular samples were prepared outside of the vacuum chamber (Section 3.2.3), effects of atmospheric contamination should be considered during analysis of the experimental data.

3. EXPERIMENTAL BACKGROUND

3.3.1.3 Current *versus* Voltage and Distance, $I(V, s)$

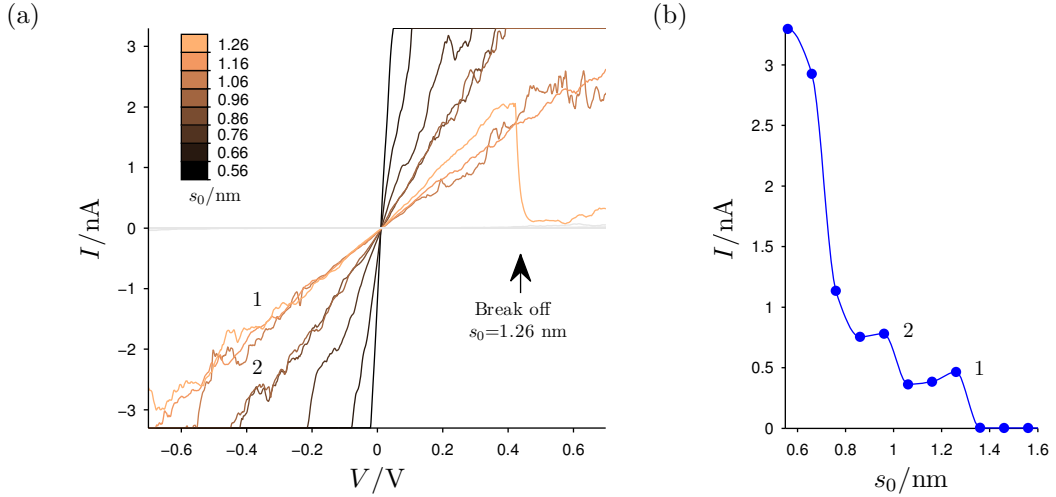


Figure 3.6: a) An example of a positive result obtained from the $I(V, s)$ technique on a 1,8-octanedithiol sample. The tip approached the surface by 0.6 nm, from an initial setpoint of 500 pA and -0.7 V, before being retracted in 0.1 nm steps, with $I(V)$ sweeps from -0.7 V to 0.7 V and back again (not shown for clarity) being performed at each step. The curves first converge to gradients of roughly $\sigma = (8.09 \pm 0.03)$ nS (2) and subsequently $\sigma = (4.39 \pm 0.02)$ nS (1); implying the existence of a two-molecule, followed by a one-molecule bridge. An abrupt drop in current (“break off”) can then be observed during the curve taken at $s_0 = 1.26$ nm, indicating the spontaneous destruction of the existing single molecule bridge. The remainder of the curve set resides close to zero current (grey). Figure b) is an $I(s)$ curve, fitted with a smoothing spline, obtained by sampling each $I(V)$ curve in a) at a bias of 0.1 V. The distance axis was calibrated using Equation 3.1 with $\beta = (10.0 \pm 0.3)$ nm $^{-1}$, determined from a statistical slope analysis of prior $I(s)$ curves over the same sample.

SMC measurements were also obtained using a novel $I(V, s)$ method, developed using a custom script. The tip was made to approach the surface in a similar manner to the $I(s)$ method, detailed in Section 3.3.1.2, but with a high negative applied bias (typically -0.7 to -1.5 V). It was then retracted in small increments (0.05 to 0.1 nm) and $I(V)$ curves were taken at each step; sweeping from the negative setpoint bias to the equivalent positive bias and then back again. Including time taken for voltage sweeps, the average retraction speed was roughly 0.1 nms $^{-1}$ or lower. This produced a series of $I(V)$ curves as a function of distance above the surface. In some cases, the curve set can be seen to converge

3. EXPERIMENTAL BACKGROUND

toward a non-zero gradient as the tip is retracted, before exhibiting an abrupt drop either between consecutive curves or during a single curve; these effects were attributed to the presence and subsequent destruction of molecular bridges and can be explained with the same model used to explain the current plateaus observed with the $I(s)$ method. Figure 3.6 shows an example of a positive result obtained for 1,8-octanedithiol. If the molecules are being fully stretched, then the last $I(V)$ curve(s) before bridge destruction should, nominally, be similar to those constructed by the $I(s)$ method. Equation 3.1 can again be used to calibrate absolute distances. The advantage to this method over the $I(s)$ or $I(t)$ (Section 3.3.1.4) methods is that the full $I(V)$ characteristics of a molecule can potentially be obtained in a very short time scale; however, the data can often be a lot more difficult to interpret correctly.

3.3.1.4 Current *versus* Time, $I(t)$

With the $I(t)$ method [71], a current setpoint, I_1 , is acquired such that the tip-substrate separation is smaller than the molecular species being studied. At a fixed position and bias, V , the feedback loop is turned off and the tip is allowed to drift for a short time whilst the tunnelling current is monitored. Given appropriate anchoring groups, molecular junctions can form spontaneously between tip and substrate if the tip drifts near a molecule with a favourable orientation. At this point, the current will abruptly jump from the initial setpoint to a new constant value, I_2 , and remain so for a short time, before dropping back down after the junction is broken. Hence, the molecular conductance can be deduced by $(I_2 - I_1)/V$. These measurements should, in theory, give a better estimate of molecular conductance than the $I(s)$ method since a direct difference between on and off states is being measured. However, the method is fraught with difficulties, such as variation in the measured conductance with setpoint due to different molecular conformers [34]. Haiss *et al.* conducted calibration experiments on bare gold and on samples with alkanethiols to address the question of whether such current jumps originated from random noise or from spontaneous molecular bridge formation; in both cases no positive results (current jumps) were obtained, suggesting that the jumps over alkanedithiol samples were indeed caused by the

latter [71].

Fixed-voltage single-point $I(t)$ measurements can also be useful for assessing the stability of a tunnel junction before imaging or other spectroscopic measurements are performed; the variation in the current under these conditions provides an indication of the variability of the tunnel barrier height, due to influences such as thermal noise, and so can be used to estimate the uncertainty in subsequent experiments.

3.4 Summary

After a discussion of the UHV system used for the experiments in this thesis, template procedures for preparing the alkanedithiol and oligothiophene samples for SMC measurements by STM were given. The operational principles of the STM were described and related back to the theory of tunnelling in Chapter 2, before the main SMC measurement techniques were expounded; these included the $I(V)$, $I(s)$, $I(V, s)$, and $I(t)$ methods. Particular focus was given to the $I(s)$ method (and its calibration), in which the tunnelling current is monitored as a function of tip retraction distance at a fixed bias. Using a simple model, current plateaus in the resulting $I(s)$ curves were shown to be indicative of molecular bridge formation between tip and substrate, with the values of the plateaus giving estimates of their conductance. The unwieldy nature of all the SMC methods means that large data sets need to be obtained and analysed in a statistical manner, which often entails the use of histograms.

Chapter 4

Alkanedithiols

Chapters 2 and 3 established the background theory and experimental details, respectively, necessary for understanding the single molecule conductance measurements reported in this thesis. This chapter focusses on presenting, explaining, and discussing the $I(s)$ and $I(V, s)$ results obtained from the Au-alkanedithiol-Au system. However, beforehand, an introduction into the nature of the system and a discussion of the important related works reported in the literature is given.

4.1 Introduction

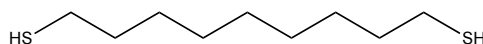


Figure 4.1: Structural diagram of 1,9-nonanedithiol ($N = 9$ methylene units), which is one of the α, ω -alkanedithiols studied in this thesis.

The α, ω -alkanedithiol (ADT) species, $\text{HS}-(\text{CH}_2)_N-\text{SH}$, consists of thiol-terminated methylene chains; the fully extended length (all-trans conformers) of which, $L(N)$, can be evaluated, in nanometres, by the empirical formula [72, 73];

$$L(N) = 0.127N + 2(0.25). \quad (4.1)$$

ADTs are the simplest molecules that can be reliably coupled between metallic electrodes and have therefore played a prominent role in the development of single molecule conductance (SMC) measurement techniques; acting, somewhat, as a calibration molecule. As such, there exists a wide range of theoretical reports on the Au-ADT-Au system [74–80], as well as reports of experimental investigations conducted under various different environmental conditions (and with a variety of techniques), including; air [25, 29, 34, 48, 60, 71, 81–84], organic solvents [51, 59, 61–63, 71, 81, 85–87], dry gases [25, 49], ionic liquids and solutions [62, 88, 89], and UHV [27, 90–92]. However, with regards to the latter, there are very few reports and no systematic studies over a large range of molecular chain lengths.

These molecules should be expected to behave as electrical insulators since the HOMO-LUMO gap is large ($\sim 8 - 10$ eV for the full chain length range) and the frontier orbitals are far removed from the Fermi energy of gold electrodes ($\sim 5.1 - 5.5$ eV) [25, 27, 38, 77, 79, 93]. Density functional theory (DFT) calculations place the LUMOs and HOMOs at over 5 eV above, and less than 3 eV below, the gold Fermi level, respectively, and complex band structure calculations yield effective carrier masses of about $3.0 m_e$ and $0.3 m_e$ for electron and hole tunnelling, respectively [25, 77, 79]. These considerations point to non-resonant coherent hole tunnelling as the dominant transport mechanism for the species, which may be expected to result in conductance values that are largely independent of temperature and environmental conditions, and which demonstrate a simple exponential decay relationship with chain length (barrier width). However, despite the superficial simplicity of the system, numerous problems and sources of confusion have arisen in the literature and some of these issues are currently unresolved.

4.1.1 Temperature Dependence

From the tunnelling theory outlined in Chapter 2, temperature-dependent conductance values should not be anticipated for ADTs. Interestingly, Haiss *et al.* studied chain lengths of $N = 5 - 9$, employing the $I(t)$ method under air, and

observed an exponential increase in conductance with temperature over a range of 300 to 353 K. However, this trend was attributed to an increase with temperature in the population of highly-folded molecular (gauche) conformers, which offer more negotiable tunnelling barriers. This effect is apparently nullified if the technique entails fully stretching the molecules *e.g.* the $I(s)$ method [94], or if the molecular species is rigid and unable to access gauche conformations [34].

Wang *et al.* performed measurements on self assembled monolayers (SAM) under nitrogen, investigating chain lengths of $N = 8 - 16$, and observed no dependence over a temperature range of 90 – 300 K [93]. More recently, Song *et al.* investigated the same chain length range over a complementary temperature range of 4.2–90 K, using an electromigrated nanogap approach under helium gas, and again observed no dependence [49]. Akkerman *et al.* performed large area (SAM) measurements on Au-PEDOT:PSS-ADT-Au structures under UHV and found the conductance for chain lengths of $N = 8 - 14$ to be invariant over a temperature range of 199 – 300 K [92]. These reports strongly point to off-resonant tunnelling for the transport mechanism. In this chapter, the temperature dependence of ADT SMC is explored under UHV over chain length and temperature ranges of $N = 3 - 10$ and 180 – 390 K, respectively; both of these ranges overlap with and extend those investigated in UHV and other environmental conditions elsewhere [49, 92, 93].

4.1.2 Chain Length Dependence

The SMC for ADTs should be expected to decay exponentially with increasing molecular chain length, in accordance with tunnelling through a simple barrier. This trend has been observed during experimental studies on long molecules ($N > 5$) [25, 49, 51, 59, 61–63, 81, 83, 84, 88, 93, 95, 96] and theoretical investigations [74–80], with reported decay constants per methylene unit spread around $\beta_N = (1.0 \pm 0.2)$. Using β_N , extrapolation of the conductance back to $N = 0$ should result in a value of $G_0 \approx 77 \mu\text{S}$, and this is indeed observed in many of the cited experimental studies. However, investigations measuring both short and long chain lengths are scarce, and those that do exist seem to report anomalous

SMC behavior at lengths below $N = 6$ [25, 61, 88].

Haiss *et al.* explored a chain length range of $N = 3$ –12 under air, dry nitrogen, and room-temperature ionic liquids and noticed that as the chain length decreased below $N = 8$, the exponential increase in conductance began to diminish, leading to length-independent conductance values after $N = 5$ [25, 88]. Li *et al.* also witnessed a similar effect when measuring lengths of $N = 5$ –10 in toluene solution. The behaviour could be described accurately by a fit involving a two resistor model, wherein the total resistance of the circuit R_T is given by the series sum of the molecular resistance and an unknown length-independent resistance, R_Ω ;

$$R_T = R_0 \exp(\beta_N N) + R_\Omega, \quad (4.2)$$

Here, R_0 is the molecular resistance at zero methylene units, or “contact” resistance, which should be close to $1/G_0$ if the electronic coupling is strong. Furthermore, at these short chain lengths, Haiss *et al.* observed that the tunnelling current departed from the Simmons model (Section 2.2.1); being lower than expected at high biases. Inclusion of the image potential (Section 2.2.1.1) on the tunnelling barriers failed to account for these effects and no conclusive explanation has been put forth. Reverse engineering of the data (including the image potential) showed that the effective carrier mass would have to increase substantially from about $0.28 m_e$ at $N = 6$ to $1.69 m_e$ at $N = 3$ in order to account for these anomalous trends. It is not clear what this means physically and more rigorous theoretical models and independent experimental investigations are desirable. A systematic study on the effect of chain length on the SMC value and voltage characteristics of ADTs under UHV, otherwise absent from the literature, is presented in this chapter.

4.1.3 Multiple Conduction Groups

In early studies, surprisingly different SMC values were measured for similar molecular systems between different research groups. For example, a value of

1.0 nS was obtained for 1,8-octanedithiol (ODT) when measured with the STM $I(s)$ and $I(t)$ methods (under air) [71], and a value of (0.99 ± 0.07) nS, in agreement with the former, was measured using a method involving a conducting atomic force microscope (AFM) and gold nanoparticles [97]. However, the STM BJ method (in a dilute molecular solution with a toluene solvent) resulted in a value of 19.6 nS [59, 86], which is over an order of magnitude larger than the aforementioned two values. Given the suspected transport mechanism, such wildly different SMC values for the same molecule might not be anticipated, despite the different environmental conditions and techniques used between experiments. Later investigations go on to show that there are a few different reproducible conductance groups; low (A), medium (B), and high (C) [51, 60–62, 88], the origin of which is still a source of dispute in the literature.

Li *et al.* [61] observed the three groups using the STM BJ method under trimethylbenzene and, after DFT modelling, proposed that the groups originated from a combination of different molecular conformers and different sulfur-gold coordination geometry; the B and C groups were attributed to all-trans conformers with both sulfur atoms located at gold atop and bridge sites, respectively, whereas the A group was attributed to molecules with one gauche defect and with atop coordinated thiol-gold contacts. However, presumably, this model makes predictions about the existence of more conduction groups that arise from other combinations of gauche conformers and sulfur-gold contact geometries *e.g.* bridge-gauche-bridge, and these are not generally distinguished or reported in the literature. Moreover, techniques that involve fully stretching the molecules, such as the $I(s)$ and STM BJ methods, may be expected to preclude the measurement of gauche conformers and this has indeed been demonstrated elsewhere [34, 80, 94, 98]. The fact that the A group can still be observed with these methods would thus further diminish the validity the proposed model. Furthermore, in an earlier paper, Lee *et al.* conclude from theoretical calculations that the large differences between the B and C groups could not be accounted for by different sulfur-gold coordination sites alone (atop, bridge, and hollow) [75].

Haiss *et al.* [60] performed a range of experiments investigating the effect of

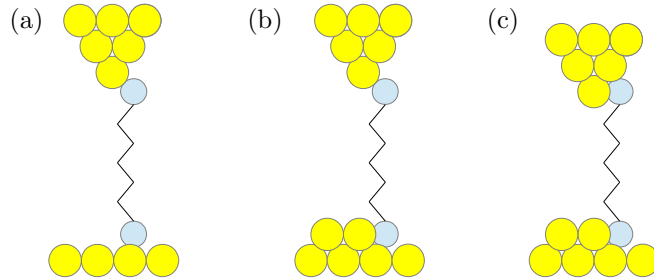


Figure 4.2: Representation of the coordination geometry model proposed by Haiss *et al.* to explain the a) A, b) B, and c) C conduction groups for ADT molecules. For group A, both sulfur atoms contact a single gold atom, whereas for the B and C groups one and both sulfur headgroups, respectively, are located at step edge sites and contact multiple gold atoms. The model predicts that the fully extended length of the junction should decrease by successive multiples of a gold step height (0.236 nm) in going from A to B to C. After Reference [60].

technique and electrode roughness on the relative observation probabilities of the different conduction groups. They concluded that having a high electrode roughness, or using a technique that induces a high electrode roughness *e.g.* STM BJ or high setpoint $I(s)$ measurements, leads to increased B and C group observations relative to the A group. Based on these results, a model was proposed (Figure 4.2) in which the A group is explained by junction formation where both sulfur headgroups are bonded to a single gold atom, whereas the B and C groups originate from junctions where one or both of the sulfur headgroups, respectively, are adsorbed at step edge sites. It was then suggested that the increase in conductance from A to C might be explained by the highly coordinated step edge sites providing either increased sulfur-gold electronic coupling, direct carbon to gold electronic coupling, increased mechanical bridge stability, or a combination of all three. A statistical analysis showed that the distance above the surface at which molecular break off occurs decreased in successive steps of 0.2 nm in going between the groups from A to C; this value is close to the height of a gold monatomic step (0.236 nm) [58] and seemingly corroborates the proposed model.

The three reported conductance groups have been observed during the experiments of this thesis and are presented in this chapter, along with an $I(s)$ break off distance analysis to further explore the validity of the two different models

proposed by Li *et al.* and Haiss *et al.* [60, 61].

4.1.4 Summary

ADTs have a large band gap of 8 – 10 eV and it is thought that the dominant electronic transport mechanism is non-resonant coherent hole tunnelling. The work presented in this chapter seeks to address the lack of a systematic study of the effects of ADT chain length on current-voltage characteristics under UHV; this may help shed light on the anomalous effects observed at short chain lengths in the few studies that investigate full chain length ranges, under other environmental conditions, reported in the literature. Furthermore, the effect of temperature on electronic transport is studied over temperature and chain length ranges that overlap with and extend those investigated elsewhere, with the intention of conclusively proving the apparent transport mechanism. Also, the origin of the multiple conductance groups is addressed via a break off distance analysis.

4.2 Imaging

Figure 4.3 shows constant-current STM images of 1,9-nonanedithiol (NDT) and 1,5-pentanedithiol (PDT) samples obtained several hours after substrate cleaning (Section 3.2.1) and molecular deposition (Section 3.2.3) procedures. The striped regions in the images indicate molecular self-organisation and are consistent with observations reported in the literature for the ADT/Au(111) system [99, 100]. In each case, the periodicity of these regions matches closely to the molecular lengths, implying that the molecules are lying fully-extended on the surface, with both sulfur groups bound to gold atoms, perpendicular to the stripes (the sulfur headgroups) [99]. Leung *et al.* propose a structural unit cell that encompasses a row of three molecules end-to-end, with some sulfur groups located atop gold atoms and others located in bridge and hollow gold sites [99]. (In principle, there should be striped domains oriented in three different directions, corresponding to the symmetrically-equivalent directions on the Au(111) surface; however, in this case, only two orientations can be distinguished clearly in any one image.) However, under this model, it is difficult to understand why the molecules should

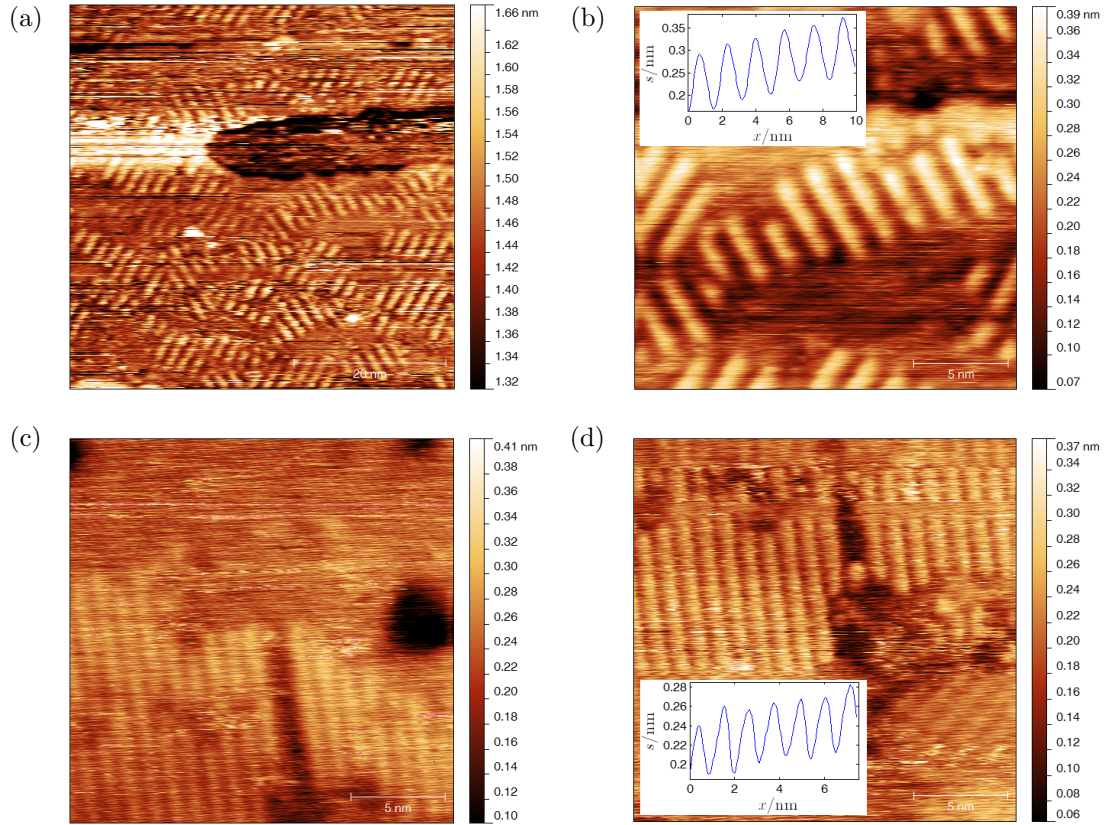


Figure 4.3: STM constant-current images of 1,9-nonanedithiol (NDT), a) and b), and 1,5-pentanedithiol (PDT), c) and d), on Au(111)/mica substrates, obtained with a tungsten tip with current and bias setpoints of 10 pA and 1.5 V, respectively. From the inset line profiles in b) and d), the periodicity of the striped regions is (1.66 ± 0.03) and (1.13 ± 0.02) nm, respectively. These values match closely to the length of NDT (1.64 nm) and PDT (1.13 nm) and imply that the molecules are lying flat and stretched out on the surface, perpendicular to the bright stripes (sulfur headgroups) [72, 73, 99–101].

align themselves in an end-to-end configuration that results in two electronegative sulfur groups residing in close proximity. Indeed, much more recent theoretical calculations by Carro *et al.* indicate that the situation is likely more complicated than the model proposed by Leung *et al.*, and they suggest that a model involving a reconstructed gold surface is more energetically favourable [101]. Essentially, in the newer model, a gold adatom is introduced inbetween the head of one molecule and the tail of the next, such that the electronegative sulfur groups are distanced from one another. If the adatom is indeed present, then the periodicity of the striped regions in Figure 4.3 might be expected to be slightly larger than the length of the molecules (by the width of one gold atom). Interestingly, this does not appear to be the case, as the periodicity of the striped regions closely matches the length of the molecules. Nevertheless, the DFT calculations by Carro *et al.* strongly suggest that the gold adatom is likely to be present and, if so, it may influence the nature of the molecular conductance measurements. For example, if the step edge coordination geometry model is considered (Figure 4.2), then more B conductance group observations might be anticipated, since the adatom increases the sulfur-gold coordination (effectively acting like a step edge). On the other hand, if the sulfur groups are dragged atop the adatoms during $I(s)$ retractions, then more A conductance group observations might be expected. Clearly, the resolution of the images is far too low to allow such a feature to be distinguished.

A surface coverage of roughly 0.5 monolayers or less can be estimated, suggesting that the samples were far from the single monolayer regime. Interestingly, pits can be observed in Figure 4.3c, which may have arisen from either argon ion bombardment or thiol etching during molecular deposition from solution. (It is possible that some pits were formed when gold atoms migrated to form the gold adatom-thiolate surface reconstruction discussed by Carro *et al.* [101].) Leung *et al.* suggest that molecular desorption begins at temperatures exceeding 393 K, thus a limit of 390 K was adhered to for the heating experiments [99]. Images of sufficient quality were not acquired for the other chain lengths. However, given the invariance of the sample preparation procedure, it is reasonable to assume that all the samples had a surface coverage similar to those presented here.

4.3 $I(s)$ Measurements

For each molecular chain length ($N = 3, 4, 5, 6, 8, 9,$ and 10), approximately 7500 $I(s)$ curves were measured at each 0.1 or 0.2 V bias step, over a range of ± 1.5 V. These measurements were then repeated, though typically with a slightly smaller bias range, at low (180 K) and high (390 K) temperature. As such, there are approximately 400,000 curves per molecule and an estimated 2.0 – 3.0 million for the molecular species in total. Since the overarching character of the results is similar for all chain lengths, a case study showing examples of the raw data and analysis procedure for only one molecule is presented here; focus is given to 1,6-hexanedithiol (HDT) due to its intermediary chain length. For the other molecules, unless the raw data is exceptional or instructive, only final processed results are presented.

Figure 4.4 shows an $I(s)$ curve all-data histogram and a histogram after trace selection, along with example selected traces for an HDT sample, measured with a tip bias of +0.2 V at room temperature. Aside from the amplifier saturation and noise peaks, a small molecular current peak (B) at (0.935 ± 0.012) can be distinguished above the background noise in the all-data histogram, and the same peak can be seen clearly at (0.954 ± 0.015) in the filtered histogram. These two values overlap within experimental error, determined by the histogram bin widths, and thus average to give (0.945 ± 0.010) , or (44 ± 1) nS. The all-data histogram shown here is atypical insofar as they did not usually present distinguishable molecular peaks; heavy trace filtering, with an acceptance rate around 1 – 3%, was almost always required to observe current peaks. The conductance value stated here corresponds most closely to the medium (B) group values reported for HDT elsewhere [25, 51, 61, 81, 88, 91]. However, it is still typically 10 – 20 nS higher than reported literature values and this discrepancy will become more evident when the conductance with molecular chain length trend is illustrated (Section 4.3.3). The “shoulder” at roughly 1.7 on the horizontal axis arises from a failure of the data to fully saturate the amplifier, evident in Figure 4.5a.

One of the example traces in Figure 4.4c demonstrates evidence of a two-

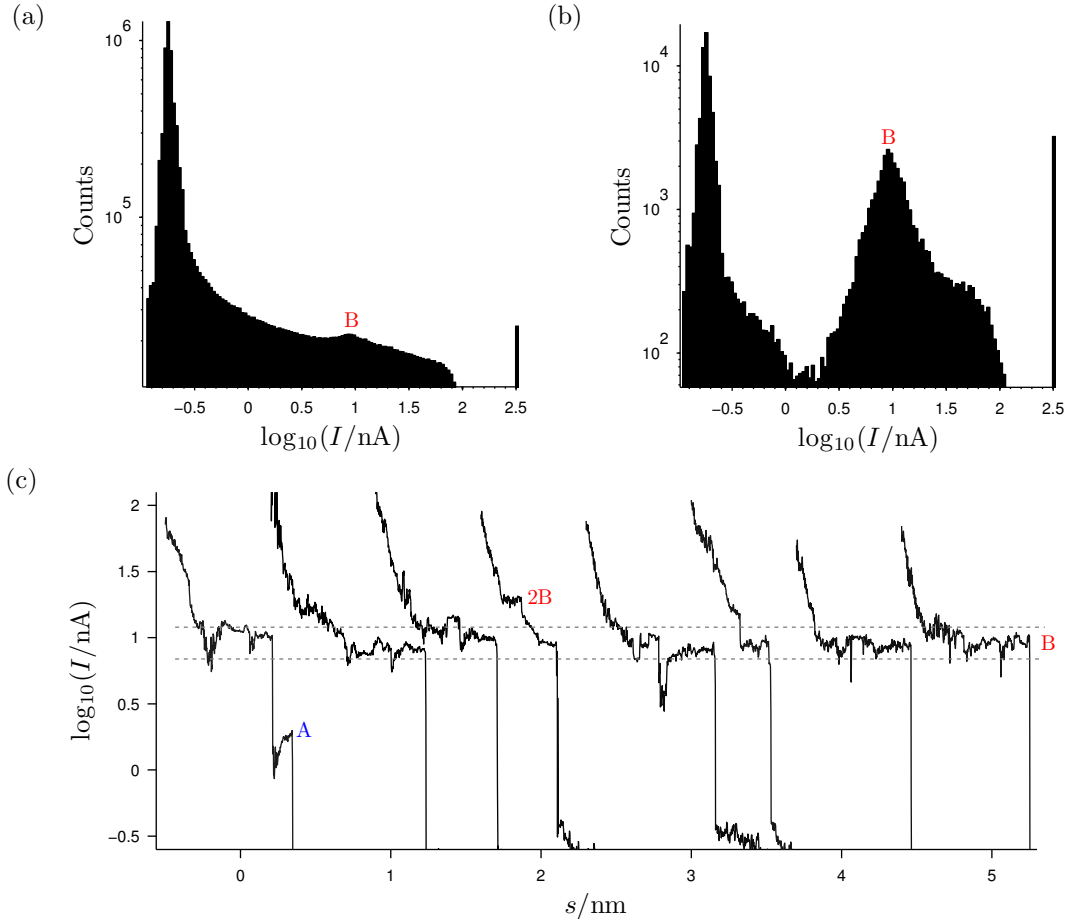


Figure 4.4: a) and b) show logarithmic histograms of $I(s)$ curves for 1,6-hexanedithiol (HDT) before (7500) and after (116) filtering the data set for current plateaus. The measurements were performed at room temperature and the tip bias and initial current setpoints were +0.2 V and 300 pA, respectively; the approach distance from this setpoint was 0.5 nm before a retraction of 2.0 nm at a rate of 5.1 nms^{-1} . The amplifier saturation (333 nA) and noise (0.18 nA) peaks are at the extremes of the histograms and a single molecular current peak (**B**) is present in both cases at (0.945 ± 0.010) , or (44 ± 1) nS. Figure c) shows representative examples of the $I(s)$ traces that were selected to construct the histogram in b). Some traces demonstrate smaller plateaus, corresponding to roughly **2B** ≈ 90 nS and **A** ≈ 8 nS, but these were not numerous enough to form visible peaks in either histogram.

4. ALKANEDITHIOLS

molecule bridge by exhibiting a plateau at approximately $2B \approx 90$ nS [50]. Such many-molecule bridge observations were rare and the corresponding current peaks were usually not visible above the background level in filtered histograms. In this data set, there was only one convincing high (C) conductance group plateau (~ 250 nS) and, arguably, only two belonging to the low (A) group; one of which is shown in Figure 4.4c, labelled A (~ 8 nS). The relative occurrence probability of the three groups witnessed in this example is representative of that for the entire molecular species; in general, only B group plateaus were observed in significant quantities, and A and C group plateaus were extremely infrequent. When present at all, the latter would almost never generate peaks large enough to be distinguished above the noise level of even filtered histograms. Thus, accurate determination of the $I(V)$ characteristics of the A and C groups was essentially impossible; however, it was possible to obtain low bias SMC estimates of these groups for all the molecular chain lengths, albeit from a handful of $I(s)$ curves in cases. The analysis for these groups is discussed further in Section 4.3.3, but in the next section (Section 4.3.1) focus is given to the characteristics of the predominant B conduction group.

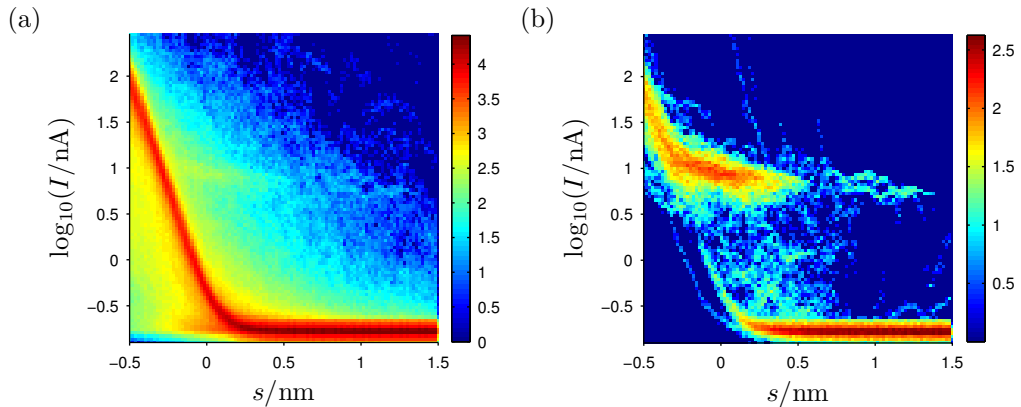


Figure 4.5: Area density plots for the same HDT data set shown in Figure 4.4 a) before (7500) and b) after (116) filtering for current plateaus (+0.2V). The values on the colour bar are the logarithms (base 10) of the bin counts.

The HDT data set discussed in this section can be visualised in the area density (two-dimensional histogram) plots of Figure 4.5. Again, the ubiquitous B

conductance group can just about be distinguished in the unfiltered plot (Figure 4.5a) and can be clearly identified in the filtered histogram (Figure 4.5a). The aforementioned C group plateau can be observed at an ordinate of roughly 1.6 (~ 250 nS). The scarce few A group plateaus cannot be distinguished above noise. These plots can sometimes be useful for judging the overall character of a data set at a glance; however, the false colour scale can sometimes be misleading or confusing.

4.3.1 $I(V)$ Characteristics (B Group)

Figure 4.6 shows further representative $I(s)$ traces and filtered histograms obtained with different tip-sample applied biases from HDT samples. The figure seeks to illustrate that the B conductance peak, isolated at (44 ± 1) nS in Figure 4.4 for a tip bias of +0.2 V, scales with applied bias and produces similar SMC estimates regardless of the polarity of the bias. Moreover, the notion that the A and C fundamental conductance peaks are generally not observed is further evidenced. Indeed, the largest and most obvious peaks in Figures 4.6a (-0.5 V), 4.6b ($+1.0$ V), and 4.6c (-1.5 V) correspond to the B group, being located at (37 ± 4) , (40 ± 1) , and (54 ± 5) nS, respectively. The latter value is slightly higher than the other two due to departure from linear current-voltage characteristics at high biases; this effect is apparent in the $I(V)$ curve for the group (Figure 4.7). The frequency and quality of the plateaus seems to decrease for applied biases of magnitudes exceeding about 1 V, resulting in wider peaks. This was generally the case for all the molecular chain lengths.

Plateaus and peaks at (89 ± 4) and (124 ± 12) nS are also present in Figures 4.6b and 4.6c, respectively, and these are thought to correspond to two B group molecular bridges in parallel [50]. In Figure 4.6b there is also a peak situated at (56 ± 3) nS. The physical origin of this is unknown and there are only a couple of traces with current plateaus that clearly contribute to it; one example of which has been included in the figure and is marked with a red dashed line. Interestingly, this trace exhibits a departure from the exponential decay that seems to fluctuate discretely between the value of (56 ± 3) nS and the slightly lower

4. ALKANEDITHIOLS

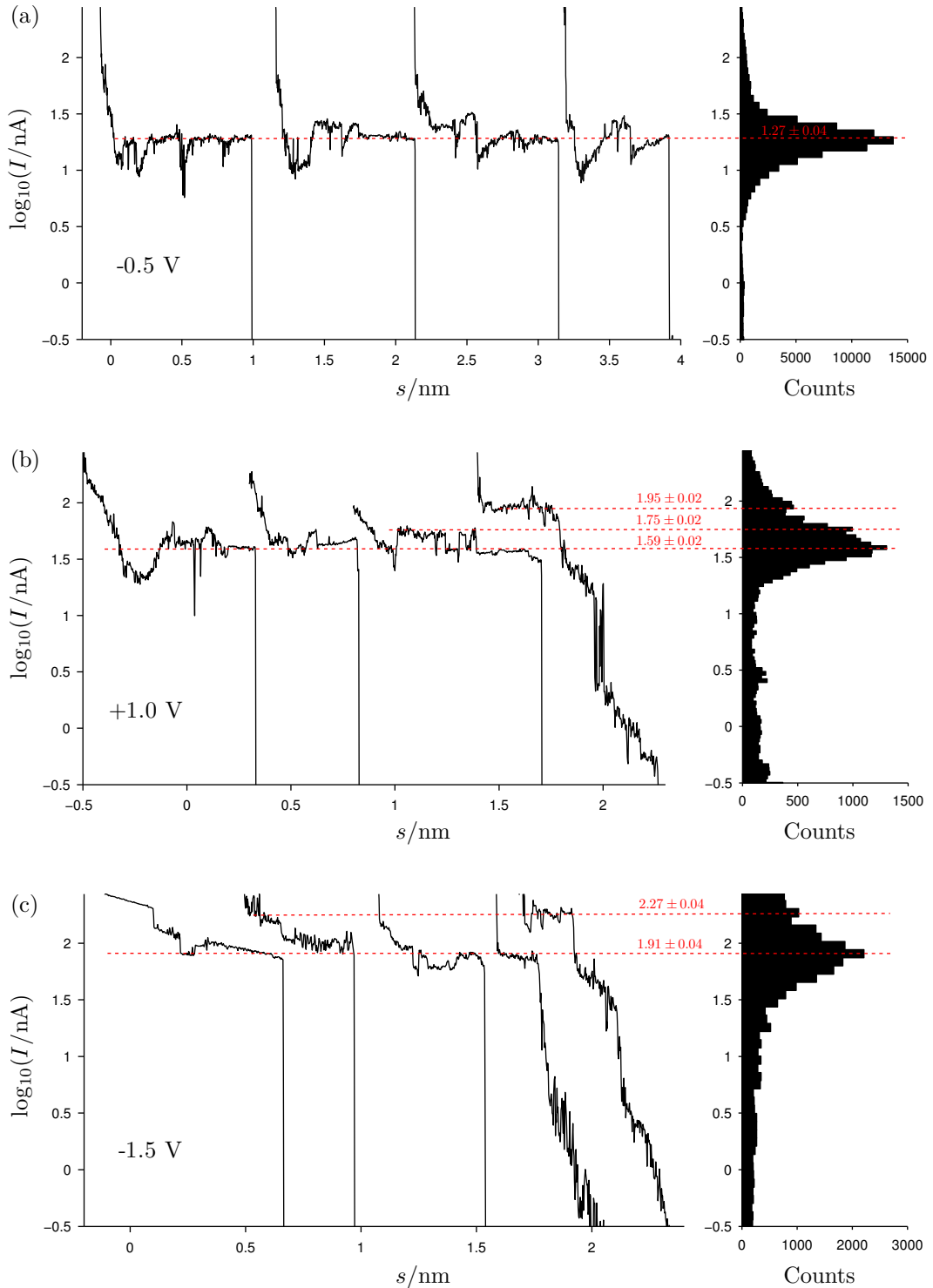


Figure 4.6: Representative $I(s)$ traces and filtered histograms for HDT measured with tip biases of a) -0.5 V (200 traces), b) $+1.0\text{ V}$ (76 traces), and c) -1.5 V (81 traces). Experimental conditions were the same as those stated in Figure 4.4.

B group value of (40 ± 1) nS. Lee *et al.* suggest from theoretical simulations that SMC estimates may be 20 – 30% higher if the sulfur groups are situated in hollow, as opposed to atop, gold sites [75]. Thus, in this case, there may have been alternation between the two coordination geometries during tip retraction, before the system eventually settled into the lower conductance geometry before molecular break off. The tendency of the technique to drag the sulfur groups into atop-atop gold coordinations might also explain the relatively higher observation probability of the low conductance values.

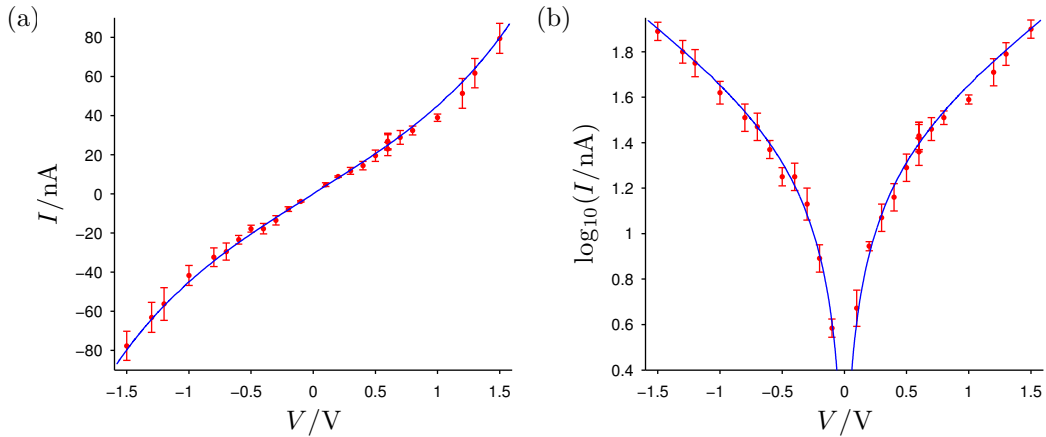


Figure 4.7: The B group $I(V)$ curve for HDT, with a) linear and b) logarithmic current scales, constructed by reading histogram peaks arising from current plateaus on $I(s)$ traces for different applied biases (Figure 4.6). The error bars correspond to the widths of the histogram bin at the center of the peaks. The lines of fit were generated by computation of the quantum mechanical transmission through a rectangular barrier (Section 2.2.2.1) and subsequent integration of this with the Landauer equation (Equation 2.13). The barrier height was 2 eV (above the gold Fermi level of 5.5 eV), the width was set to the length of the molecule (1.26 nm, Equation 4.1) minus 0.169 nm, the effective carrier mass was $0.315 m_e$, and the temperature was 300 K.

Figure 4.7 shows the $I(V)$ curve for the B conduction group of HDT, constructed using the $I(s)$ method; each data point corresponds to the current value of a peak in a filtered histogram, like those shown in Figure 4.6. The logarithmic current axis in Figure 4.7b is more instructive for judging the symmetry of the curve across positive and negative biases, and so subsequent $I(V)$ curves are

displayed in this manner. In order to fit the data, the transmission through a rectangular barrier was calculated (Section 2.2.2.1) and then integrated in accordance with the Landauer equation (Equation 2.13). The barrier height was set to 2 eV (above the Fermi level of the electrodes, taken to be 5.5 eV), based on DFT calculations of the location of the HOMO and LUMO levels performed by other groups [25, 61, 77, 79]. The barrier width was set to the molecular length, $L(N = 6)$ (Equation 4.1), minus a constant of 0.169 nm. With these parameters, a charge carrier mass of $0.315 m_e$ was necessary to fit the data, which is in excellent agreement with theoretical and experimental estimates of the effective hole mass reported in the literature by other groups ($0.28 - 0.36 m_e$) [25, 27, 62, 77, 79, 84, 88, 96].

The choice of barrier shape and width will become apparent after the conductance *versus* molecular chain length trend for the A, B, and C groups are presented (Section 4.3.3), and is also elaborated upon in the discussion at the end of this chapter (Section 4.5). In short, whilst other tunnel barrier shapes (*e.g.* hyperbolic) and widths can be used to produce somewhat reasonable fits to this particular curve, the resulting parameters either do not give agreement with literature values or do not yield suitable conductance *versus* chain length trends, or both. With this foreknowledge, the B group $I(V)$ curves for $N = 3 - 10$ are presented in Figure 4.8, with fit lines calculated using the rectangular barrier model. In each case, all the parameters were identical to those used for HDT, with the exception of the effective charge carrier mass, which was varied slightly between each molecule to achieve better fits. The anomalous characteristics for $N = 4$ at high biases, and the demonstrably higher effective charge carrier mass required for $N = 3$ are addressed in the discussion section for this chapter (Section 4.5).

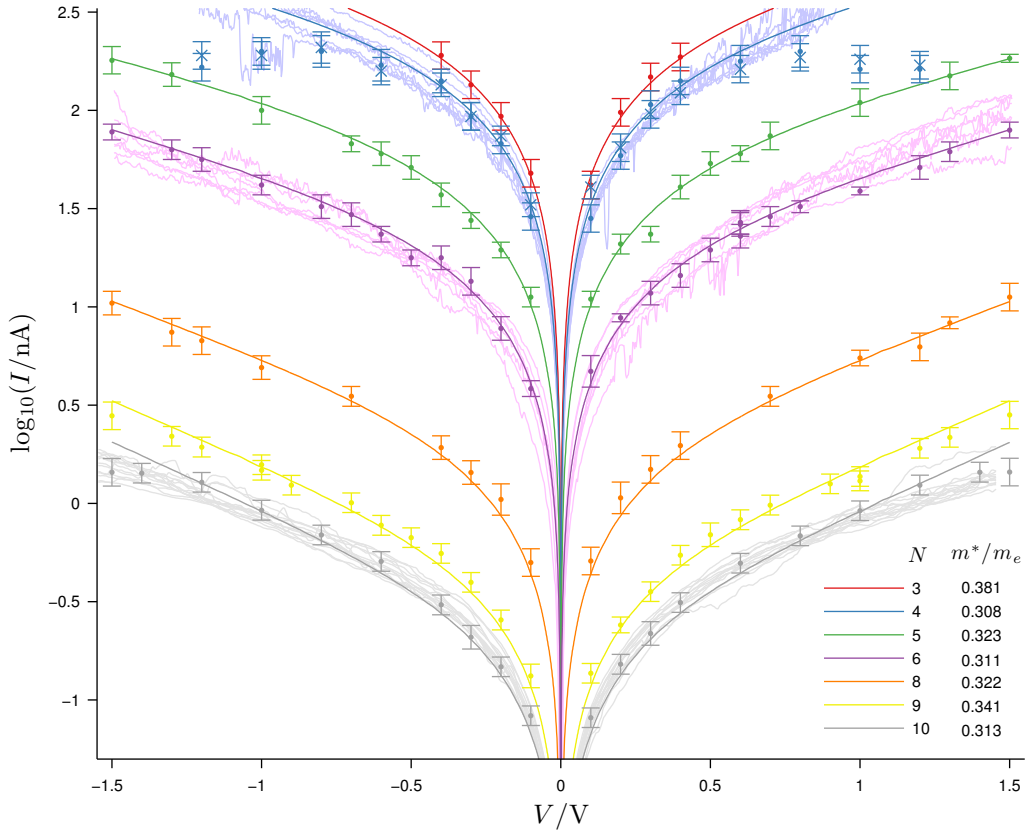


Figure 4.8: The B group $I(V)$ characteristics for different chain length alkanedithiols; $\text{HS}-(\text{CH}_2)_N\text{-SH}$. The data points represent values measured using the $I(s)$ method and the solid lines are theoretical fits achieved by numerical calculation of the transmission through a rectangular barrier (Section 2.2.2.1) and subsequent integration in accordance with the Landauer equation at 300 K (Equation 2.13). The barrier height for all the fits was 2 eV (above the gold Fermi energy of 5.5 eV) and the widths were given by the molecular length, $L(N) = (0.127N + 0.5)$ nm (Equation 4.1), minus 0.169 nm. The effective carrier mass, m^* , was the only free parameter (see legend). For $N = 4$, measurements under dry nitrogen gas have been overlaid (crosses) on the UHV data (circles). The multiple pale traces are the last $I(V)$ curves before break off obtained from the $I(V, s)$ method (see Section 4.4) for $N = 10$ (grey), $N = 6$ (pink) and $N = 4$ (blue).

4.3.2 Temperature Dependence

Figure 4.9 illustrates that the B group $I(s)$ measurements for 1,3-propanedithiol (PrDT) and NDT were temperature-invariant, within experimental uncertainty, over the temperature range of 180 – 390 K; the same was true for the other molecular chain lengths between $N = 3 - 10$. The error bars in the figure correspond to the width of the histogram bin at the center of a peak.

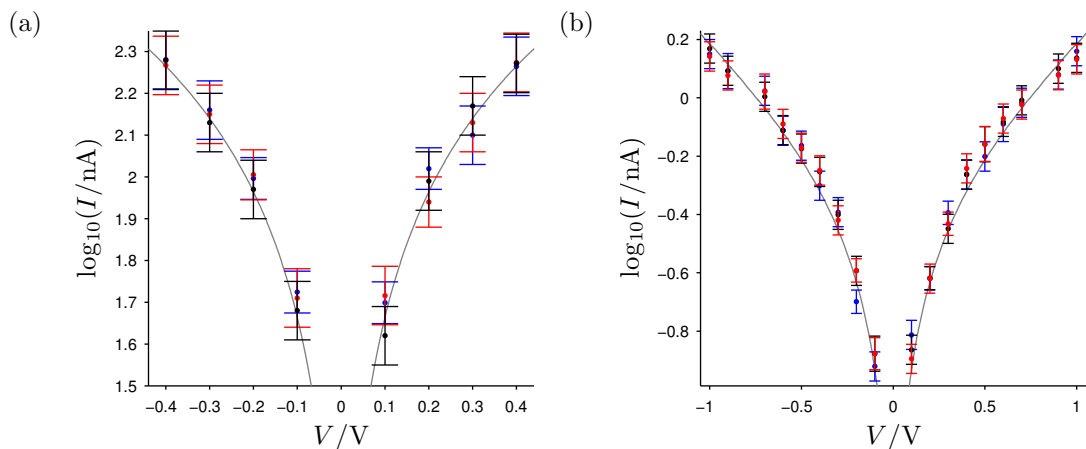


Figure 4.9: The B conduction group $I(V)$ characteristics for a) 1,3-propanedithiol and b) 1,9-nonanedithiol determined by the $I(s)$ method at temperatures of 180 K (blue), 295 K (black), and 390 K (red). The grey lines are the same rectangular tunnel barrier fits shown in Figure 4.8.

4.3.3 Chain Length Dependence

SMC estimates for the A, B, and C conduction groups for ADTs are presented in Figure 4.10 against molecular chain length. The estimates for the B group were measured from the gradients of the linear regions (typically ± 0.7 V) of the $I(V)$ curves shown in Figure 4.8. A and C group plateaus were observed with a frequency over 20 times lower than that of the B group. More often than not, there would not be any plateau observations for these two groups at any one particular bias, and thus accurate determination of the $I(V)$ characteristics was not possible. However, there were enough plateaus for each group across all the measured biases in total ($\sim 20 - 30$ per molecule) to obtain SMC estimates. For

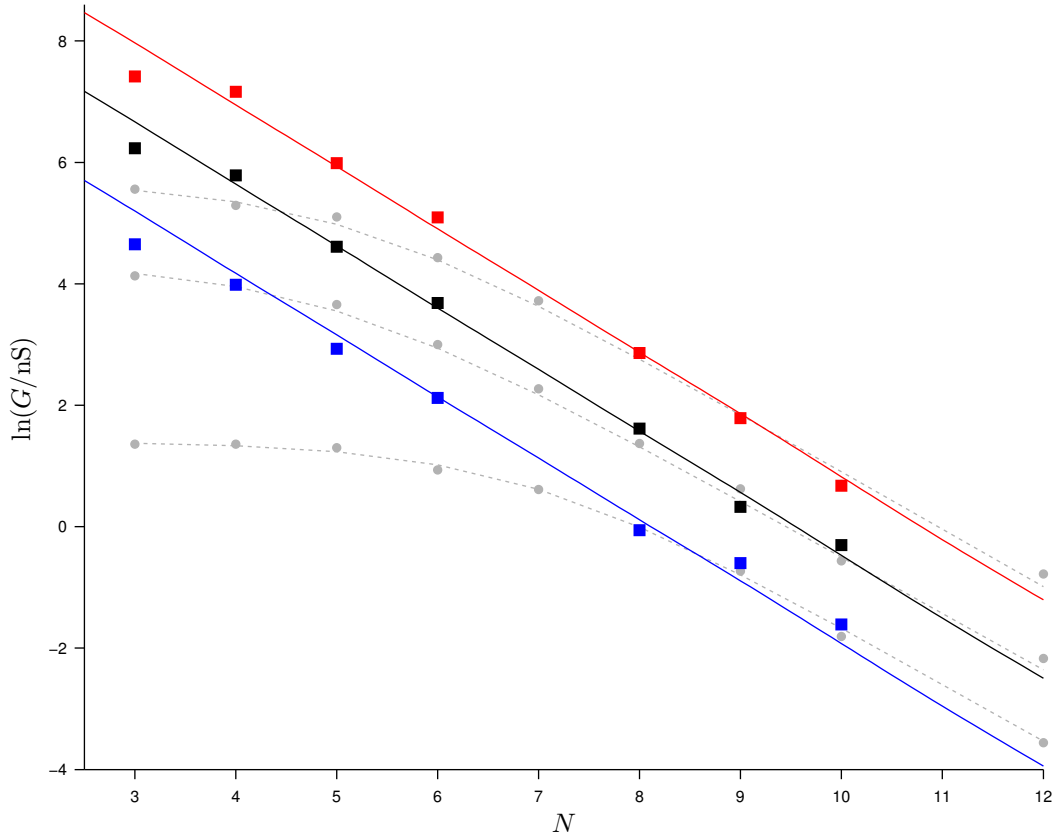


Figure 4.10: Variation of the A (blue), B (black), and C (red) alkanedithiol molecular conduction groups with chain length, measured by the $I(s)$ method under UHV. The data were modelled by numerical calculation of the quantum mechanical transmission through a rectangular barrier (Section 2.2.2.1) followed by integration with the Landauer equation (Equation 2.13) at a temperature of 300 K and an applied bias of 0.6 V. The barrier height (2 eV above the gold Fermi level of 5.5 eV) and effective charge carrier mass ($0.32 m_e$) were fixed between the different conduction groups. Only the barrier width varied, which was set at the full molecular length, $L(N) = (0.127N + 0.5)$ nm (Equation 4.1), for the A group, and reduced by successive multiples of 0.169 nm for the B and C groups. Departure of the conductance from exponential behaviour at short chain lengths is much less pronounced than that observed by Haiss *et al.* under air, dry nitrogen gas, and room temperature ionic liquids (grey circles) [25, 88].

each molecular chain length and group (A and C), the end current value(s) of the plateaus obtained at biases in the linear $I(V)$ regime were measured, converted into conductance values, and binned into a single conductance histogram; the A and C data points in Figure 4.10 thus correspond to peak readings from such histograms. (The decision to read only the end points of the plateaus when constructing histograms, as described in Section 3.3.1.2, was made in order to reduce histogram noise arising from low quality A and C group plateaus.) Examples of $I(s)$ traces exhibiting A and C group plateaus are shown in Reference [102].

The lines of fit were generated using the same rectangular barrier model used for fitting the B group $I(V)$ characteristics in Section 4.3.1 (see Figure 4.8). Again, the barrier height was fixed at 2 eV and, with the width fixed at the full molecular length (Equation 4.1), an effective charge carrier mass of $0.32 m_e$ was necessary to fit the A group data; this value is in excellent agreement with the average value calculated from B group $I(V)$ characteristics for $N \geq 4$, $(0.32 \pm 0.02) m_e$, and hence is in excellent agreement with theoretical and experimental literature values [25, 27, 62, 77, 79, 84, 88, 96]. Since the gradients for all three groups were almost equivalent, the only way the B and C conduction groups could be fitted, without changing the barrier height, was to adjust the barrier width. Hence, these two groups were readily fitted by subtracting 0.169 nm and 0.338 nm from the initial A group barrier width (full molecular length), respectively. Thus, the reason for the choice of the barrier width when fitting the B group $I(V)$ characteristics should be clear. Linear fits applied to the computed tunnelling barrier lines yield a value of $\beta_N = (1.02 \pm 0.01)$ per methylene unit, or $\beta = (0.80 \pm 0.01) \text{ \AA}^{-1}$, for all three conductance groups, consistent with theoretical predictions [74–80] and within the spread of experimental values, $\beta_N = (1.0 \pm 0.2)$, measured for long molecules ($N > 5$) in other media [25, 49, 51, 59, 61–63, 81, 83, 84, 88, 93, 95, 96]. The anomalous data reported by Haiss *et al.* (Section 4.1.2) has been overlaid on Figure 4.10 (grey circles) with two resistor model fit lines (Equation 4.2); the discrepancy between the two data sets is discussed in Section 4.5.

4.3.4 Break off Distance

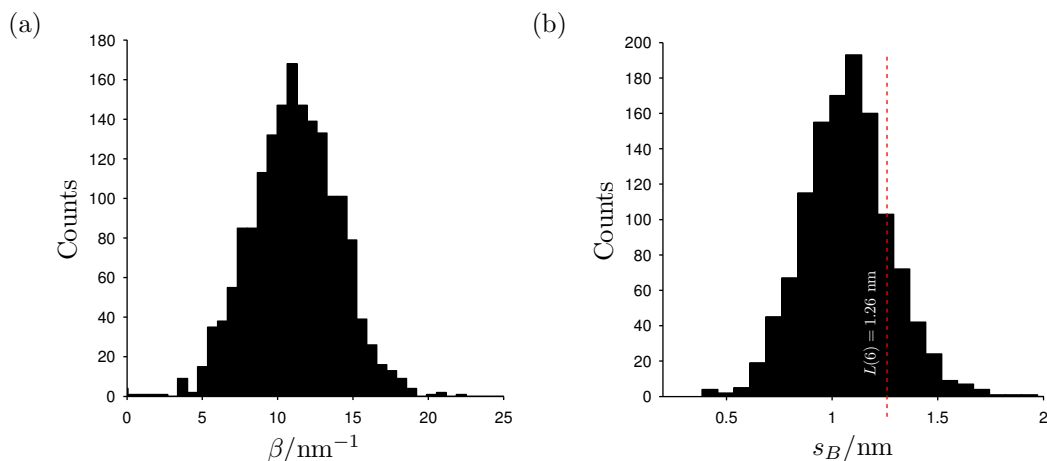


Figure 4.11: a) Histogram of the gradients of the linear regions of the natural logarithm of featureless $I(s)$ curves (2000) over an HDT sample (similar to Figure 3.5). The peak value suggests $\beta = (11.0 \pm 0.3) \text{ nm}^{-1}$. b) Histogram of the tip-sample separation distance at which molecular break off occurs (s_B), constructed by measuring the distance values of the last points on $I(s)$ plateaus (295 K). Distance calibration was performed using Equation 3.1 with the β value from a). There was no observable break off distance trend with bias, so the readings for all measured biases ($\pm 1.5 \text{ V}$) have been included in the same histogram (~ 1500). The peak at $s_B = (1.10 \pm 0.03) \text{ nm}$ corresponds to the B group. The red dashed line is the molecular length of HDT; 1.26 nm .

The tip-sample separation at the point of molecular break off, s_B , during $I(s)$ traces was analysed statistically, to gain information about bridge contact geometry. The tip distance relative to the initial setpoint was converted into a distance relative to the sample surface using the method outlined in Section 3.3.1.2. Figure 4.11a shows an example histogram used to estimate the decay constant, β , for an HDT sample required for the calibration. Figure 4.11b is a calibrated break off distance histogram for the same sample. The clear peak at $(1.10 \pm 0.03) \text{ nm}$ arises from B conduction group plateaus. This figure is representative of those for other chain lengths; when all the plateaus were considered, only the signal from the B group could be observed. Hence, the B group break off values for the species, determined from such histograms, are listed in Table 4.1, with comparison to the full molecular length, L (Equation 4.1).

4. ALKANEDITHIOLS

Table 4.1: Decay constants (β) measured above alkanedithiol samples and $I(s)$ break off distances (s_B) for the B conduction group.

N	β/nm^{-1}	L/nm	s_B/nm	$(L - s_B)/\text{nm}$
3	12.5 ± 0.3	0.88	0.72 ± 0.05	0.16 ± 0.05
4	11.6 ± 0.1	1.01	0.86 ± 0.02	0.15 ± 0.02
5	11.7 ± 0.2	1.14	0.97 ± 0.03	0.17 ± 0.03
6	11.0 ± 0.3	1.26	1.10 ± 0.05	0.16 ± 0.05
8	10.0 ± 0.3	1.52	1.34 ± 0.05	0.18 ± 0.05
9	10.8 ± 0.2	1.64	1.47 ± 0.02	0.17 ± 0.02
10	9.8 ± 0.3	1.77	1.60 ± 0.03	0.17 ± 0.03

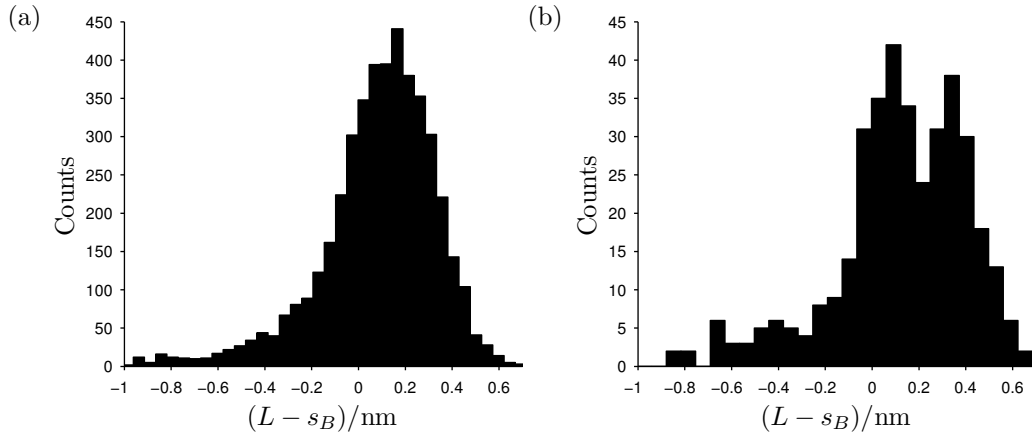


Figure 4.12: a) Histogram of molecular length, L (Equation 4.1), minus $I(s)$ break off distance, s_B , for all molecular lengths and applied biases (comprising about 50% of the room temperature plateaus; ~ 5000 break off values). The clear peak at (0.17 ± 0.02) nm is the signal from the B conduction group. Figure b) is similar to a), but the B group data has been removed *i.e.* it comprises only A and C group data (~ 200 break off values per group). The two principle peak values are (0.09 ± 0.03) and (0.34 ± 0.03) nm, corresponding to the A and C groups, respectively.

In Figure 4.12a the break off distance data for all molecular chain lengths has been combined into one histogram by considering the difference between the break off values and the full molecular lengths ($L - s_B$). The peak from the B group is visible at (0.17 ± 0.02) nm and other peaks from the A and C groups cannot be distinguished, despite such data being present. The small occurrence probability of the A and C group plateaus means that individual break off distance estimates for each chain length were unreliable. However, similar to Figure 4.12a, estimates relative to the full molecular lengths could be made for the two groups by combining the A and C data across all chain lengths (Figure 4.12b). The two peaks at (0.09 ± 0.03) nm and (0.34 ± 0.03) nm correspond to the A and C groups, respectively. In both of the histograms in Figure 4.12, the small peaks at roughly -0.2 , -0.4 , -0.6 , and -0.8 nm may correspond to molecular break off after formation of atomic gold chains between the sulfur headgroups and the tip or substrate during retraction.

4.4 $I(V, s)$ Measurements

The novel $I(V, s)$ method, described in Section 3.3.1.3, was employed to study the $I(V)$ characteristics of the ADT species. The additional time taken to perform voltage sweeps at each distance step means that the average retraction speed for this method is typically significantly lower (0.1 nms^{-1}) than that for the $I(s)$ method ($\sim 5 \text{ nms}^{-1}$). Thus, to rule out the influence of retraction speed when comparing the two methods, room temperature $I(s)$ measurements were repeated on HDT and the SMC estimates were found to be invariant for retraction speeds between 0.1 and 15.0 nms^{-1} .

Figures 4.13 and 4.14 show example $I(V, s)$ measurements for NDT and 1,4-butanedithiol (BDT). Both figures show clear evidence of molecular bridge formation and, moreover, switching between A, B, and C conduction groups. There is excellent agreement between the theoretical fit lines, generated using the rectangular tunnel barrier model proposed for the $I(s)$ data in Section 4.3, and the $I(V)$ data in both cases. Such measurements were performed on ADT chain lengths of $N = 3, 4, 5, 6, 8, 9$, and 10 . In each case, several convincing positive

results similar to those shown in these figures were obtained, which again gave excellent agreement with the theoretical fits suggested from the $I(s)$ data. These full $I(V, s)$ data sets have been omitted for brevity, but B group examples of the last $I(V)$ curves before molecular break off have been overlaid on the $I(s)$ data in Figure 4.8 for $N = 4, 6$, and 10 . (An additional full example for ODT is shown in Figure 3.6). A gap separation analysis was performed on the $I(V, s)$ data yielding an average difference between molecular length and break off distance of (0.0 ± 0.1) , (0.19 ± 0.04) , and (0.37 ± 0.04) nm for the A, B and C group, respectively. These values agree with those derived from the $I(s)$ method within experimental uncertainty (Section 4.3.4).

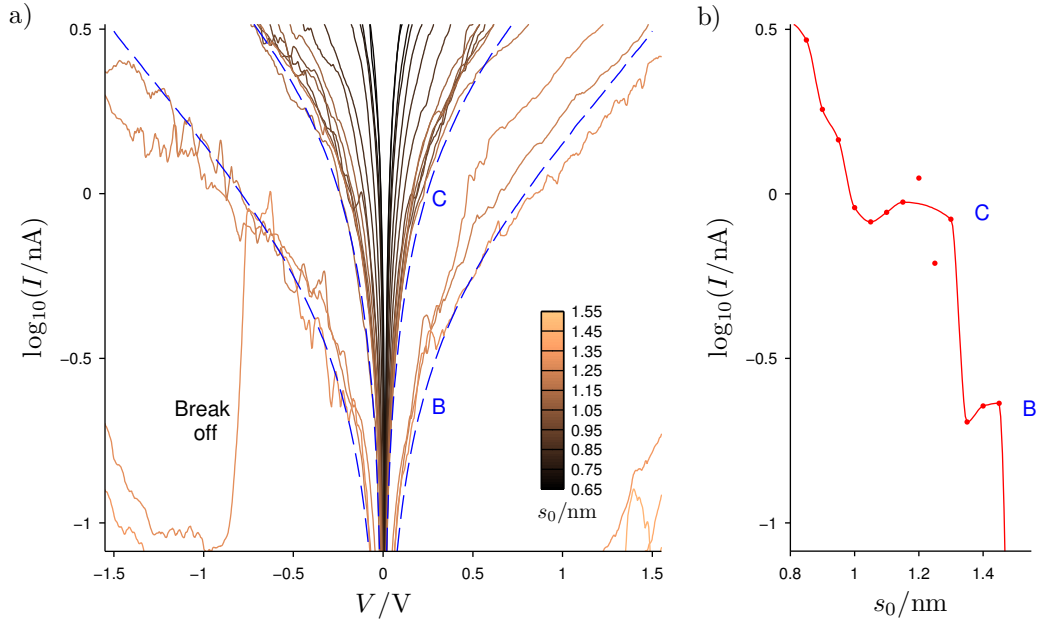


Figure 4.13: a) An $I(V, s)$ measurement performed on NDT. The tip approached the surface by 0.5 nm from a setpoint of -1.6 V and 0.5 nA before being retracted in 0.05 nm steps. The $I(V)$ curves shown are the retraces from 1.6 to -1.6 V at each step; the forward traces from negative to positive bias have been omitted for clarity. The distance scale was calibrated using Equation 3.1 with $\beta = 10.8 \text{ nm}^{-1}$ (see Table 4.1). The blue dashed lines, B and C, are the theoretical $I(V)$ curves for the B and C conduction groups calculated using the model determined from the NDT $I(s)$ data in Section 4.3 (identical parameters). During retraction, the $I(V)$ set first converges to the C group curve, before converging to the B group curve. Spontaneous molecular break off can then be observed during one of the traces following the B group curve at $s_0 = (1.50 \pm 0.05) \text{ nm}$, and the remainder of the curve set reside close to zero current. Figure b) shows an $I(s)$ curve, fitted with a smoothing spline, obtained by sampling each $I(V)$ curve in a) at a bias of -0.2 V. The two current plateaus result from the convergence of the $I(V)$ curves to the C and B molecular conductance states and these terminate at (1.35 ± 0.05) and $(1.50 \pm 0.05) \text{ nm}$, respectively.

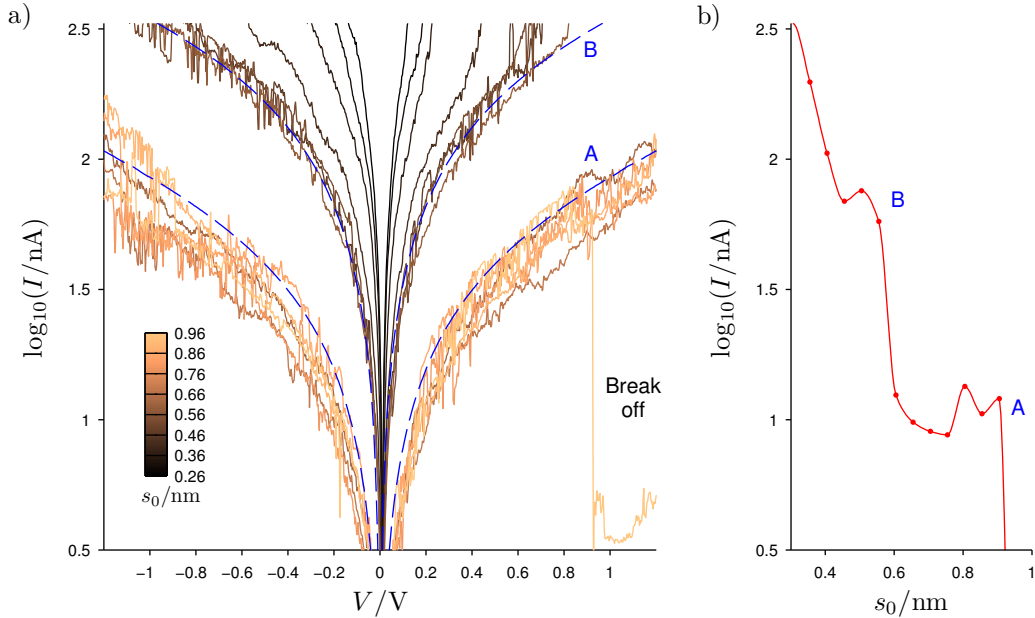


Figure 4.14: a) An $I(V, s)$ measurement performed on 1,4-butanedithiol (BDT). The tip approached the surface by 0.5 nm from a setpoint of -1.2 V and 0.5 nA before being retracted in 0.05 nm steps. The $I(V)$ curves shown are the traces from -1.2 to 1.2 V at each step; the retraces from positive to negative bias have been omitted for clarity. The distance scale was calibrated using Equation 3.1 with $\beta = 11.6 \text{ nm}^{-1}$ (see Table 4.1). The blue dashed lines, A and B, are the theoretical $I(V)$ curves for the A and B conduction groups calculated using the model determined from the BDT $I(s)$ data in Section 4.3 (identical parameters). During retraction, the $I(V)$ set first converges to the B group curve, before converging to the A group curve. Spontaneous molecular break off can then be observed during one of the traces following the A group curve at $s_0 = (0.91 \pm 0.05) \text{ nm}$, and the remainder of the curve set reside close to zero current. Figure b) shows an $I(s)$ curve, fitted with a smoothing spline, obtained by sampling each $I(V)$ curve in a) at a bias of -0.2 V. The two current plateaus result from the convergence of the $I(V)$ curves to the B and A molecular conductance states and these terminate at (0.56 ± 0.05) and $(0.91 \pm 0.05) \text{ nm}$, respectively.

4.5 Discussion

The derived $I(V)$ characteristics and SMC values for chains between $N = 3$ and $N = 10$ were temperature-independent between 180 K and 390 K; Figure 4.9 shows example data for the B conduction group of NDT and PrDT at three selected temperatures. (The $I(s)$ break off distances were also temperature independent). Because the $I(s)$ method measures molecules in their extended conformation at break off, this rules out possible temperature dependence originating from conformational flexibility [34]. It should be mentioned that $I(s)$ plateaus measured at low temperatures were far noisier than those measured at room or elevated temperatures, and this most likely arises from the clamping block and copper braid that must be coupled to the sample stage during cooling experiments, but are otherwise absent. The experiments conducted here overlap with and extend the temperature and chain length ranges studied by Wang *et al.* ($N = 8 - 16$ and 80 - 300 K, single monolayer devices under nitrogen gas), Akkerman *et al.* ($N = 8 - 14$ and 199 - 300 K, single monolayer devices under UHV), and Song *et al.* ($N = 8 - 12$ and 4.2 - 90 K, single molecule junctions in electromigrated nanogaps under helium gas), with the measured SMC values of the latter matching closely to the B conductance group reported here [49, 92, 93]. The temperature invariance strongly suggests that non-resonant coherent tunnelling is the dominant transport mechanism, confirming the existing theory. The temperature dependence of the A and C groups was not analysed as thoroughly as that for the B group *i.e.* investigation of the full $I(V)$ characteristics, but comparison of such plateaus at different temperatures seems to indicate that the A and C groups are indeed also invariant with temperature. Moreover, if the coordination geometry model proposed by Haiss *et al.* is correct, then there is no reason to believe that their temperature behaviour should be any different from that of the B group [60]. If the model proposed by Li *et al.* is correct, then A group observations should be expected to become more numerous with increasing temperature as the population of molecules with gauche defects increases [34, 61]. However, for reasons already outlined in Section 4.1.3 the validity of this model is questionable.

The three reproducible conductance groups; A, B, and C; reported in the liter-

ature were observed during both $I(s)$ and $I(V, s)$ investigations for all the studied ADT chain lengths [51, 60, 60–62, 88]. However, B conduction group plateaus were observed with a frequency over twenty times higher than that of A and C group plateaus. As mentioned in Section 4.1.3, Haiss *et al.* demonstrated that an increased step edge density and/or sample roughness led to increased observation of B group plateaus over A group plateaus when employing the $I(s)$ method, and that C group observations were only significant in number if the STM BJ method was employed [50, 60]. Thus, if the proposed coordination model is correct (Figure 4.2), it could be concluded that either the samples studied for this thesis were very rough or that the fairly high setpoint conditions meant that the sulfur group had a tendency of being pushed up the tip (which is rough by definition) to a high gold coordination site. Given the high flatness of the surfaces deduced from imaging, the latter explanation is more likely to be correct and, if so, this could be investigated by variation of the initial setpoint conditions. In the former case, surface roughness could arise from either argon ion bombardment or from thiol etching during molecular deposition from solution (Section 4.2). These effects could be investigated by annealing the samples at higher temperatures and cooling more slowly to encourage surface ordering, or by using molecular beam deposition under UHV instead of solution deposition (but the facilities at Cardiff University did not allow for this). A further possible explanation for the prevalence of the B group was alluded to in the discussion of surface imaging in Section 4.2; if the surface model suggested by Carro *et al.* is correct [101], then each sulfur group is bound to a gold adatom, which may effectively mimic a step edge sulfur-gold coordination geometry and lead to B group conductance observations.

The B group $I(V)$ characteristics and conductance against chain length trend for all three conduction groups were best modelled by considering the quantum mechanical transmission through a simple rectangular tunnel barrier. The barrier height was fixed at 2 eV (as suggested by the literature [25, 61, 77, 79]), and the barrier width was given by the full molecular length (Equation 4.1) for the A group, and subsequently reduced by one and then two multiples of roughly 0.17 nm for the B and C groups, respectively. With these parameters, the effective charge carrier mass required to fit the B group $I(V)$ characteristics were spread

around $(0.32 \pm 0.02) m_e$ for $N > 3$ and the single value of $0.32 m_e$ gave the best fit to the conductance *versus* chain length trend of all three groups; these values are in excellent agreement with theoretical and experimental reports elsewhere [25, 27, 62, 77, 79, 84, 88, 96]. The A and C group $I(V)$ characteristics were not fully mapped using the $I(s)$ method, but theoretical lines could be generated from the proposed model and these gave superb agreement with A and C group $I(V)$ curves obtained from the $I(V, s)$ method when present.

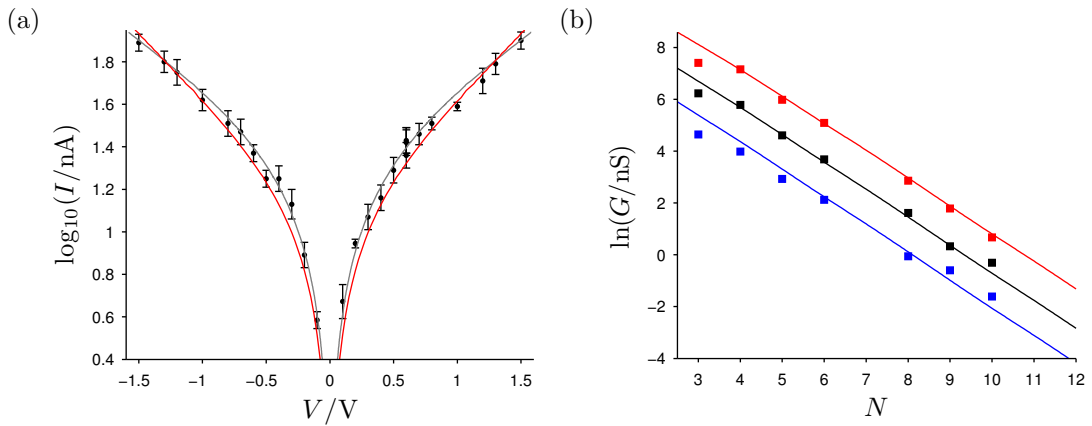


Figure 4.15: a) The B conductance group $I(V)$ characteristics for HDT with the best hyperbolic barrier model (red) and rectangular barrier model (grey, Figure 4.7) fit lines. b) Conductance against molecular chain length trend for the A (blue), B (black), and C (red) conductance groups with lines of best fit generated using the same hyperbolic barrier model as in a) under an applied bias of -0.6 V. The other relevant parameters are described and discussed in the text.

The influence of the image potential was also examined by calculating the transmission through a hyperbolic barrier shape [20]. (See Section 2.2.1.1). Figure 4.15a shows the best fit that could be generated for the B group $I(V)$ characteristics of HDT using the hyperbolic barrier model. Using Equation 2.7, the initial width (d_0) was set to the full molecular length (Equation 4.1), the initial height (ϕ_0) was set to 2 eV [25], and ϵ_r was set to 2.1 [25]. With these parameters, an effective charge carrier mass of $0.395 m_e$ was required to produce the line of best fit. This carrier mass value is substantially larger than the value suggested by the literature ($\sim 0.30 m_e$, [25, 27, 77, 79, 88, 96]). Moreover, the best fit line

from the hyperbolic barrier model seems to slightly underestimate the current at low biases and thus is decidedly worse than that of the rectangular barrier model; similar behaviour to this is observed when the hyperbolic barrier model is applied to the B group $I(V)$ characteristics of the other molecular chain lengths. Figure 4.15b shows the conductance *versus* chain length trend for the three conductance groups. For the B group line, the parameters used were identical to those used for Figure 4.15a. With all else constant, the A and C group lines were then generated after the addition and subtraction, respectively, of 0.17 nm to the initial barrier width. Whilst the lines appear to give reasonable fits to the data, the assumed barrier widths do not match the anticipated widths and so the validity of the model is questionable *i.e.* the assumed initial barrier width for that of the A group is 0.17 nm larger than the actual length of the molecule. If instead the initial width is set to the full length of the molecule for the A group, and the B and C groups are modelled by reducing this width by successive multiples of 0.17 nm, then the effective charge carrier mass must be further increased (away from the literature value) and the resulting fits to the $I(V)$ data become qualitatively worse. Thus, this model did not yield satisfactory $I(V)$ characteristics or conductance *versus* chain length trends for any reasonable parameters and the rectangular barrier model is far more appropriate. Therefore, it is suggested, tentatively, that the effects of the image potential were not significant, at least for $N > 3$ [25].

For $N = 3$, a noticeably higher charge carrier mass of $0.38 m_e$ was required to fit the $I(V)$ curve *i.e.* the gradient of the linear region of the curve was lower than anticipated. This anomaly is reflected in the conductance *versus* chain length trend for all three conduction groups (Figure 4.10); the data conforms closely to the rectangular tunnel barrier lines until a small detraction occurs at $N = 3$. This effect is similar to, but much less pronounced than, that observed by Haiss *et al.* under air and nitrogen [25] (and later verified by the same research group under ionic liquids [88]). Applying the two resistor model (Equation 4.2) to the data presented here shows that the contact resistance, $R_0 = 0.90 \text{ M}\Omega$, and the unknown resistance, $R_\Omega = 0.044 \text{ M}\Omega$, are roughly an order of magnitude lower than those reported by Haiss *et al.* and Kay *et al* [25, 88]. To eliminate the

influence of different media, BDT was examined with the UHV chamber vented with 1 atm of dry nitrogen (it was not possible to vary humidity in the UHV chamber a controllable manner) but no observable difference in the $I(s)$ results was found (Figure 4.8). Therefore, the reason for the discrepancy between the two data sets in Figure 4.10 is unknown. Moreover, the physical origin of the two resistor model itself still remains unclear as its predictions here could not be reproduced by numerically modelling rectangular and other barrier shapes and, as mentioned previously (Section 4.1.2), Haiss *et al.* were also unable to sufficiently explain the trend that they observed. Long *et al.* suggest that hydration of Au-S bonds can reduce the conductance of the system (by reprotonation of the sulfur contacts back to thiol groups), which may possibly explain the trend only if the humidity levels between the nitrogen experiments reported here and by Haiss *et al.* were different [103]. This criterion is more than possible given that Haiss *et al.* purged an air filled container with nitrogen for only 15 hours (Leary *et al.* suggest that nitrogen is not especially effective at purging adsorbed water molecules from gold surfaces and that argon gas should be used instead [104].), whereas the chamber used in this experiment was vented to dry nitrogen after being held at UHV pressures for several months. The chain length dependence presented here is much closer to the anticipated exponential decay model than those reported in any other full chain length investigation elsewhere [25, 61, 88], and the measured decay constant $\beta_N = 1.02$ gives an excellent agreement with theoretical and experimental values for long molecules ($N > 5$) in other media [25, 49, 51, 59, 61–63, 74–81, 83, 84, 88, 93, 95, 96].

$I(s)$ measurements for BDT ($N = 4$) also exhibit anomalous behaviour at high biases (> 0.4 V), no longer agreeing with the theoretical fit or the directly-measured $I(V, s)$ values. Again, this observation is similar to that reported by Haiss *et al.* [25]. Current adapter limitations meant that it was not possible to confirm whether this anomaly persisted for $N = 3$, but it is suspected that this effect and the reduced conductance for $N = 3$ likely have the same origin. The $I(V)$ curve for BDT could not be accurately fitted with the quantum mechanical transmission program for any barrier shape. However, it could be fitted almost perfectly using the image potential corrected Simmons equation (Section 2.2.1.1)

with an initial barrier height and width of 1.81 eV and 0.45 nm (respectively), an effective area of 0.525 nm², and $\alpha = 0.577$ ($m^* = 0.332 m_e$). Whilst the height and effective mass values seem sensible, the applicability of this approach is called into question by the fact that the barrier width is over two times smaller than the molecular length and the effective area is over twice the size of that proposed elsewhere for a single molecule on an Au(111) surface [25]. Furthermore, it would be difficult to understand why a model that relies on more assumptions and heavy approximations should be valid when the more exact numerical models fail. It should be noted that this model was also considered to model the conductance *versus* chain length trend and was able to fit the data very well, but it seems to break down entirely after $N = 3$, exhibiting an asymptote. Also, as mentioned, this abnormal behaviour at high biases is not observed in results obtained using the $I(V, s)$ method, which thus fit very closely to the simple rectangular barrier model applied to the data for other chain lengths. Given the similarity of the $I(s)$ and $I(V, s)$ methods, the origin of this discrepancy is unclear. It appears that the standard $I(s)$ technique at higher bias underestimates the molecular conductance. One explanation might be that a strong electric field between tip and sample at high bias, which is continuously applied in the $I(s)$ technique but only intermittently during the $I(V, s)$ technique, plays a role. In this sense, $I(V, s)$ might be a ‘gentler’ technique.

The measured differences between the molecular lengths and $I(s)$ break off distances for the B and C group, (0.17 ± 0.02) and (0.34 ± 0.03) nm, provide support for the rectangular barrier model applied in Sections 4.3 and 4.4, in which the width of the rectangular tunnel barrier is reduced by integer multiples of 0.17 nm between the successive conduction groups. Likewise, the B and C group difference values measured from the $I(V, s)$ example in Figure 4.13, as well as the values obtained from statistical analysis on the other positive results, also provide support for this model. The difference value for the A group determined from the $I(s)$ method, (0.09 ± 0.03) nm, is larger than the anticipated 0 nm. The corresponding value estimated from the $I(V, s)$ analysis, (0.0 ± 0.1) nm, agrees with the expected value albeit within a large uncertainty arising from a small sample size. There may be a genuine tendency for molecules in the A group configuration

to break off at distances slightly smaller than the full molecular length. If so, this might be explained by bridge or hollow site coordinated sulfur groups or by a tendency of the molecules to break off when they are not orthogonal to the surface *i.e* the molecule composes the hypotenuse of a shallow right angled triangle. In any case, the conductance *versus* chain length trend and $I(V)$ characteristics for the A group, as determined from the $I(V, s)$ method, seem to conform incredibly close to the proposed model in which the barrier width is determined by the full molecular length.

The presence of multiple conduction groups on the same $I(s)$ trace or $I(V, s)$ data set reported here seems to lend support to the step edge model proposed by Haiss *et al*; only transitions from higher to lower conduction groups were witnessed, which can be readily explained by the dragging of sulfur headgroups up gold step edges during retraction [60]. However, the fundamental difference value of (0.17 ± 0.02) nm, determined by the $I(s)$ method (and verified by the $I(V, s)$ method), falls considerably short of the gold monatomic step height, 0.236 nm, predicted by this model (Section 4.1.3). Miscalibration of the STM height piezo should be ruled out on the basis that the line profiles taken from the bare gold images (Figure 3.3) yielded monatomic step height values that were in excellent agreement with the accepted value. In the original paper where the model is proposed [60], the average distance between conduction group transitions is stated as (0.20 ± 0.01) nm, which is also decidedly lower than the gold step height. Furthermore, in the two transition distance histograms presented in the paper (distance differences between the ends of C and B plateaus and the ends of B and A plateaus, see Figure 10 of Reference [60]), the exact locations of the peaks are questionable due to the seemingly small (but unspecified) number of data points, but their centers are arguably both closer to roughly 0.19 nm as opposed to 0.20 nm. Moreover, in the two example $I(s)$ traces (shown in the same figure), the distance between the end of the C and B plateaus is roughly 0.13 nm and that between the end of the B and A plateaus is roughly 0.18 nm. Given these factors, the value of 0.17 nm reported here is not too far away from the values implied by the Haiss *et al.* data and it is difficult to see how either relate directly to the height of a gold monatomic step. Despite these concerns, the step edge model is

the strongest candidate for explaining the multiple conduction groups, but there is perhaps slightly more to the picture that might be able to be addressed with sophisticated simulations. Perhaps there is just a propensity toward stretching of Au-S or Au-Au bonds before break off occurs.

In general, the $I(V, s)$ technique gives results in excellent agreement with the theoretical $I(V)$ curves predicted by the rectangular tunnel barrier model used to fit the $I(s)$ data. In addition, the technique is i) far less time consuming than repeating $I(s)$ measurements at different biases for the purposes of obtaining molecular $I(V)$ characteristics, and ii) can give individual molecular $I(V)$ curves. In particular, as illustrated in Figure 4.14, it gives the ability to observe the full $I(V)$ characteristics for multiple conduction groups for an individual molecule followed by very clear evidence of molecular bridge destruction in a single measurement. In Figure 4.14, both the A and B conductance groups can be seen, as well as break off during one of the $I(V)$ traces. The difference in distance between the last B group trace and the last A group trace is approximately (0.35 ± 0.1) nm, which is significantly larger than the average observed for the $I(s)$ and $I(V, s)$ measurements and larger than the monatomic step on Au(111). This suggests that there may be a positional change in the Au atoms bound to the molecule, additional to any change in the binding site of the thiol end group(s), during extension of the molecule. A second interesting feature is that as the distance separation is increased, the individual curves approach the B dashed lines from above (*i.e.* higher current) but the A dashed lines from below (*i.e.* smaller current). This is consistent with the behaviour sometimes seen in standard $I(s)$ measurements where the plateaus show an increase in current just before break off. This might be interpreted in terms of the fully extended molecule at break off showing maximum conductance due to its linear configuration. (A molecular bend will act as a scatterer.)

4.6 Summary

The well-established $I(s)$ method and the novel $I(V, s)$ method were employed to investigate the $I(V)$ characteristics of ADTs over a large temperature (180 –

390 K) and chain length ($N = 3 - 10$) range under UHV, since there seemed to be an absence of such UHV studies from the literature. Three temperature-independent conduction groups were observed, in agreement with existing data and models based on off-resonance coherent hole tunnelling. For $N > 3$, the measured conductance adheres closely to an exponential decay with chain length, with a decay constant in good agreement with theoretical and experimental results in the literature. An effective charge carrier mass of $(0.32 \pm 0.02) m_e$ was determined by modelling the chain length and voltage dependence of the charge transport with a rectangular tunnel barrier of height 2 eV. The barrier width was initially set to the full molecular length to model the low group, and one and two multiples of 0.17 nm, respectively, were subtracted from this width to fit the medium and high group characteristics. This fundamental width reduction value is supported by a robust tip-surface separation analysis, but falls noticeably short of the gold monatomic step height (0.236 nm) predicted by the step edge model [60]. Departure from this rectangular barrier model occurs for $N = 3$, where the SMC value is anomalously low and a slightly higher effective carrier mass of $0.38 m_e$ was required to fit the transport characteristics. The $I(V)$ characteristics as determined by $I(s)$ method (but not with the $I(V, s)$ method) also exhibits anomalous behaviour at high biases for $N = 4$. These anomalies are similar to those observed by Haiss *et al.* under air, but are much less pronounced [25, 88]. The effect itself and the discrepancy between the two data sets is not fully understood, but likely related to hydration of thiol contacts; more sophisticated theoretical modelling is needed to investigate possible reasons for the apparent chain length dependent effective carrier mass. The $I(V, s)$ method gave excellent agreement with the $I(s)$ method, but is much faster for the purposes of discerning full $I(V)$ characteristics. Moreover, being able to observe both the full $I(V)$ characteristics of multiple conduction groups for an *individual* molecule and molecular break off all in one measurement is incredibly compelling.

Chapter 5

Oligothiophenes

In this chapter, single molecule electrical conductance measurements of alkylthiol-terminated oligothiophenes are presented. Since the molecules are structurally related to alkane(di)thiols, the results expounded and explained in Chapter 4 provide a solid base from which to begin understanding their electronic transport properties. Before the results are presented and discussed, the basic properties of the molecules and the important studies that have been conducted upon them are described.

5.1 Introduction

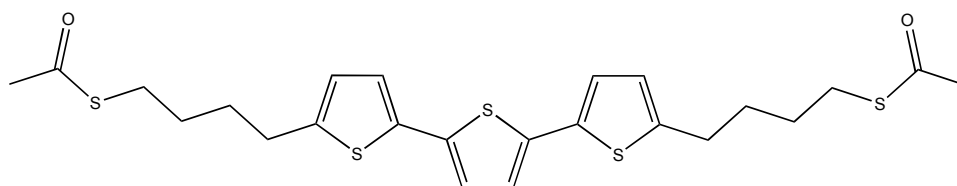


Figure 5.1: Structural diagram of the oligothiophenes studied in this thesis. Let N_1 and N_2 denote the number of methylene units on either side of n conjugated thiophene rings, such that the molecules can be referred to as $N_1 [Tn] N_2$; in this case, 4[T3]4. The acetyl (COCH_3) groups protect the sulfur anchoring groups before solution deposition; in the presence of gold and water, the groups are cleaved and Au-S bonds are formed.

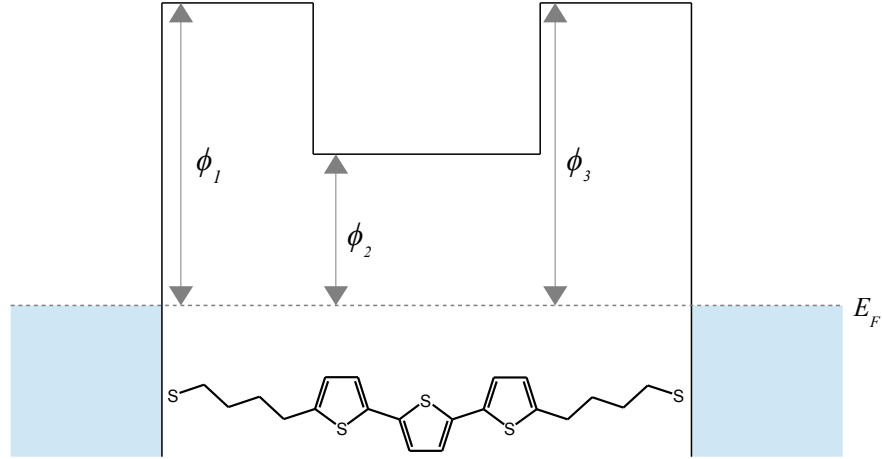


Figure 5.2: An indented tunnel barrier as a candidate for modelling electron transport through oligothiophene molecules with connected alkanethiol chains, drawn with zero applied bias. The parameters ϕ_1 and ϕ_3 describe the height of the barriers above the Fermi level, E_F , presented by the alkanethiol chains and ϕ_2 describes the height of the (shorter) barrier presented by the conjugated ring system.

The oligothiophenes studied in this chapter comprise conjugated thiophene units terminated on either side by alkanethiol chains of varying length. Figure 5.1 shows a structural diagram for these molecules along with a description of the naming convention used in this thesis. Bingqian *et al.* measured roughly 3.4 eV for the HOMO-LUMO gap of the conjugated system of 1[T3]1 from UV-Vis spectroscopy [105], whereas Leary *et al.* report a value of 2.15 eV for 6[T3]6 from DFT calculations [104] (though they note that DFT calculations underestimate the gap size). For reasons discussed in Chapter 2, the gap size should be expected to decrease as the number of thiophene units increases. Indeed, Bingqian *et al.* and Leary *et al.* report values of 3.0 eV and 1.64 eV, respectively, for similar molecules with four thiophene rings. Theoretical calculations suggest that the HOMO for the conjugated system is closer to the Fermi level than the LUMO, and thus is likely responsible for mediating much of the charge transport [104–108]. Given this, the physical structure of the molecules, and the relatively small gap values compared to those of alkanedithiols, one of the simplest anticipated

transport models involves an indented tunnel barrier, illustrated in Figure 5.2 [104, 109, 110].

The transmission through the barrier in Figure 5.2 can be readily investigated using the Python program, discussed in previous chapters (Chapters 2 and 4 and Appendix A). The work presented in Chapter 4 helps to confine the number of free parameters when fitting the experimentally-measured $I(V)$ curves for the molecules; a value of 2 eV is reasonable for ϕ_1 and ϕ_3 eV. Throughout this chapter, each molecular length is approximated by the addition of 0.35 nm per thiophene unit, implied by the literature [104], to the length of the alkanethiol chains given by Equation 4.1. This empirical formula gives length values that are in extremely close agreement with those estimated from recent theoretical modelling (private communication) by the research group at the University of Liverpool [52] and allows the width of each barrier section to be readily defined. Thus, the only free parameters in the model that need to be determined are the barrier height of the central region, ϕ_2 , and the charge carrier effective mass, m^* . To optimise these two parameters, the Python tunnel barrier program was implemented with a non-linear least-squares regression (based on the Levenberg-Marquardt algorithm [111]) with each data point weighted by an error estimate. The regression algorithm provides a covariance matrix that can be used to calculate the standard errors in the fit parameters.

The model proposed here may be overly simplistic and it may be necessary to decouple the central barrier from the other two, and then calculate the total transmission as the product of the individual transmissions for the three separate stages; $T(E) = T_1(E)T_2(E)T_3(E)$. This may be necessary if the effective charge carrier mass in the conjugated system is vastly different from that in the alkanethiol chains (spatially varying mass), or if the energy level mediating the charge transport in the ring system is close enough to the Fermi level such that a single energy level model (Section 2.2.2.2) is more appropriate for calculating $T_2(E)$.

5.1.1 Notable Works

Bingqian *et al.* studied the electrical properties of 1[T3]1 and 1[T4]1 oligothiophene molecules experimentally using a conductive AFM under toluene and found that the conductance of the four-ring molecule, ~ 5.8 nS, was significantly larger than that of the three-ring molecule, ~ 2.17 nS [105]. (Zhang *et al.* report a similar conductance of 1.78 nS for 1[T3]1 using an STM under ambient conditions [112].) The decrease in conductance was attributed to a combination of a reduction in the HOMO-LUMO gap (mentioned previously), and a shift of the HOMO closer to the Fermi level of the electrodes, as the number of rings increased. The latter effect was investigated using an STM-based electrochemical gating technique under aqueous NaClO_4 , wherein the HOMO levels were shifted closer to the electrode Fermi levels by increasing the gate electrode bias voltage (reversibly oxidising the molecules). The conductance of the longer molecule was shown to undergo a rapid increase at a gate voltage roughly 0.2 V lower than that for the shorter molecule, illustrating the relative proximity of the two HOMOs to the Fermi level. This unusual length dependence and proposed explanation is seemingly corroborated by theoretical calculations (DFT and non-equilibrium Green's functions approaches) reported by Zhou *et al.* and later by Tang *et al.* [107, 108]. The former group, as well as others elsewhere [113], investigate the conductance *versus* length trend for other conjugated oligomer molecules, such as oligophenylenes, and find the more common and anticipated exponential decay relationships, suggesting that the HOMO-LUMO gaps for these species are less variable with length. Also worth noting are the large conductance decreases observed by Bingqian *et al.* after the application of stretching forces, which were attributed to an increase in the HOMO-LUMO gap sizes with force rather than simply elongation of the molecules [105]. These redox state and stretching force conductance dependences potentially make the species a viable candidate for molecular switches.

Contrary to the length dependence observed by Bingqian *et al.*, Leary *et al.* performed experimental SMC measurements under dry argon gas and theoretical calculations, based on a non-equilibrium Green's function (NEGF) method,

5. OLIGOTHIOPHENES

and observed a very shallow ($\sim 0.2 \text{ \AA}^{-1}$) conductance decrease as the number of rings increased [104]. Yamada *et al.* and Yutaka *et al.* also observe weak exponential decays, with constants of $\sim 0.1 \text{ \AA}^{-1}$ and $\sim 0.19 \text{ \AA}^{-1}$, respectively, when measuring more structurally complicated oligothiophene molecules by STM under solutions of hexadecane and mesitylene [114, 115]. Furthermore, Peng *et al.* derive a similar exponential decay constant of $\sim 0.211 \text{ \AA}^{-1}$ from a theoretical study on unsubstituted oligothiophenes based on DFT and NEGF approaches [106].

Leary *et al.* also observed large conductance increases when going from the dry argon gas atmosphere to ambient conditions [104]. The reason for this increase was attributed to the interaction between water molecules and the thiophene rings (π system); it was suggested, and demonstrated with theoretical modelling, that the formation of a solvation shell around the thiophene backbones electrostatically gates the molecules, shifting the LUMO transmission resonance very close to the Fermi energy of the electrodes (whilst shifting the HOMO resonance far away) leading to increased conductance. The effect was shown to be more dramatic for molecules with a greater number of thiophene rings (with an increase of two orders of magnitude for the longest chain) since they allow for the presence of a larger number of water molecules in the solvation shell. The effect was shown to compensate for the exponential conductance decrease with ring number, observed under dry argon gas, and led to essentially length-independent conductance values. (The effect was also shown to be fully reversible by the removal of the water, potentially making the molecules excellent candidates for room-temperature molecular sensors.) Thus, hydration state dependence is an alternative explanation for the length dependence observed by Bingqian *et al.* experimentally, though the reasons for the contradictions between the theoretical modelling of the various groups is unclear. After the discovery of this hydration dependence, measurements under UHV, where humidity levels should be far lower than even the argon-purged container reported in [104], are prudent.

Lee *et al.* performed temperature and thiophene unit SMC studies on molecules with oligothiophene backbones, but with several additional functional groups

(heterogeneously substituted) to those studied in this thesis, using an STM under dry argon gas and vacuum (2×10^{-6} mbar) [116]. Their measurements suggest that for each molecular length there exists a critical temperature, below which the conductance is temperature-independent, and above which the conductance exhibits a strong increase with temperature, accurately described by an activation energy model (Arrhenius plot; $\exp[-E_B/k_B T]$). The proposed explanation for this observation is the competition between superexchange tunnelling and thermally-induced hopping *i.e.* tunnelling dominates the electron transport below the critical temperature, whereas thermal hopping dominates above this threshold. The critical temperatures varied such that molecules with lengths shorter than 5.6 nm were almost exclusively dominated by tunnelling at room temperature, whereas longer molecules were dominated by hopping. This explanation is backed by NEGF modelling, but there is a call for more sophisticated simulations and verification by other parties. Taniguchi *et al.* also observe similar behaviour for more structurally simplistic oligothiophene molecules incorporated into gold nanoparticle assemblies, though the measured critical transition temperatures were far lower (7 – 10 K, instead of ~ 350 K) [117].

Very recently, Rattalino *et al.* reported extremely interesting optoelectronic properties of oligothiophenes with short alkanethiol chains attached to each thiophene unit [118]. Using an electromigration induced break junction technique under atmospheric conditions, it was demonstrated that the measured conductance of the molecules can be modulated by changing the ambient illumination. A peak in the molecular conductance was seen when the wavelength of the incoming light was 450 nm (2.76 eV), which was 120% larger than the conductance observed at wavelengths of 300 nm. They suggest that some photo-generated excitons [119] on the thiophene ring system are able to undergo dissociation and subsequently tunnel off the molecule, contributing to the measured conductance. The optoelectronic properties of polymerised thiophenes, such as poly(3-hexylthiophene-2,5-diyl) (P3HT), have been widely studied and utilised as electron donor materials in the field organic photovoltaics [120–125], and these latest experiments now indicate the possibility of exploiting oligomer units to make single molecule optoelectronic devices. The findings also suggest that great care should be taken to

control the ambient illumination when performing conductance measurements; the opaque walls and easily capped windows on the UHV system employed in these experiments allow the background lighting to be kept constant throughout the entire investigation.

5.1.2 Summary

Oligothiophene molecules exhibit extremely interesting molecular conductance trends with length, temperature, redox state, hydration state, and illumination, which potentially make them great candidates for molecular (opto)electronic devices and sensors. Since the conductance is seemingly sensitive to so many factors, a systematic study under the highly-controlled environment of UHV, currently absent from the literature, is imperative. The physical and electronic structure of the molecules suggests that the electronic transport properties might be best modelled by consideration of the transmission through an indented tunnel barrier.

5.2 $I(s)$ Measurements

The oligothiophene molecules studied in this investigation; 3[T3]3, 4[T3]4, 5[T3]5, 6[T3]6, 5[T2]5, and 5[T1]5; were synthesised and provided by the research group of Richard Nichols and Simon Higgins at the University of Liverpool [52]. For each molecule, approximately 5000 $I(s)$ curves were acquired at each 0.2 V bias interval, spanning ± 1.6 V, on both the high and low current amplifiers. The measurements were then repeated at elevated temperatures, up to 390 K. For reasons relating to noise, discussed in the following sections, meaningful data could not be obtained from reduced temperature measurements. Thus, approximately 200,000 – 300,000 traces were measured for each type of molecule and about 1.0 million were measured for the molecular species in total. All-data current histograms were almost always featureless, such that curve filtering was necessary to reveal current peaks originating from plateaus; the curve selection rate was roughly 1 – 3%, which is comparable to that of the ADTs in Section 4.3. In the following sections, an in-depth case study of the data obtained from 4[T3]4 will first be presented, before the data for the other molecules is presented

in a more concise manner.

5.2.1 4[T3]4 Characteristics

Figures 5.3 and 5.4 show representative $I(s)$ traces and the corresponding filtered current histograms for 4[T3]4 obtained at various tip biases (and at room temperature) using the low (0 – 3.3 nA) and high (0 – 333 nA) current amplifiers, respectively. The range of current plateaus observed for the molecule is far larger than that measured for the ADT species; numerous different peaks can often be observed in any given filtered histogram. Despite the large breadth of possible conductance values, only two conduction groups could be measured consistently and reproducibly over the range of applied biases (± 1.6 V) – these invariably produced the largest and most convincing current peaks. The zero-bias ($|V| < 0.6$ V) conductance values of these two groups are approximately 0.09 nS (low, blue) and 5.0 nS (high, red). Both groups were observed on the low amplifier; however, due to the upper current limit of 3.3 nA, the high group was only observed at biases between ± 0.4 V. The noise threshold, 0.18 nA, precluded measurement of the low group on the high amplifier. Many of the other peaks in the histograms can be attributed to integer multiples of these two fundamental groups, implying the formation of many-molecule bridges. Possible explanations for the origin of the other peaks are addressed in the discussion section of this chapter (Section 5.4). In general, the current plateaus, as measured on both adapters, are far noisier and more ill-defined than those measured from ADTs and the associated uncertainties are larger.

Figure 5.5 show example two-dimensional $I(s)$ histograms, before and after filtering traces for current plateaus, measured on both the low and high current amplifiers with a tip bias of +1.0 V. There are no clear features that can be discerned in the all-data histograms (Figure 5.5a and 5.5c). After filtering, both diagrams (Figure 5.5b and 5.5d) exhibit discontinuities (at roughly -1.0 and 1.0 on the respective vertical axes) that arise from current plateaus corresponding to the low and high molecular conductance groups. Again, the molecular signals from the diagrams are far more poorly defined than the analogous diagram

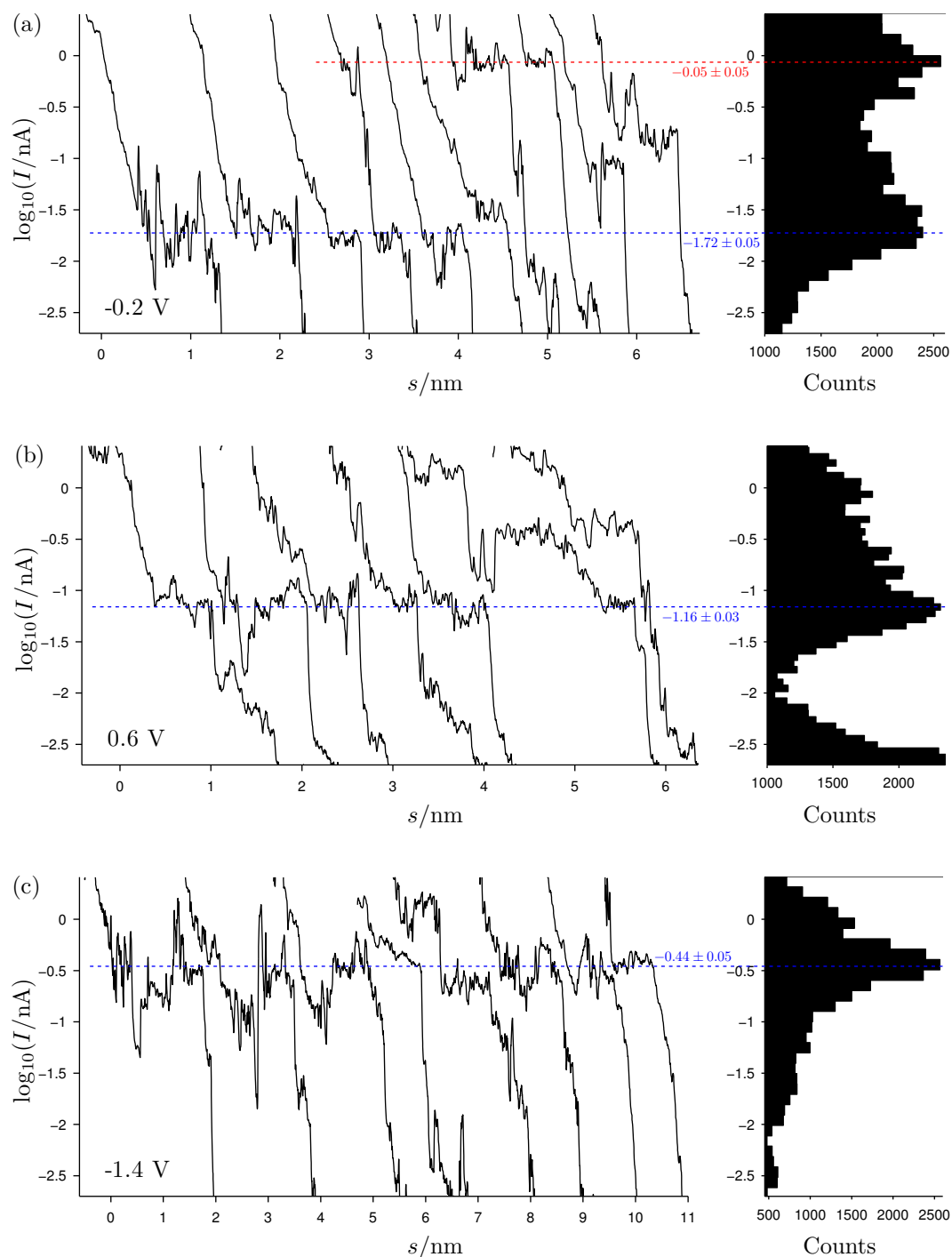


Figure 5.3: Representative $I(s)$ traces and filtered histograms for 4[T3]4, taken at tip biases of a) -0.2 V (175 traces), b) $+0.6\text{ V}$ (123 traces), and c) -1.4 V (59 traces), on the low ($0 - 3.3\text{ nA}$) adapter. Setpoint: 500 pA , approach: 0.5 nm .

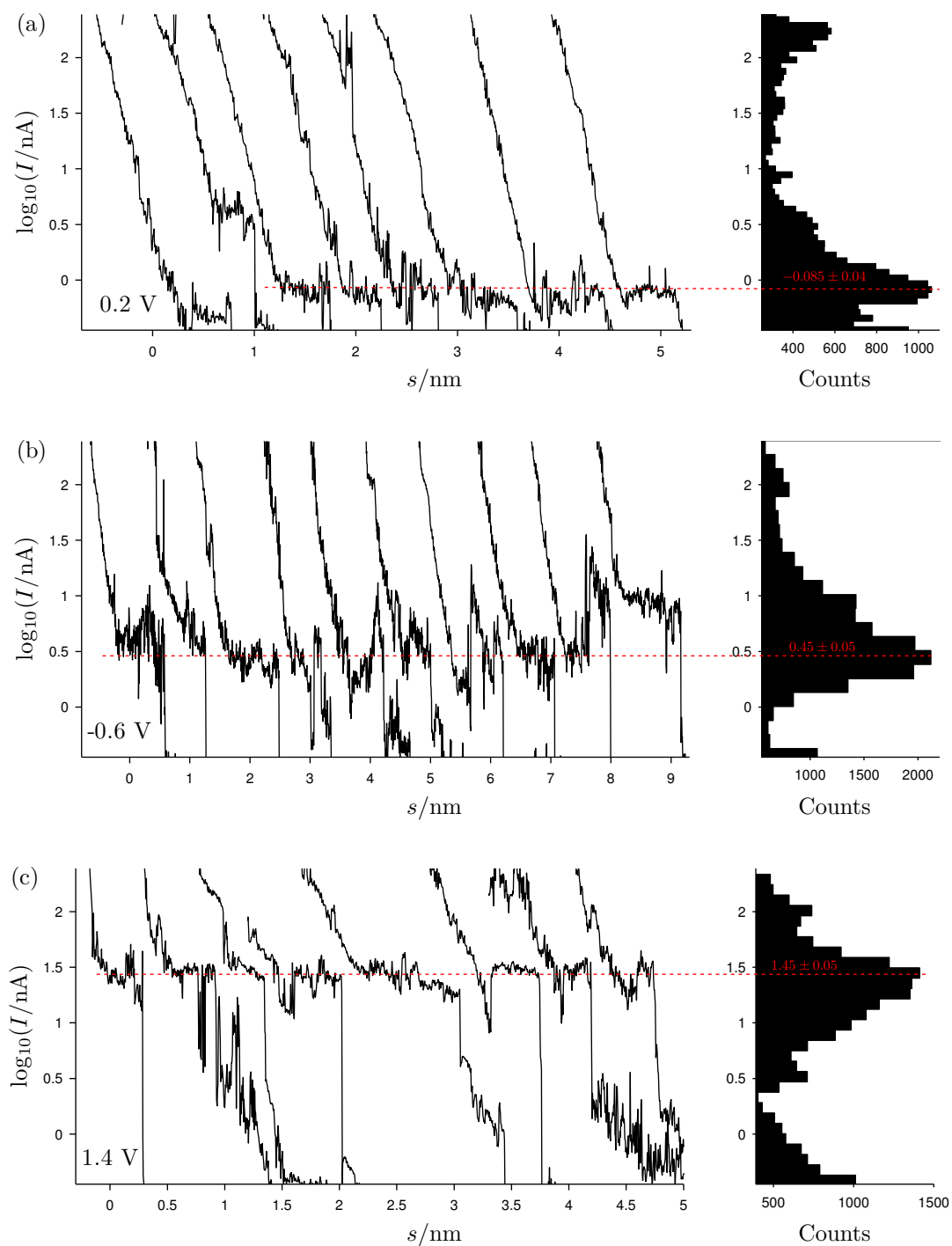


Figure 5.4: Representative $I(s)$ traces and filtered histograms for 4[T3]4, taken at tip biases of a) 0.2 V (82 traces), b) -0.6 V (67 traces), and c) 1.4 V (67 traces), on the high (0 – 333 nA) adapter. Setpoint: 500 pA, approach: 1.0 nm.

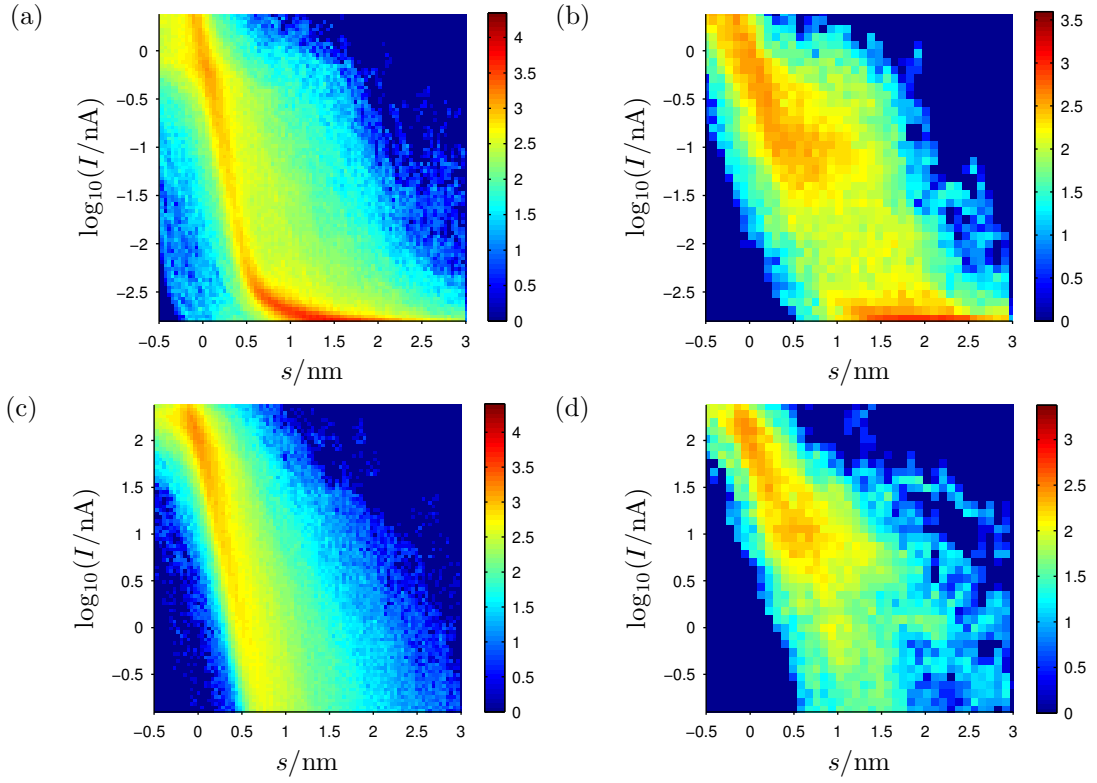


Figure 5.5: Area density plots for $I(s)$ traces measured on the low current amplifier a) before (5000 traces) and b) after filtering for current plateaus (181 traces). Figures c) and d) are the same as a) and b), respectively, (5000 and 100 traces) but the data set was acquired on the high current amplifier. Both sets were acquired with a tip bias of +1.0 V. The values on the colour bar are the logarithms (base 10) of the bin counts.

shown for ADTs in Chapter 4 (Figure 4.5), reflecting the relative noise levels on the measurements of the two species.

The $I(s)$ -derived $I(V)$ characteristics of both reproducible conductance groups are presented in Figure 5.6. Given that both conductance groups are temperature-independent over the range 295–390 K, it should be concluded that the dominant transport mechanism under these conditions is tunnelling. Therefore, the $I(V)$ characteristics of the low conductance group (Figure 5.6a) were fitted by consideration of the quantum mechanical transmission through the indented barrier described in Figure 5.2; with $\phi_1 = \phi_3 = 2.0$ eV (above $E_F = 5.5$ eV) and a total

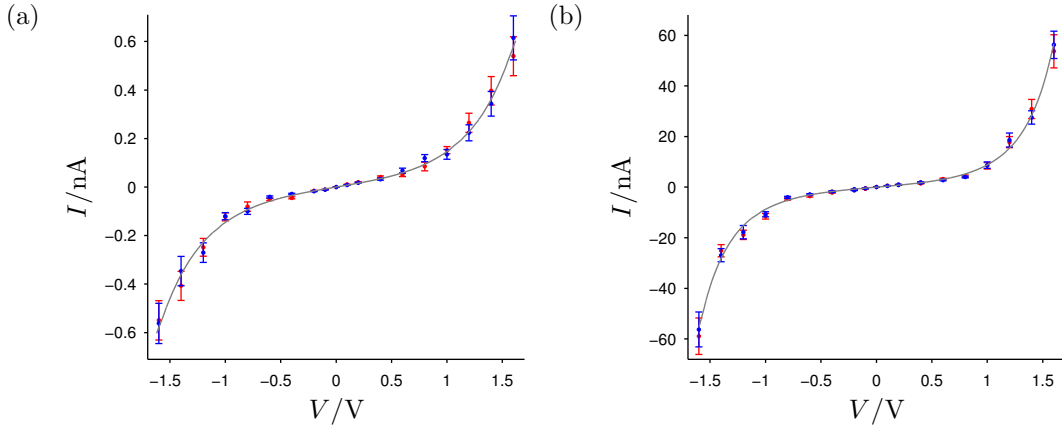


Figure 5.6: The $I(V)$ characteristics of the two repeatable conductance groups for 4[T3]4; a) low and b) high. Each data point corresponds to a peak position on an $I(s)$ histogram, with the error bars relating to the width of the central bins. The blue and red data points were measured at 295 K and 390 K, respectively. For the high group, the data measured on both low and high current amplifiers have been included. The lines of fit were generated by computation of the quantum mechanical transmission through tunnel barriers and subsequent intergration with the Landauer equation (Equation 2.13); the parameters used for each are discussed in the text.

width of $L = 2.57$ nm (the full molecular length; Section 5.1), the least-squares optimised values for the two free parameters were $m^* = (0.186 \pm 0.003) m_e$ and $\phi_2 = (1.33 \pm 0.02)$ eV. (A temperature of 295 K was used during the integration to derive the current.) In order to achieve a fit for the high group, it was necessary to substantially reduce the width of the barrier. (A reasonable fit could not be obtained simply by altering the effective mass and the central barrier height.) The fit in Figure 5.6b was produced with $\phi_2 = (0.75 \pm 0.03)$ eV and $m^* = (0.281 \pm 0.004) m_e$ after the subtraction of 0.5 nm from the alkanethiol sections on each side of the barrier. (This value was chosen after considering the average break off distance value for the group; Figure 5.7.)

The parameters used for the low group seem sensible if the molecule is near fully-stretched and suggest that the energy level mediating the transport for the thiophene system is located roughly 1.33 eV away from the Fermi level. It should be noted that a similar fit line can be generated by considering a rectangular

tunnel barrier of height 1.70 eV and width 2.57 nm with an effective charge carrier mass of $0.18 m_e$ (parameters optimised by eye). The effective mass value is similar to that determined from the indented barrier fit, and the barrier height is close to the value expected from averaging the heights of each individual section. These findings are not particularly surprising and suggest that a simple Simmons tunnelling model 2.2.1 could be used instead. However, this approach would not reveal as much information about the component energy levels of the system. For the high conductance group, the applicability of the indented barrier shape is questionable and it is unclear what the parameters mean. (These points will be discussed further in Section 5.4.) Again, a similar fit can be generated by employing a rectangular barrier shape of height 1.0 eV, width $L = (2.57 - 1.2)$ nm, and effective mass $0.26 m_e$. The change in parameters in going from the indented to the rectangular barrier is similar to that observed for the low group and again implies that a simple Simmons model could be used instead. In any case, the shape of the $I(V)$ curve requires that the barrier be both far shorter and narrower than that of the low conductance group.

To help address the physical origin of the high group, a tip-sample separation analysis was conducted. Absolute tip-sample distances were calibrated using Equation 3.1. An average decay constant of $\beta = (10.8 \pm 0.3) \text{ nm}^{-1}$ was estimated from featureless $I(s)$ traces acquired using the low and high current amplifiers, according to the method described in Figures 3.5 and 4.11. Figure 5.7 is a two-dimensional histogram of conductance and tip-sample separation distance at the point of molecular break off for 4[T3]4. The figure highlights the distribution in molecular break off distances of the two conduction groups; the low (~ 0.09 nS) and high (~ 5.0 nS) groups span distances of roughly 1.7 – 2.5 nm and 1.1 – 1.7 nm, respectively. Clearly, the average break off distance for the high group is significantly larger than that of the low group. These distances are discussed further in Section 5.4 at the end of this chapter. The data measured at biases of magnitude greater than 0.4 V has not been included in Figure 5.7 as the $I(V)$ characteristics of the groups depart from linearity and the conductance begins to change.

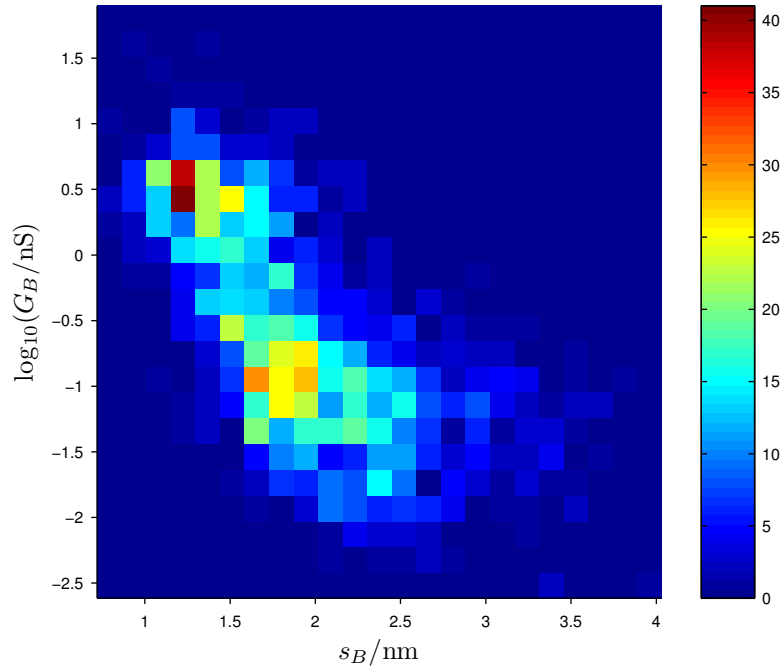


Figure 5.7: Two-dimensional histogram constructed by reading the absolute tip-sample separation distance (s_B) and the conductance (G_B) at the point of molecular (4[T3]4) break off on each $I(s)$ plateau *i.e.* the coordinates at the end of each current plateau. The figure includes 1600 curves, from both current adapters, measured at biases in the linear $I(V)$ regimes ($|V| < 0.6$ V; see Figure 5.6). The values on the colour bar are the counts in each two-dimensional bin.

5.2.2 Alkyl Chain Dependence

In this section, data for the remaining terthiophene molecules (3[T3]3, 5[T3]5, and 6[T3]6) are presented in order to investigate the effect of variation of the alkyl side group length upon the molecular $I(V)$ characteristics. Most of the raw data, including individual $I(s)$ traces and histograms, have been omitted for brevity since the overall character of the results is extremely similar to that presented for 4[T3]4 in Section 5.2.1.

Figure 5.8 shows an example data set measured from 3[T3]3 on the low current amplifier both before and after filtering for current plateaus. Before filtering, the exponential decay backbone resulting from $I(s)$ traces is visible (Figure 5.8a).

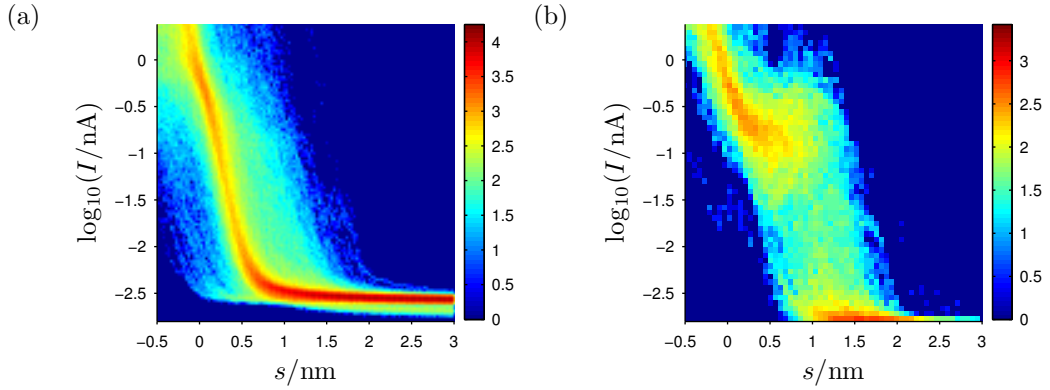


Figure 5.8: Area density plots of $I(s)$ traces for 3[T3]3 measured on the low current amplifier a) before (5000 traces) and b) after filtering for current plateaus (159 traces). Both sets were acquired with a tip bias of +0.2 V. The values on the colour bar are the logarithms (base 10) of the bin counts.

After filtering, a clear molecular signal originating from current plateaus on the traces can be observed around roughly -0.7 on the vertical axis, corresponding to ~ 1 nS. Similar to the data for 4[T3]4 (Section 5.2.1), current plateaus at many different values could be observed at any given bias; however, the conductance group highlighted here produces the largest current peaks in histograms and is the only reproducible group that consistently scales with the applied bias. The $I(V)$ characteristics of this group are mapped in Figure 5.9a; for biases of magnitude greater than 1.2 V, the conductance group could no longer be observed on the low current amplifier and so the data points in these ranges correspond to those measured on the high current amplifier. (Both amplifiers gave equivalent measurements of the group, within experimental error, for biases of ± 1.0 V). Figure 5.9b shows a conductance *versus* break off distance histogram for the group (similar to that described in Figure 5.7).

Again, the group was temperature-independent and hence the line of fit to the $I(V)$ curve (Figure 5.9a) was generated by considering the tunnelling through an indented barrier (Figure 5.2), where $\phi_1 = \phi_3 = 2.0$ eV, $\phi_2 = (1.30 \pm 0.03)$ eV, $L = 2.31$ nm (full molecular length), and $m^* = (0.169 \pm 0.001) m_e$ ($E_F = 5.5$ eV, $T = 295$ K). These parameters are reasonably close to those required to fit the low group measured from 4[T3]4, suggesting the molecules are in a similar config-

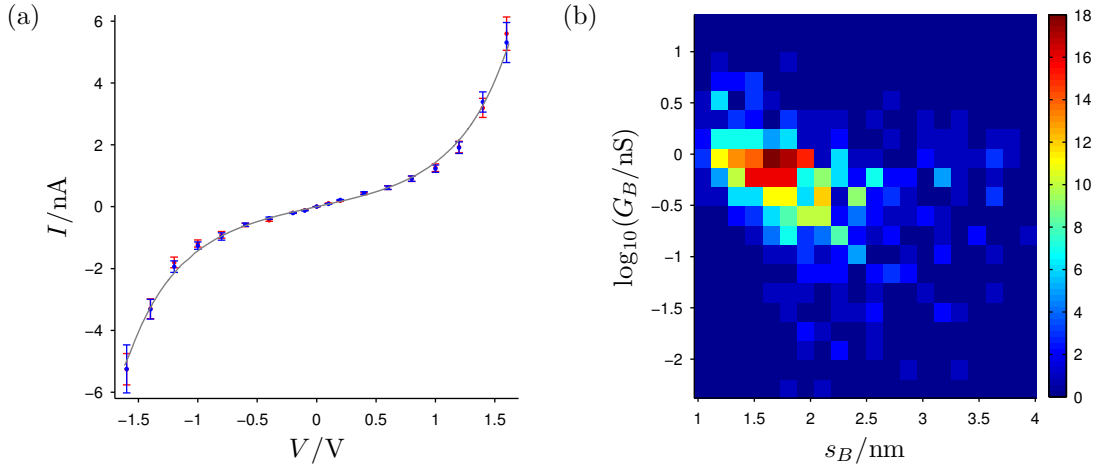


Figure 5.9: a) The $I(V)$ characteristics of the reproducible conductance group for 3[T3]3 measured with the $I(s)$ method at temperatures of 295 K (blue) and 390 K (red). The line of fit was generated by computation of the quantum mechanical transmission through an indented barrier (parameters described in the text) and subsequent integration with the Landauer equation (Equation 2.13). b) Two-dimensional histogram showing conductance (G_B) against absolute tip-sample separation distance (s_B) at the point of molecular break off for the $I(s)$ method. The figure includes the room-temperature data from roughly 500 curves measured in the bias range $|V| \leq 0.8$ V. Distance calibration was performed using Equation 3.1 with an average measured decay constant of $\beta = (11.0 \pm 0.2) \text{ nm}^{-1}$. The values on the colour bar are the counts in each two-dimensional bin.

uration in both cases. Furthermore, Figure 5.9b shows that the majority of the bridges experience break off at distances of roughly 1.3 – 2.2 nm. The extent of this range and its position relative to the length of the molecule are both similar to those observed for the low group of 4[T3]4 in Figure 5.7. A reproducible, bias-scaling conductance group analogous to that of the high group of 4[T3]4 was not observed (on either the low or high current amplifiers); possible reasons for this discrepancy are discussed in Section 5.4.

Figure 5.10 is similar to Figure 5.9 but details processed results for 5[T3]5. Again, only one bias-scaling conductance group could be isolated and the $I(V)$ characteristics are shown in Figure 5.10a. The break off conductance *versus* distance characteristics for the group are shown in Figure 5.10b; the low-bias

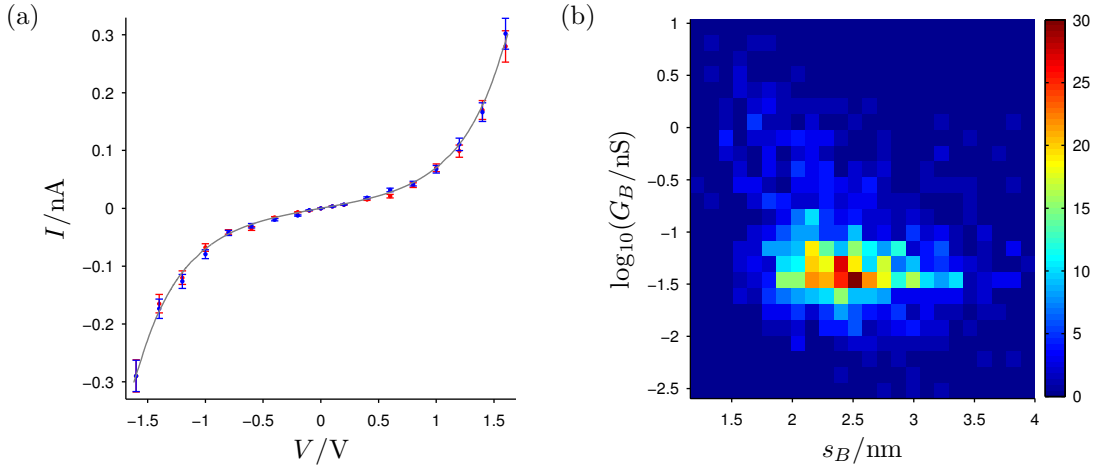


Figure 5.10: a) The $I(V)$ characteristics of the reproducible conductance group measured for 5[T3]5 with the $I(s)$ method at temperatures of 295 K (blue) and 390 K (red). The line of fit was generated by computation of the quantum mechanical transmission through an indented barrier (parameters described in the text) and subsequent integration with the Landauer equation (Equation 2.13). b) Two-dimensional histogram showing conductance (G_B) against absolute tip-sample separation distance (s_B) at the point of molecular break off for the $I(s)$ method (comprising data from 1000 room-temperature curves in the $|V| \leq 0.8$ V regime). Distance calibration was performed using Equation 3.1 with an average measured decay constant of $\beta = (10.8 \pm 0.2) \text{ nm}^{-1}$. The values on the colour bar are the counts in each two-dimensional bin.

conductance is roughly 0.04 nS and the majority of the bridges are destroyed at tip-sample separations between 2.15 – 2.75 nm (compared to a molecular length of $L = 2.82$ nm; Section 5.1). The results were again temperature-independent, within experimental uncertainty, over a range of 295 – 390 K. Hence, the indented tunnel barrier model was applied to the $I(V)$ curve, with $\phi_1 = \phi_3 = 2.0$ eV ($E_F = 5.5$ eV, $T = 295$ K) and $L = 2.82$ nm, yielding best estimates of $m^* = (0.174 \pm 0.002) m_e$ and $\phi_2 = (1.36 \pm 0.02)$ eV.

Figure 5.11a summarises and compares the key $I(V)$ characteristics of the molecules studied in this section, and Figure 5.11b illustrates the low-bias conductance trend with molecular chain length (for variations in alkyl group chain length). The $I(V)$ characteristics for 6[T3]6 could not be convincingly determined from the experimental measurements. Whilst a few current plateaus were

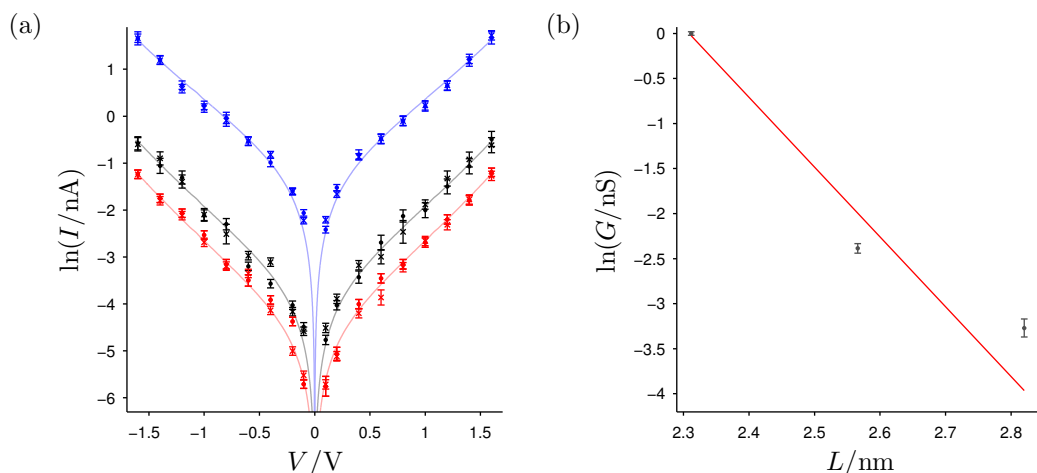


Figure 5.11: a) The $I(V)$ characteristics of 3[T3]3, 4[T3]4 (low group), and 5[T3]5 (highest to lowest) at 295 K (circles) and 390 K (crosses). The fit lines were computed using the indented tunnel barrier model (parameters described in the text). b) The zero-bias conductance of each molecule ($G = I/V$) was estimated from linear fits to the experimental $I(s)$ data points measured for $|V| < 0.6$ V and this is plotted against molecular length on a semi-log plot. The red line is a linear fit to the data, weighted by the error estimates (determined from the linear fits); the gradient implies $\beta = (0.78 \pm 0.15) \text{ \AA}^{-1}$.

observed at any given bias (similar to the observations from the other molecules), a reproducible, bias-scaling conductance group could not be isolated. It is likely that a portion, or majority, of the $I(V)$ curve resides below or too close to the noise threshold of the low current amplifier (0.0015 nA). This potentially means that the entire linear region, used for zero-bias conductance estimates, cannot be measured. This idea is elaborated upon in Section 5.4, and other possibilities for the lack of signal are also discussed. The estimate for the decay constant associated with the alkyl chains, stated in the figure caption, is compared to the value measured for pure ADTs in Chapter 4, in Section 5.4.

5.2.3 Thiophene Unit Dependence

Data for 5[T2]5 and 5[T1]5 are presented in this section in order to investigate the thiophene unit dependence of the molecular $I(V)$ characteristics. (The results for 5[T3]5 are shown in Figure 5.10 and are referenced for comparison.)

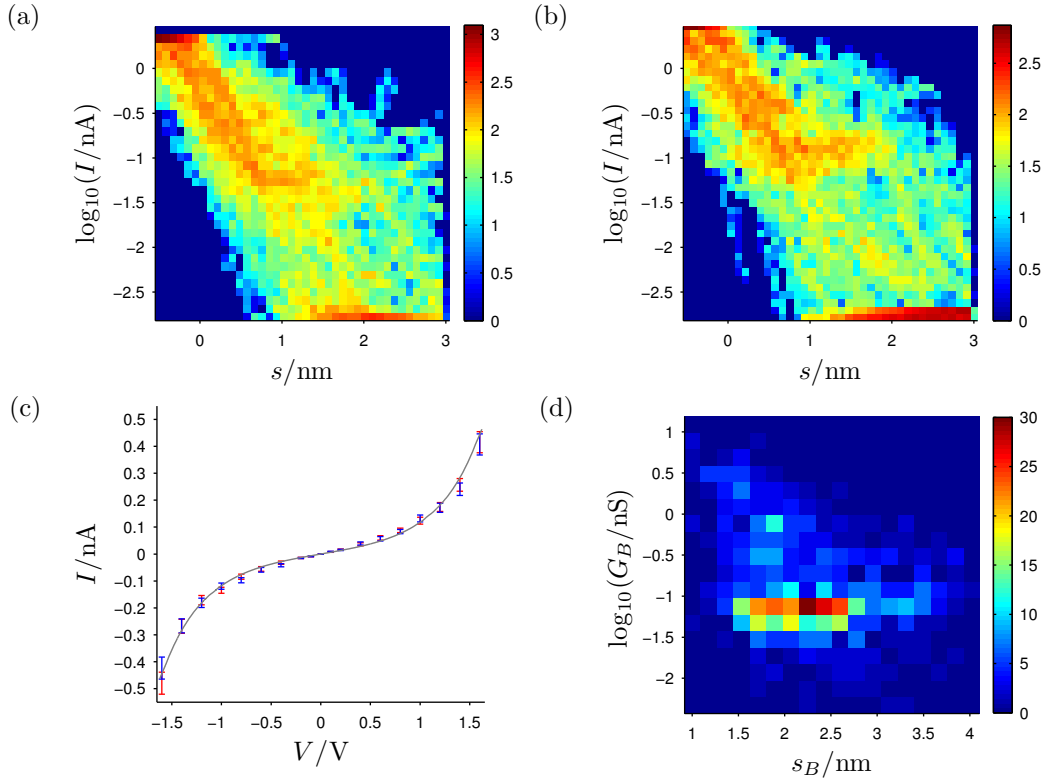


Figure 5.12: Area density plots for $I(s)$ traces from 5[T2]5, measured on the low current amplifier, with applied tip biases of a) $+0.8\text{ V}$ (86 traces) and b) -0.8 V (79 traces). The values on the colour bar are the logarithms (base 10) of the bin counts. c) The $I(V)$ characteristics of the reproducible conductance group determined by the $I(s)$ method at temperatures of 295 K (blue) and 390 K (red). The parameters for the line of fit are described in the text. d) Two-dimensional histogram showing conductance (G_B) versus absolute tip-sample separation distance (s_B) at the point of break off for the $I(s)$ method (comprising roughly 800 room-temperature curves acquired at biases of $|V| \leq 0.8\text{ V}$). Distance calibration was performed using Equation 3.1 with a measured average decay constant of $\beta = (11.0 \pm 0.1)\text{ nm}^{-1}$.

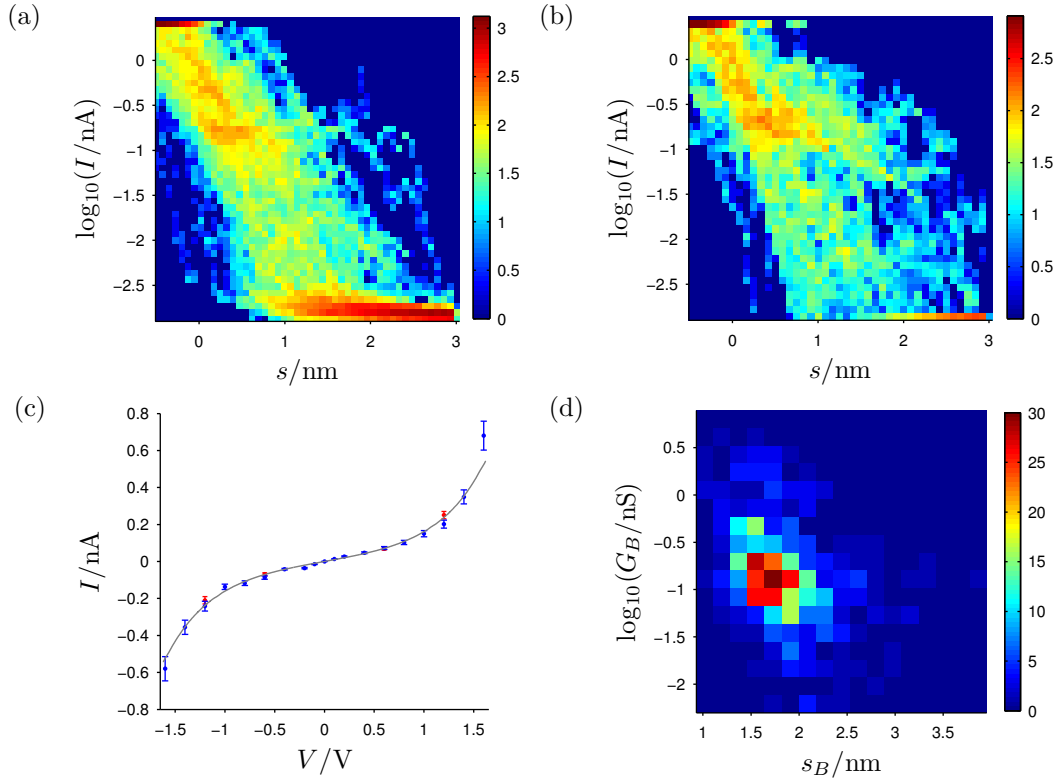


Figure 5.13: Area density plots for $I(s)$ traces from 5[T1]5, measured on the low current amplifier, with applied tip biases of a) +1.2 V (88 traces) and b) -1.2 V (50 traces). The values on the colour bar are the logarithms (base 10) of the bin counts. c) The $I(V)$ characteristics of the reproducible conductance group determined by the $I(s)$ method at temperatures of 295 K (blue) and 390 K (red). (Elevated temperature measurements were only performed at biases of ± 0.6 V and ± 1.2 V.) The parameters for the line of fit are described in the text. d) Two-dimensional histogram showing G_B versus s_B for the $I(s)$ method (from roughly 600 room-temperature curves taken at biases of $|V| \leq 0.8$ V). Distance calibration was performed using a measured decay constant of $\beta = (10.9 \pm 0.1) \text{ nm}^{-1}$.

5. OLIGOTHIOPHENES

Figure 5.12 summarises key results for 5[T2]5 along with example data (raw $I(s)$ curves binned into two-dimensional current-distance histograms). The $I(V)$ characteristics of the single reproducible conductance group (~ 0.08 nS, Figure 5.12c) did not demonstrate any dependence with temperature between 295 K and 390 K, and so were fitted using the indented tunnel barrier model with $\phi_1 = \phi_3 = 2.0$ eV ($E_F = 5.5$ eV, $T = 295$ K), $L = 2.47$ nm (full molecular length), $\phi_2 = (1.46 \pm 0.07)$ eV and $m^* = (0.196 \pm 0.003) m_e$. From Figure 5.12d, the majority of the molecular bridges are severed at tip-sample separations in the approximate range 1.6 – 2.5 nm. Figure 5.13 shows a results summary for the only reproducible conductance group (~ 0.12 nS) identified for 5[T1]5; the measurements are again temperature-independent and the parameters yielded from the application of the indented tunnel barrier model to the $I(V)$ curve were $\phi_2 = (1.64 \pm 0.09)$ eV and $m^* = (0.237 \pm 0.005) m_e$ (with the width set to the full molecular length, $L = 2.12$ nm).

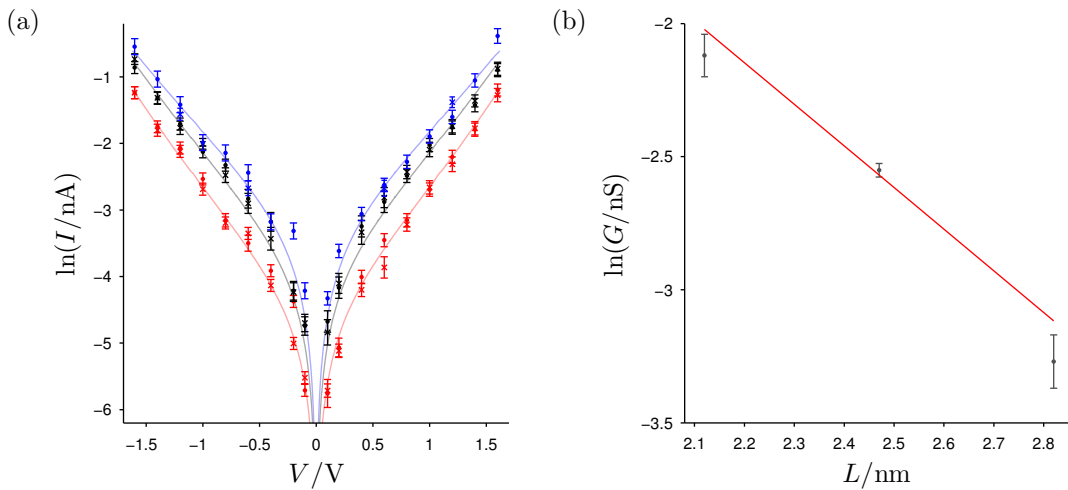


Figure 5.14: a) The $I(V)$ characteristics for 5[T1]5, 5[T2]5, and 5[T3]5 (highest to lowest) at 295 K (circles) and 390 K (crosses). The fit lines were computed using the indented tunnel barrier model (parameters described in the text). b) The zero-bias conductance of each molecule ($G = I/V$) was estimated from linear fits to the experimental $I(s)$ data points measured for $|V| < 0.6$ V and this is plotted against molecular length on a semi-log plot. The red line is a linear fit to the data, weighted by the error estimates (determined from the linear fits); the gradient implies $\beta = (0.16 \pm 0.04) \text{ \AA}^{-1}$.

Figure 5.14 is analogous to Figure 5.11, summarising all the $I(V)$ characteristics for the molecules measured in this section and illustrating the conductance *versus* thiophene unit trend. A thorough interpretation and discussion is provided in Section 5.4.

5.2.4 Summary

Table 5.1 summarises the key results for the oligothiophene molecules measured by the $I(s)$ method, as well as the parameters required to fit the $I(V)$ curves with the indented tunnel barrier model. Only information relating to the low conductance group of 4[T3]4 has been included in the table because, as suggested in Section 5.2.1, the application of the indented barrier model to the high conductance group is likely inappropriate. These results are compared and contrasted both with each other and with literature values in Section 5.4.

Table 5.1: Summary of the zero-bias conductance and break off distance values for each oligothiophene molecule, along with the parameters required to fit the measured $I(V)$ curves using the indented tunnel barrier model.

Mol.	L/nm	s_B/nm	G/nS	m^*/m_e	ϕ_2/eV
3[T3]3	2.31	1.75 ± 0.45	1.00 ± 0.02	0.169 ± 0.001	1.30 ± 0.03
4[T3]4	2.57	2.10 ± 0.40	0.092 ± 0.005	0.186 ± 0.003	1.33 ± 0.02
5[T3]5	2.82	2.45 ± 0.35	0.038 ± 0.004	0.174 ± 0.002	1.36 ± 0.02
5[T2]5	2.47	2.05 ± 0.45	0.078 ± 0.002	0.196 ± 0.003	1.46 ± 0.07
5[T1]5	2.12	1.75 ± 0.35	0.12 ± 0.01	0.237 ± 0.005	1.64 ± 0.09

5.3 $I(V, s)$ Measurements

Figures 5.15a and 5.15b show example $I(V, s)$ measurements for 5[T2]5. In Figure 5.15a, the curves first converge to a high conduction group (~ 0.5 nS at zero bias) and subsequently follow a lower conduction group after an abrupt transition during a single $I(V)$ sweep. The characteristics of the low group closely match

those of the only group isolated from $I(s)$ measurements (albeit deviating slightly at very low biases). Also, the tip-sample separation at which molecular break off occurs, $s_0 = (2.05 \pm 0.05)$ nm, lies in the middle of the range of values measured by the $I(s)$ method (Figure 5.12d). The high group, not identified from $I(s)$ measurements, was fitted using a simple rectangular tunnel barrier model with $\phi = 1.5$ eV, $L = 1.65$ nm, and $m^* = 0.20 m_e$. Possible explanations for the origin of this group and its lack of observation during $I(s)$ measurements are discussed in Section 5.4. In Figure 5.15b all of the $I(V)$ curves in the set adhere closely to the curve modelled from $I(s)$ data, despite the tip-sample separation exceeding the full length of the molecule; this may have arisen from distortion of the tip or substrate during retraction *e.g.* formation of gold atomic chains. Figure 5.16 shows $I(V, s)$ examples for 4[T3]4 in which the curve sets converge toward the low conduction group measured during the $I(s)$ method. There are also convincing $I(V, s)$ results for the other molecules of the species that give good agreement with the theoretical fits suggested from the respective $I(s)$ data. Further interpretation and discussion of these results is given in Section 5.4.

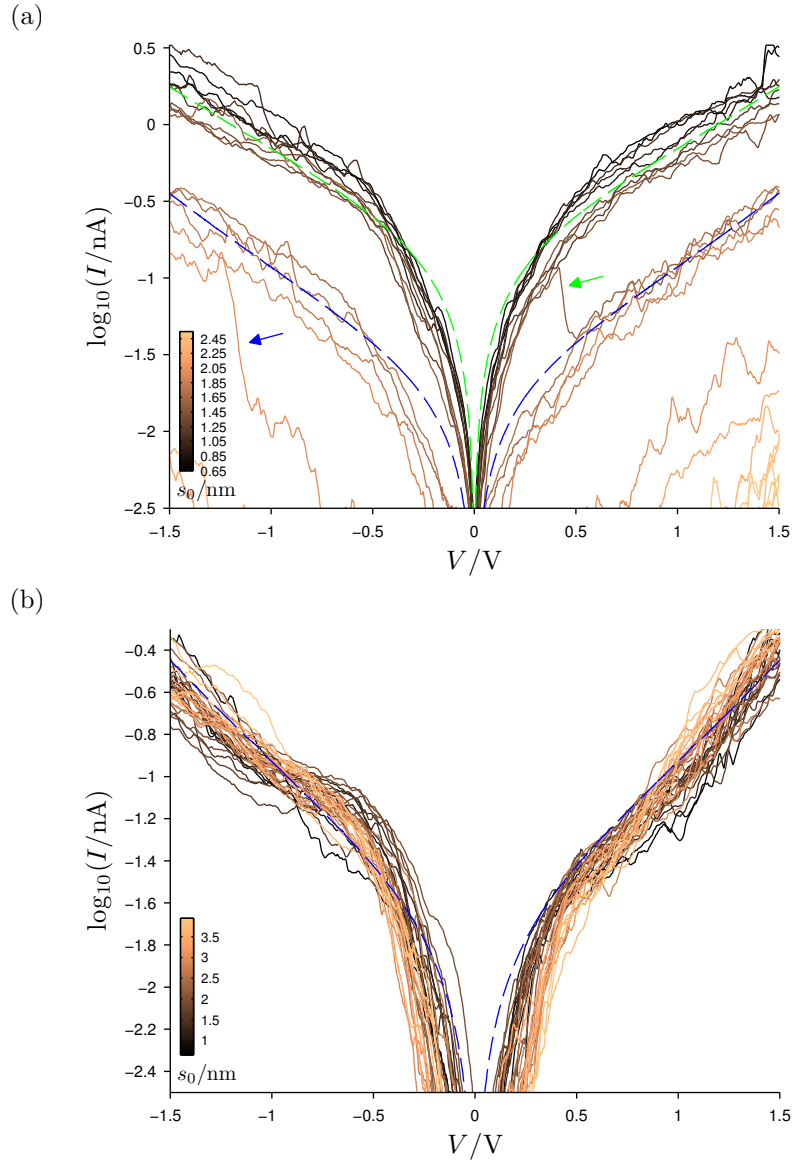


Figure 5.15: Two $I(V, s)$ measurements performed on 5[T2]5; the tip approached the surface by 0.5 nm from a setpoint of -1.5 V and 0.5 nA before being retracted in 0.1 nm steps. The $I(V)$ curves shown are the forward traces from -1.5 to $+1.5$ V at each step. Distance scales were calibrated using Equation 3.1 with $\beta = 11.0 \text{ nm}^{-1}$. In both cases, the blue dashed line is the theoretical $I(V)$ curve for the conductance group identified by the $I(s)$ method (Figure 5.12c). In a) the curves first converge to a high conductance group, fitted with a green dashed line (parameters are in the text). A spontaneous transition (green arrow) to the blue conduction group occurs during the $I(V)$ curve measured at $s_0 = (1.55 \pm 0.05)$ nm, before break off occurs at $s_0 = (2.05 \pm 0.05)$ nm (blue arrow). Interestingly, all the curves in b) are close to the blue dashed line.

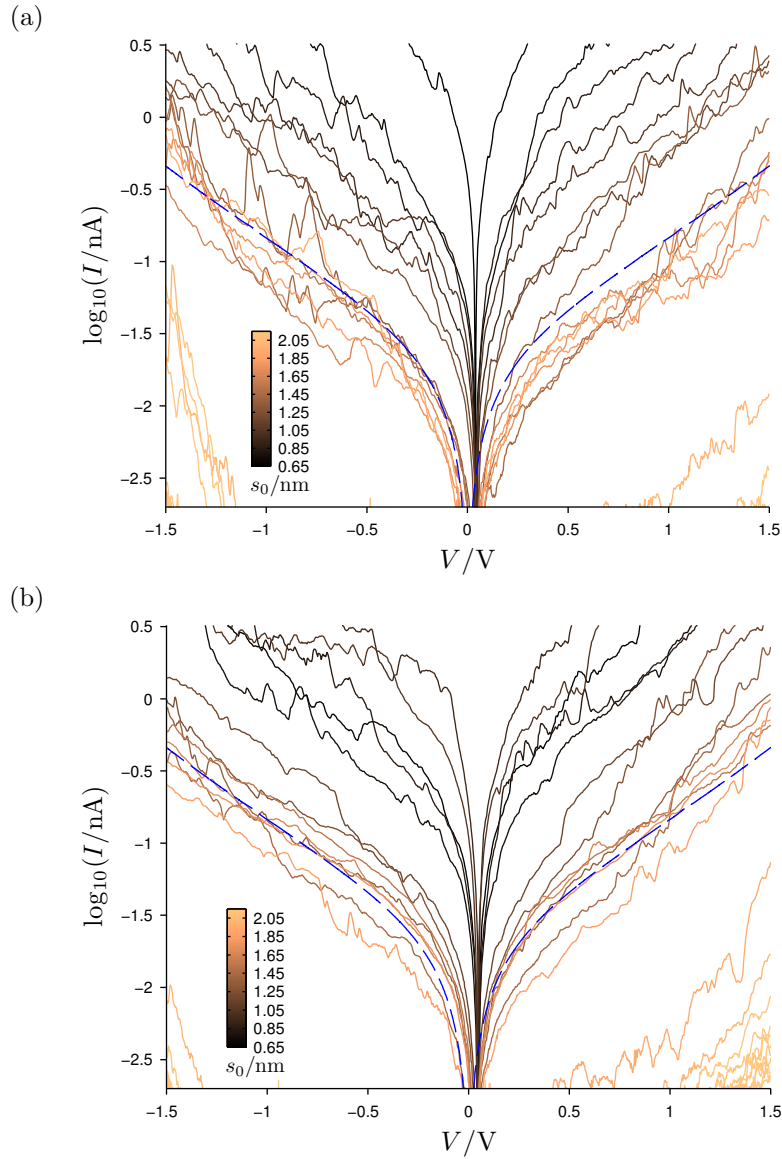


Figure 5.16: Two $I(V, s)$ measurements performed on 4[T3]4; the tip approached the surface by 0.5 nm from a setpoint of -1.5 V and 0.5 nA before being retracted in 0.1 nm steps. The $I(V)$ curves shown are the forward traces from -1.5 to $+1.5$ V at each step. Distance scales were calibrated using Equation 3.1 with $\beta = 10.8 \text{ nm}^{-1}$. In each case, the curves converge toward the blue dashed line, which is the theoretical $I(V)$ curve for the lowest conductance group identified by the $I(s)$ method (Figure 5.6a). Molecular break off occurs between consecutive traces at gap values of a) $s_0 = (2.00 \pm 0.05) \text{ nm}$ and b) $s_0 = (1.90 \pm 0.05) \text{ nm}$; these values lie within the range of values determined by $I(s)$ measurements (Figure 5.7).

5.4 Discussion

For 3[T3]3, 5[T3]5, 5[T2]5 and 5[T1]5, a single temperature-independent (295 – 390 K) conduction group was measured with the $I(s)$ method. (The $I(s)$ method is expected to rule out any possible temperature dependence originating from conformational flexibility by stretching the molecules [34]). The derived $I(V)$ characteristics for these groups could be fitted using the indented tunnel barrier model with seemingly reasonable parameters (Table 5.1), after assuming barrier widths that correspond to the full molecular lengths. (The tip-sample separation analyses indicate that break off typically occurs at distances within 0.7 nm lower than the full molecular lengths.) Multiple groups arising from different contact geometries [60, 102], analogous to those observed for ADTs in Chapter 4, could not be conclusively identified (Figure 4.2). However, given the relative observation probabilities of the different conductance groups witnessed for the ADT species, the groups measured here likely correspond to B group contact geometry.

For 4[T3]4, two conduction groups were measured, the lowest (~ 0.09 nS) of which seems to be consistent with the reproducible groups for the other molecules (likely arising from a near fully-stretched conformer), whereas the second group has a zero-bias conductance roughly fifty times larger (~ 5 nS) and a spread of break off distances (1.1 – 1.7 nm) much shorter than the full molecular length (2.57 nm). The large differences in the conductance values and break off distances between the two groups likely preclude an explanation based solely on contact geometry; for comparison, the C group for ADTs is typically only five times larger than the B group and only twenty times larger than the A group. A more plausible explanation for the origin of the high group is measurement of the molecule between a thiol end group and one of the thiophene rings, instead of between both thiol end groups. Arroyo *et al.* have indeed demonstrated that it is possible to establish good electrical contacts between gold electrodes and thienyl groups by measuring benzene molecules with thiophene anchoring groups using an STM BJ method [126]. If this situation is true, then modelling the $I(V)$ characteristics (Figure 5.6b) with an indented tunnel barrier shape is clearly inappropriate. Modelling was also attempted with a step-shape barrier,

but this involved the use of more free parameters, more unjustified assumptions, and produced a fit no better than that from a simple rectangular barrier model ($\phi = 1.0$ eV, $L = 1.37$ nm, $m^* = 0.26 m_e$). The validity of the hypothesis proposed here could possibly be investigated by performing measurements on asymmetric molecules such as 4[T3] or 4[T1] and comparing the $I(V)$ characteristics to those of the high group. However, the research group at the University of Liverpool report (private communication) that meaningful data could not be obtained for 6[T3] [52]. Further confusion is added by the lack of observation of high groups from the other molecules. It might be possible that the quality of the sample or the vacuum were somehow better during these measurements than they were during measurements for the other molecules, allowing for the measurement of a more difficult to observe group. The SMC value of the 4[T3]4 low group is somewhat lower than the line of fit in Figure 5.11 and a slightly higher effective mass is required to fit the $I(V)$ characteristics; given the hydration state dependence mentioned in Section 5.1, this might indicate a sample or vacuum with less contamination. (However, there was no difference in the sample preparation procedure and no noticeable difference in the chamber pressure at the time).

Convincing measurements could not be obtained for 6[T3]6 as it is suspected that a significant portion of the $I(V)$ curve lies beneath the noise threshold of the low current amplifier. Extrapolation of the line of fit in Figure 5.11, describing the variation of conductance with alkyl chain length, suggests a zero-bias conductance for this molecule between 0.001 and 0.008 nS. Thus, potentially, the curve may not be measurable in the bias regions $|V| < 1.5$ V (given that the low amplifier noise level is 0.0015 nA), making the group incredibly difficult to isolate in a convincing manner. For comparison, Leary *et al.* report a value of (0.012 ± 0.006) nS for the same molecule measured under dry argon gas [104]. More recent experiments by the University of Liverpool research group [52] suggest values of roughly 0.01 nS under dry argon gas and 0.19 nS under air for the same molecule. As anticipated, these values are slightly larger than the value range estimated here for UHV conditions.

In general, the plateaus were far more noisy than those measured from ADTs

(and became worse at higher biases), and this is reflected in the relative quality of the various area density plots of $I(s)$ data sets as well as the two-dimensional break off distance plots; for example, Figure 4.5 for HDT is far more clear than Figure 5.5 for 4[T3]4. Low temperature measurements were attempted for 4[T3]4 and 3[T3]3 but were inconclusive due to excessive noise; therefore, such measurements for the other molecules were not attempted. As mentioned in Chapter 4, low temperature measurements involved coupling a clamping block and copper braid to the sample stage, which likely made the tip-sample interaction even worse by introducing mechanical vibrations. A reasonably large temperature range could still be investigated by heating. Furthermore, imaging of sufficient quality for these samples was not possible, even with tungsten tips. The reason for the relatively poor quality current signal (compared to that from ADTs) is not known. There were often a large range of plateaus for each molecule, corresponding to conductance values other than those of the reproducible groups. However, these were not reproducible and did not produce convincing histogram peaks that scaled with applied bias. Hence, very little meaningful information can be extracted from such data. It is possible that many of these other plateaus can be explained either by integer multiples of the reproducible groups, by different contact geometries, or by different molecular conformations. Given the increased length and structural complexity of the molecules compared to ADTs, far more molecular conformations should be anticipated.

For the terthiophene molecules (N [T3] N), the β factor corresponding to variations in the length of the alkanethiol chains was measured to be $(0.78 \pm 0.15) \text{ \AA}^{-1}$ (Figure 5.11); this is in agreement with the value of $(0.80 \pm 0.01) \text{ \AA}^{-1}$ measured for pure ADTs in Chapter 4, albeit, within a large experimental uncertainty. It is interesting to extrapolate the linear fit from Figure 5.11 to give crude estimates of $(70 \pm 50) \text{ nS}$ and $(700 \pm 600) \text{ nS}$ for 1[T3]1 and 0[T3]0 (terthiophene with thiol anchoring groups), respectively. Clearly, there are problems with this approach. The initial linear fit is based upon only three data points, so the fit parameters have large associated uncertainties. Moreover, it may not be appropriate to extrapolate the fit back this far (from lengths of roughly 2.3 to 1.5 nm) if the transport properties of the molecules change abruptly at very short alkyl chains.

Zhang *et al.* and Bingqian *et al.* both report a value of roughly 2 nS for 1[T3]1 measured under humid conditions [105, 112], whereas Tang *et al.* report a value of approximately 6 nS from theoretical modelling [108]. The disagreement between these literature values and the value reported here likely stems from problems with the extrapolation, but may also result from the measurement of different conduction groups that arise from either different contact geometry, molecular conformation, or both. The issue is further complicated by humidity variation between different experiments. For 0[T3]0, Zhou *et al.* arrive at a conductance of 10,000 nS from theoretical simulations, whereas Taniguchi *et al.* measure 100 nS using a nanoparticle assembly [107, 117]. The estimated value reported in this thesis resides between these two values, but is significantly closer to the latter experimental value.

The measured β factor associated with the thiophene units is $(0.16 \pm 0.04) \text{ \AA}^{-1}$ (Figure 5.14), which is significantly smaller than that for the alkyl chains. This value falls within the range of values measured experimentally under dry conditions and calculated theoretically; 0.1 to 0.2 \AA^{-1} [104, 106, 114, 115]. The addition of thiophene units is less detrimental to the overall conductance than the addition of the equivalent length of alkyl chains. Extrapolation of the linear fit in Figure 5.14 yields a conductance value of $(0.27 \pm 0.14) \text{ nS}$ for 5[T0]5 *i.e.* 1,10-decanedithiol (DDT). In Chapter 4, the conductance values of the A, B, and C groups for DDT were measured to be (0.20 ± 0.01) , (0.74 ± 0.01) and $(1.96 \pm 0.03) \text{ nS}$, respectively. The extrapolated value matches most closely that of the A group, despite the expectation (from Chapter 4) that it match the B group value. For reasons discussed in the previous paragraph, this kind of extrapolation is not definitive and ideally the trend needs to be refined by measurement of further molecules. The A and B groups for DDT are relatively similar in magnitude when compared to the potential scope of the systematic error in the extrapolation; thus, the conduction group identified from the 5[T n]5 molecules could realistically correspond to either of contact geometry. (The very broad range of values in the tip-sample break off distance histograms makes identification of contact geometry extremely difficult for these molecules). Nevertheless, the fact that the extrapolated value is reasonably close to both groups is encour-

aging and goes some way toward verifying the validity of the measurements.

The zero-bias conductance values measured for the low group of each molecule are listed in Table 5.1, along with the key parameters required to fit the derived $I(V)$ characteristics using the indented tunnel barrier model. (The conductance values are in close agreement with recent measurements performed by [52] under a dry argon gas environment.) In general, this barrier model was able to generate very close fits to the experimental $I(V)$ curves for seemingly reasonable parameters. For the terthiophene molecules, the model implies that the energy level mediating charge transport through the conjugated system is roughly 1.33 eV away from the Fermi level; the literature suggests that this is the HOMO, due its relative proximity to the Fermi level compared to the LUMO [104–108]. The barrier value can be doubled to yield a crude estimate of the HOMO-LUMO gap size for the ring system; 2.66 eV. This value lies between the values of 2.15 eV for 6[T3]6 and 3.4 eV for 1[T3]1 reported by Leary *et al.* and Bingqian *et al.*, respectively [104, 105]; as stated in Section 5.1, the former estimate is based on DFT calculations and is likely an underestimate of the true gap size. It is possible that there is a slight increase in gap size in going from 3[T3]3 to 5[T3]5 (2.60 eV to 2.72 eV), but the size of the error estimates make such a trend impossible to prove conclusively. However, such an increase might be anticipated because increasing the length of the alkyl chains on either side of the thiophene rings should increase electron confinement in the conjugated system and open the HOMO-LUMO gap slightly wider [17].

The fit parameters for 5[T2]5 and 5[T1]5 suggest larger gap sizes of roughly 2.92 and 3.28 eV, respectively. (Again, these gap values are estimated by simply doubling the barrier height ϕ_2). This general trend is in agreement with that described in Section 2.1; increased conjugation leads to decreased HOMO-LUMO gap sizes [17]. Interestingly, this trend can be observed by the colour change in the molecular powders; bright yellow to pale yellow as the thiophene ring number is decreased. For further comparison, DFT calculations reported in the literature suggest values of 2.0 – 2.3 eV for infinite polythiophene chains [127, 128]. The method of estimation employed in this thesis may be unreliable for numerous

reasons, chiefly because; i) the HOMO is slightly closer to the Fermi level than the LUMO, so doubling the measured barrier yields an underestimate, and ii) the $I(s)$ method involves stretching the molecules, which can lead to increased gap sizes compared to the expected values for relaxed molecules [105]. Nevertheless, the estimates presented here still seem to be consistent with the expected trend and reside within the spread of literature values. Ideally, photoelectron spectroscopy under UHV should be used to verify or refine the estimates reported in this thesis, but this was not possible for technical reasons involving equipment failure.

The effective charge (hole) carrier masses determined from fitting the $I(V)$ curves of terthiophene molecules range between 0.168 and 0.189 m_e ; considerably lower than the values determined for the ADTs ($0.32 \pm 0.02 m_e$). This value seems to increase with decreasing numbers of thiophene units; (0.196 ± 0.003) and (0.237 ± 0.005) m_e for 5[T2]5 and 5[T1]5, respectively. It is unclear what this means, but a possible interpretation is that the measured effective mass is an average of the carrier mass through the alkanethiol components and a much lower carrier mass through the conjugated component. Though, a spatially varying effective mass does not seem compatible with coherent tunnelling. Robust theoretical calculations of the carrier mass for these molecules are desirable.

In general the indented barrier model produced excellent fits to the experimental data and yielded an internally consistent set of parameters, which are in reasonable agreement with external literature values. It should be noted, that for any given data set, it may be possible that there exists more than one optimum set of parameters to which a regression algorithm may converge. This situation was generally not observed even after adjustment of the initial conditions. Furthermore, manual adjustment of the parameters to fit by eye always seemed to suggest parameters very close to those suggested by the automated regression. As implied in Section 5.2.1, similar fit lines could be generated for most of the $I(V)$ curves using a simple rectangular barrier model, with a similar effective carrier mass, but with a height roughly equivalent to the width-weighted average of the heights of the individual sections of the corresponding indented barrier.

However, the rectangular model conceals more information about the component energy levels system and so is not as useful as the indented barrier model. In principle, it may be possible to distinguish the barrier shapes from one another if the experimental $I(V)$ curves had more resolution (voltage steps smaller than 0.2 V), and extended further ($|V| > 1.6$ V), on the voltage axis; if an experimental transmission function was obtained from this curve by reversing the Landauer equation, then ripples in the function at high energies may allude to which barrier shape more accurately describes the system (Section 2.2.2.1). Given the outcome of the fitting in Chapter 4, the effects of the image potential were not considered here. Moreover, additional assumptions (that are difficult to justify) would need to be introduced regarding the modification to the shape of the indented barrier when under the influence of the image force. Consideration was lent to the molecular level model (Section 2.2.2.2) for the purposes of modelling the transport through the thiophene ring system (as suggested in Section 5.1); however, suitable $I(V)$ characteristics could not be derived for any reasonable parameters. Even if this were not the case, it is difficult to see the benefit of such a model over the numerical tunnelling model; effective carrier masses are replaced by coupling strengths, which are equally, if not more, difficult to interpret. The indented barrier model with the numerical tunnelling code is adequate for describing the transport, and is consistent with the work of Chapter 4.

The conduction groups observed by the $I(s)$ method were also observed by the $I(V, s)$ method. Figure 5.15a demonstrates a spontaneous transition from a high group (~ 0.5 nS), which was not observed with the $I(s)$ method, to the low group (0.078 ± 0.002 nS) identified by the $I(s)$ method. The conductance ratio for the transition is similar to those observed for the ADTs in Section 4.4 and can likely be explained in the same manner *i.e.* transition from C to B contact geometries (or less likely, B to A). The reason for the lack of observation of this higher group (not to be confused with the high group from 4[T3]4, which likely stems from a different molecular conformation) with the $I(s)$ method is not known. Nevertheless, the utility of the $I(V, s)$ method is once again demonstrated; potentially only one measurement is required to establish the full $I(V)$ characteristics of multiple and improbable conduction groups and observe transitions between them.

However, the observation of such transitions are indeed rare, and positive results indicating molecular bridge formation with this method are usually more akin to those shown in Figure 5.16; several such results were obtained for the other molecules, which verify the groups identified by the $I(s)$ method.

Finally, recent measurements by the research group of Reference [52] have seemingly corroborated and expanded upon the hydration state dependence reported by Leary *et al.* (Section 5.1.1) [104]. The group report vastly increased molecular conductance when going from a dry argon atmosphere to ambient conditions, and the effect is more pronounced for molecules with more thiophene units; in fact, monothiophene molecules exhibit no detectable conductance change when the environmental conditions are varied. Moreover, in ambient conditions, the molecules exhibit conductance increases with temperature (300 – 373 K); again, this effect is not present for monothiophenes and becomes more pronounced with increasing numbers of thiophene units. All the molecules studied are shorter than the shortest molecule studied by Lee *et al.* [116], so the transport is expected to be far from the thermal hopping regime, and dominated by tunnelling within the stated temperature range. Thus, the proposed explanation for this temperature effect is hydration state. The formation of a solvation shell around the thiophene backbone shifts the LUMO resonance very close to the Fermi level of the electrodes, leading to increased conductance. (At the same time, the HOMO resonance is shifted very far away from the electrode Fermi level). As the thiophene backbone gets longer, the solvation shell comprises more water molecules, enhancing the effect. The temperature dependence then derives solely from the temperature dependence of the Fermi distribution function; if a transmission resonance is closer to the applied bias interval, then the contribution to the current from thermal broadening of the Fermi distributions is more pronounced [129]. The UHV measurements reported in this thesis are temperature-independent, and the values are in excellent agreement with the aforementioned argon atmosphere measurements; thus, they provide support for the proposed theory and will form an integral part of a forthcoming manuscript, which is currently being drafted in collaboration with Reference [52].

5.5 Summary

The $I(s)$ and $I(V, s)$ methods were used to study the $I(V)$ characteristics of $N[\text{T}3]N$ and $5[\text{T}n]5$ oligothiophene molecules, over a temperature range of 295 – 390 K. These UHV measurements were spurred by a recent report suggesting that the presence of water can dramatically and reversibly increase the conductance of the molecules [104]. For each molecule, a temperature-independent reproducible conduction group was measured, which, from tip-sample separation analyses, corresponds to a near fully-extended conformer. The precise contact geometry of these groups could not be determined conclusively, though B group configurations are heavily suspected based on the work of Chapter 4. (In a few instances, other conduction groups were identified, which likely correspond to different molecular conformations or contact geometries). With increasing alkanethiol chain length, the conductance decreases exponentially, with a decay constant of $(0.78 \pm 0.15) \text{ \AA}^{-1}$, in experimental agreement with that measured for ADTs, $(0.80 \pm 0.01) \text{ \AA}^{-1}$. The exponential decay associated with increasing thiophene units is far more shallow; the measured decay constant for which, $(0.16 \pm 0.04) \text{ \AA}^{-1}$, being within the spread of values reported in the literature. An indented tunnel barrier model was utilised to fit the measured $I(V)$ characteristics; with the surrounding barrier heights set to the anticipated value for alkanethiol chains (2 eV), the regression-optimised height of the central barrier for terthiophenes was roughly 1.33 eV. This value is thought to correspond to the distance from the HOMO to the Fermi level, and suggests HOMO-LUMO gap sizes in loose agreement with those of literature values; it increases slightly when the number of thiophene units is decreased, reflecting the increase in gap size that accompanies increased particle confinement. For terthiophenes, the charge carrier mass was determined to be approximately 0.17 to 0.19 m_e , which is decidedly lower than $(0.32 \pm 0.02) m_e$ for ADTs (toward which the values for molecules with fewer thiophene units seem to converge). The $I(V, s)$ method gave excellent agreement with the $I(s)$ method and again demonstrated many advantages over which. The UHV measurements give good agreement with recent measurements performed under dry argon gas, and provide an excellent baseline from which to better understand new and interesting hydration dependent conductance *versus* temperature trends [52].

Chapter 6

Conclusions

The electrical transport properties of single ADT and alkanethiol-terminated oligothiophene molecules have been characterised under UHV, over large temperature ranges. The measurements were realised through two STM point-contact techniques; the well-known $I(s)$ method and the novel $I(V, s)$ method; both of which depend upon stochastic molecular bridge formation between gold tip and substrate, and compel statistical data analysis.

Chapter 4 provides a thorough investigation of the $I(V)$ characteristics of the Au-ADT-Au system under UHV, otherwise absent from the literature. The anomalous reduction of the molecular conductance for small chain lengths, reported by various groups for measurements performed in other environmental conditions, was far less pronounced here; the conductance adheres closely to the anticipated exponential decay with chain length until a small deviation is observed for the shortest molecule. Thus, the most likely explanation for the anomalous effect and its suppression under UHV is hydration of the thiol contacts (or lack of); the presence of water around the thiol contacts adds a constant resistance in series with the molecular resistance, which becomes more dominant for shorter, less resistive, molecules. This effect is clearly extremely important and should be taken into consideration when characterising the transport properties of any molecular system. Three conduction groups were identified, and judging by the tip-sample separation analyses, these are likely explained by, and provide support for, the step edge contact coordination geometry model (Figure 4.2). The

6. CONCLUSIONS

groups were proven to be temperature-independent over larger temperature and molecular chain length ranges than have been previously investigated, lending support for the existing theory that the transport is dominated by off-resonance coherent hole tunnelling. In each case, the transport characteristics were successfully modelled by considering the transmission through rectangular tunnel barriers, the parameters of which being in agreement with reported literature values. Hopefully, these latest measurements will help clarify some points of confusion in the literature and help streamline the future development of new measurement techniques (in which ADTs are likely to continue to play a prominent role). Though the Au-ADT-Au system is now thoroughly studied, there is still much work involving ADTs that should be carried out. For example, characterisation of their transport properties between electrodes of different materials *e.g.* Co-ADT-Co, Au-ADT-Co *etc.* Furthermore, relatively little work has been performed on methylene chains that are terminated by anchoring groups other than thiol groups, and this should be addressed *e.g.* carboxylic acid, pyridine, amine, and other anchoring groups could be more thoroughly investigated.

The $I(V)$ characteristics of $N[T3]N$ and $5[Tn]5$ oligothiophene molecules, as measured under UHV, are reported in Chapter 5. For each molecule, one reproducible temperature-independent conduction group was isolated that is thought to correspond to molecules in near fully-extended conformations, likely with B group contact geometry. When the length of the alkanethiol chains is increased, the conductance exhibits an exponential decay in accordance with that observed for single ADT molecules. The exponential decay corresponding to increases in the length of the thiophene backbone is far more shallow; potentially making the molecules, and those with similar conjugated systems, excellent candidates for efficient nanoscale transport of charge in devices (molecular wires). The physical and electronic structure of the molecules point toward an indented tunnel barrier model for the transport; and such was used to fit the measured $I(V)$ characteristics, with parameters that are in agreement with the expected trends and literature values. The study of these molecules was necessitated by recent reports suggesting that the conductance can be substantially, and reversibly, increased by the introduction of water vapour into the system. Even more recent

6. CONCLUSIONS

measurements by other parties involved in the same collaborative research group also suggest that hydration of the molecules leads to temperature-dependent conductance values (increasing with temperature). Thus, the UHV measurements reported here (otherwise absent from the literature), for which the level of hydration is expected to be extremely low, provide a solid control experiment from which to better understand these effects and how exactly the electron transport is altered in the presence of water. This effect has important implications for molecular electronics and should be taken into account when the transport properties of similar molecular systems are being characterised. Moreover, the prospect of single molecule humidity sensors is very exciting.

There is a lot of work that needs to be carried out on the oligothiophene system in the future. First, atomic resolution imaging of the samples should be attempted under UHV in order to better understand exactly how the molecules distribute themselves on the gold surfaces; this may lead to a better understanding of exactly which molecular conformers and contact geometries are being measured during the spectroscopy. Second, additional molecules of the same species should be investigated; in particular, those molecules with greater numbers of thiophene units ($n > 3$) should be characterised in order to explore whether or not the hydration state dependence, and the hydration state induced temperature dependence, of the conductance persists according to the proposed model. Third, it is necessary to extend the range of temperatures investigated both in humid and dry conditions. With regards to the latter, this could be attempted in UHV by using liquid helium as the cryogen, which is likely to introduce far less mechanical noise to the STM measurements than the constantly-boiling liquid nitrogen used in the experiments reported in this thesis. Fourth, it would be very interesting to understand how, if at all, subtle alterations to the chemical structure of the molecule change the observed conductance trends; in particular, it would be interesting to find out whether the introduction of certain functional groups to the molecules can disrupt the formation of the solvation shells and nullify the observed hydration effects. Finally, UV-Vis photoelectron spectroscopy measurements should be conducted to obtain accurate estimates of the HOMO-LUMO gap sizes; this information would be instructive during an investigation

6. CONCLUSIONS

of the effects of background illumination on molecular conductance. (A system would need to be developed for the UHV chamber in which the wavelength and intensity of incoming light onto the STM sample stage can be varied in a controlled manner.)

The new $I(V, s)$ method has proven to be a powerful alternative to existing STM-based point-contact SMC measurement techniques. The technique allows the full $I(V)$ characteristics of multiple conduction groups to be measured from an individual molecule. Moreover, remarkable spontaneous transitions between the different groups can sometimes be observed. The method may not be appropriate for STM systems with substantial tip drift (in or out of the plane of the sample) due to the decreased retraction speeds, but should definitely be considered if this is not a problem.

The field of molecular electronics, though promising, is still in its infancy; much more work is required, both incremental and innovative, before its full potential can be realised and molecular electronic devices become commonplace.

References

- [1] Csoeregi, E., Quinn, C. P., Schmidtke, D. W., Lindquist, S.-E., Pishko, M. V., Ye, L., Katakis, I., Hubbell, J. A., and Heller, A. (1994) *Analytical Chemistry* **66**(19), 3131–3138.
- [2] Heath, J. R. Label-Free Nanowire and Nanotube Biomolecular Sensors for In-Vitro Diagnosis of Cancer and other Diseases pp. 213–232 Wiley-VCH Verlag GmbH Co. KGaA (2007).
- [3] Song, H., Reed, M. A., and Lee, T. (2011) *Advanced Materials* **23**(14), 1583–1608.
- [4] Heath, J. R. (2009) *Annual Review of Materials Research* **39**(1), 1–23.
- [5] Aviram, A. and Ratner, M. A. (1974) *Chemical Physics Letters* **29**(2), 277 – 283.
- [6] Ashwell, G. J., Urasinska, B., and Tyrrell, W. D. (2006) *Phys. Chem. Chem. Phys.* **8**, 3314–3319.
- [7] Song, H., Kim, Y., and Jeong, H. (2009) *Nature* **462**(7276), 1039–1043.
- [8] Park, J., Pasupathy, A. N., and Goldsmith, J. I. (2002) *Nature* **417**(6890), 722–725.
- [9] Park, H., Park, J., and Lim, A. K. L. (2000) *Nature* **407**(6800), 57–60.
- [10] Steuerman, D. W., Tseng, H.-R., Peters, A. J., Flood, A. H., Jeppesen, J. O., Nielsen, K. A., Stoddart, J. F., and Heath, J. R. (2004) *Angewandte Chemie* **116**(47), 6648–6653.

REFERENCES

- [11] Blum, A. S., Kushmerick, J. G., and Long, D. P. (2005) *Nat Mater* **4(2)**, 167–172.
- [12] Liljeroth, P., Repp, J., and Meyer, G. (2007) *Science* **31(5842)**, 1203–1206.
- [13] Collier, C. P., Wong, E. W., and Belohradsky, M. (1999) *Science* **285(5426)**, 391–394.
- [14] Quek, S. Y., Kamenetska, M., and Steigerwald, M. L. (2009) *Nat Nano* **4(4)**, 230–234.
- [15] Lörtscher, E., Ciszek, J. W., Tour, J., and Riel, H. (2006) *Small* **2(8-9)**, 973–977.
- [16] Hucknall, D. J. and Morris, A. (2003) *Vacuum Technology: Calculations in Chemistry*, Royal Society of Chemistry, first edition.
- [17] Atkins, P. W. and Friedman, R. S. (2010) *Molecular Quantum Mechanics*, Oxford University Press, USA, fifth edition.
- [18] Autschbach, J. (2007) *Nat Nano* **84(11)**, 1840–1845.
- [19] An, Y.-P., Yang, Z., and Ratner, M. A. (2011) *J. Chem. Phys* **135(4)**, 044706.
- [20] Simmons, J. G. (1963) *Journal of Applied Physics* **34(6)**, 1793–1803.
- [21] Simmons, J. G. (1964) *Journal of Applied Physics* **35(9)**, 2655–2658.
- [22] Datta, S. (1995) *Electronic Transport in Mesoscopic Systems*, Cambridge University Press, first edition.
- [23] Büttiker, M., Imry, Y., Landauer, R., and Pinhas, S. (1985) *Phys. Rev. B* **31**, 6207–6215.
- [24] Landauer, R. (1992) *Physica Scripta* **1992(T42)**, 110.
- [25] Haiss, W., Martín, S., and Scullion, L. E. (2009) *Phys. Chem. Chem. Phys.* **11(46)**, 10831.

REFERENCES

- [26] Miskovsky, N., Cutler, P., Feuchtwang, T., and Lucas, A. (1982) *Applied Physics A* **27**, 139–147.
- [27] Akkerman, H., Naber, R., and Jongbloed, B. (2007) *Proc. Natl. Acad. Sci. USA* **104(27)**, 11161–11166.
- [28] Innes, R. A. and Sambles, J. R. (1987) *Journal of Physics F: Metal Physics* **17(1)**, 277.
- [29] Wold, D. J. and Frisbie, C. D. (2001) *Journal of the American Chemical Society* **123(23)**, 5549–5556.
- [30] Holmlin, R. E., Haag, R., Chabinye, M. L., Ismagilov, R. F., Cohen, A. E., Terfort, A., Rampi, M. A., and Whitesides, G. M. (2001) *Journal of the American Chemical Society* **123(21)**, 5075–5085.
- [31] Abu-Hilu, M. and Peskin, U. (2004) *Chemical Physics* **296(2-3)**, 231–241.
- [32] Newton, M. D. (2003) *Theoretical Chemistry Accounts* **110**, 307–321.
- [33] McCreery, R. L. (2004) *Chemistry of Materials* **16(23)**, 4477–4496.
- [34] Martín, S., Giustiniano, F., Haiss, W., Higgins, S. J., Whitby, R. J., and Nichols, R. J. (2009) *Journal of Physical Chemistry C* **113(43)**, 18884–18890.
- [35] Xiao, Xu, and Tao, N. J. (2004) *Nano Letters* **4(2)**, 267–271.
- [36] Liboff, R. L. (2002) *Introductory Quantum Mechanics*, Addison Wesley, fourth edition.
- [37] Kalotas, T. M. and Lee, A. R. (1991) *American Journal of Physics* **59(1)**, 48–52.
- [38] Rangel, T., Kecik, D., Trevisanutto, P. E., Rignanese, G.-M., Van Swygenhoven, H., and Olevano, V. (2012) *Phys. Rev. B* **86**, 125125.
- [39] Datta, S. (2004) *Nanotechnology* **15(7)**, S433.

REFERENCES

- [40] Omicron NanoTechnology GmbH <http://www.omicron.de/> Accessed: 02/01/2013.
- [41] Department of Physics & Astronomy, Cardiff University <http://www.astro.cardiff.ac.uk/> Accessed: 02/01/2013.
- [42] Woodruff, D. P. and Delchar, T. A. (1994) *Modern Techniques in Surface Science*, Cambridge University Press, second edition.
- [43] PHASIS, Switzerland <http://www.phasis.ch/> Accessed: 02/01/2013.
- [44] Omicron (2005) ISE 10 Sputter Ion Source User's Guide, Omicron NanoTechnology GmbH, .
- [45] Ren, B., Picardi, G., and Pettinger, B. (2004) *Review of Scientific Instruments* **75(4)**, 837–841.
- [46] Bai, C. (2010) *Scanning Tunneling Microscopy and Its Application*, Springer, second edition.
- [47] Love, J. C., Estroff, L. A., Kriebel, J. K., Nuzzo, R. G., and Whitesides, G. M. (2005) *Chemical Reviews* **105(4)**, 1103–1170.
- [48] Haiss, W., vanZalinge, H., Higgins, S. J., Bethell, D., Höbenreich, H., Schiffrin, D. J., and Nichols, R. J. (2003) *Journal of the American Chemical Society* **125(50)**, 15294–15295.
- [49] Song, H., Kim, Y., Jeong, H., Reed, M. A., and Lee, T. (2010) *The Journal of Physical Chemistry C* **114(48)**, 20431–20435.
- [50] Nichols, R. J., Haiss, W., Higgins, S. J., Leary, E., Martín, S., and Bethell, D. (2010) *Phys. Chem. Chem. Phys.* **12**, 2801–2815.
- [51] Chen, F., Li, X., Hihath, J., Huang, Z., and Tao, N. (2006) *Journal of the American Chemical Society* **128(49)**, 15874–15881.
- [52] Prof. Richard Nichols and Prof. Simon Higgins, University of Liverpool <http://pcwww.liv.ac.uk/~nichols/> Accessed: 03/01/2013.

REFERENCES

- [53] Gottlieb, A. D. and Wesoloski, L. (2006) *Nanotechnology* **17(8)**, R57.
- [54] Bardeen, J. (1961) *Phys. Rev. Lett.* **6**, 57–59.
- [55] Tersoff, J. and Hamann, D. R. (1985) *Phys. Rev. B* **31**, 805–813.
- [56] Bohm, D. (1989) *Quantum Theory*, Dover Publications, first edition.
- [57] Kowalczyk, P., Kozłowski, W., Klusek, Z., Olejniczak, W., and Datta, P. (2007) *Applied Surface Science* **253(10)**, 4715–4720.
- [58] Grillo, F., Früchtl, H., Francis, S. M., and Richardson, N. V. (2011) *New Journal of Physics* **13(1)**, 013044.
- [59] Xu, B. and Tao, N. J. (2003) *Science* **301(5637)**, 1221–1223.
- [60] Haiss, W., Martín, S., Leary, E., Zalinger, H. v., Higgins, S. J., Bouffier, L., and Nichols, R. J. (2009) *The Journal of Physical Chemistry C* **113(14)**, 5823–5833.
- [61] Li, C., Pobelov, I., Wandlowski, T., Bagrets, A., Arnold, A., and Evers, F. (2008) *Journal of the American Chemical Society* **130(1)**, 318–326.
- [62] Li, X., He, J., Hihath, J., Xu, B., Lindsay, S. M., Tao, N., et al. (2006) *J. Am. Chem. Soc* **128(6)**, 2135–2141.
- [63] Li, Z., Pobelov, I., Han, B., Wandlowski, T., Baszczyk, A., and Mayor, M. (2007) *Nanotechnology* **18(4)**, 044018.
- [64] Lide, D. R. (2008) *Handbook of Chemistry and Physics*, CRC Press, eighty-ninth edition.
- [65] De Renzi, V., Rousseau, R., Marchetto, D., Biagi, R., Scandolo, S., and delPennino, U. (2005) *Phys. Rev. Lett.* **95**, 046804.
- [66] Mangin, A., Anthore, A., Della Rocca, M. L., Boulat, E., and Lafarge, P. (2009) *Phys. Rev. B* **80**, 235432.
- [67] Meepagala, S. C. and Real, F. (1994) *Phys. Rev. B* **49**, 10761–10763.

REFERENCES

- [68] Hugelmann, M. and Schindler, W. (2003) *Surface Science* **541(1-3)**, L643–L648.
- [69] Woo, D.-H., Choi, E.-M., Yoon, Y.-H., Kim, K.-J., Jeon, I., and Kang, H. (2007) *Surface Science* **601(6)**, 1554–1559.
- [70] Schuster, R., Barth, J., Wintterlin, J., Behm, R., and Ertl, G. (1992) *Ultramicroscopy* **42(44)**, 533–540.
- [71] Haiss, W., Nichols, R. J., vanZalinge, H., Higgins, S. J., Bethell, D., and Schiffrin, D. J. (2004) *Phys. Chem. Chem. Phys.* **6**, 4330–4337.
- [72] Motte, L., Billoudet, F., and Pileni, M. P. (1995) *The Journal of Physical Chemistry* **99(44)**, 16425–16429.
- [73] Bain, C. D., Troughton, E. B., Tao, Y. T., Evall, J., Whitesides, G. M., and Nuzzo, R. G. (1989) *Journal of the American Chemical Society* **111(1)**, 321–335.
- [74] Sun, Q., Selloni, A., and Scoles, G. (2005) *ChemPhysChem* **6(9)**, 1906–1910.
- [75] Lee, M. H., Speyer, G., and Sankey, O. F. (2006) *Physica Status Solidi B* **243(9)**, 2021–2029.
- [76] Basch, H., Cohen, R., and Ratner, M. A. (2005) *Nano Letters* **5(9)**, 1668–1675.
- [77] Tomfohr, J. K. and Sankey, O. F. (2002) *Phys. Rev. B* **65**, 245105.
- [78] Müller, K.-H. (2006) *Phys. Rev. B* **73**, 045403.
- [79] McDermott, S., George, C. B., Fagas, G., Greer, J. C., and Ratner, M. A. (2009) *The Journal of Physical Chemistry C* **113(2)**, 744–750.
- [80] Paulsson, M., Krag, C., Frederiksen, T., and Brandbyge, M. (2009) *Nano Letters* **9(1)**, 117–121.

REFERENCES

- [81] Jang, S.-Y., Reddy, P., Majumdar, A., and Segalman, R. A. (2006) *Nano Letters* **6(10)**, 2362–2367.
- [82] Sek, S. (2007) *The Journal of Physical Chemistry C* **111(34)**, 12860–12865.
- [83] Engelkes, V. B., Beebe, J. M., and Frisbie, C. D. (2004) *Journal of the American Chemical Society* **126(43)**, 14287–14296.
- [84] Niskala, J., Rice, W., Bruce, R., Merkel, T., Tsui, F., and You, W. (2012) *Journal of the American Chemical Society* **134(29)**, 12072–12082.
- [85] González, M. T., Brunner, J., Huber, R., Wu, S., Schnenberger, C., and Calame, M. (2008) *New Journal of Physics* **10(6)**, 065018.
- [86] Xu, B., Xiao, X., and Tao, N. J. (2003) *Journal of the American Chemical Society* **125(52)**, 16164–16165.
- [87] Morita, T. and Lindsay, S. (2007) *Journal of the American Chemical Society* **129(23)**, 7262–7263.
- [88] Kay, N. J., Nichols, R. J., Higgins, S. J., Haiss, W., Schwarzacher, W., and Mao, B.-W. (2011) *The Journal of Physical Chemistry C* **115(43)**, 21402–21408.
- [89] Wierzbinski, E. and Slowinski, K. (2006) *Langmuir* **22(12)**, 5205–5208.
- [90] Fujihira, M., Suzuki, M., Fujii, S., and Nishikawa, A. (2006) *Phys. Chem. Chem. Phys.* **8(33)**, 3876–3884.
- [91] Nishikawa, A., Tobita, J., Kato, Y., Fujii, S., Suzuki, M., and Fujihira, M. (2007) *Nanotechnology* **18(42)**, 424005.
- [92] Akkerman, H., Blom, W., deBoer, D. M., and deBoer, B. (2006) *Nature* **441(7089)**, 69–72.
- [93] Wang, W., Lee, T., and Reed, M. A. (2003) *Phys. Rev. B* **68**, 035416.
- [94] Haiss, W., Wang, C., Grace, I., Batsanov, A., Schiffrin, D., Higgins, S., and Nichols, R. (2006) *JNat Mater* **5(12)**, 995–1002.

REFERENCES

- [95] Wang, W., Lee, T., and Reed, M. A. (2005) *Reports on Progress in Physics* **68(3)**, 523.
- [96] Wang, G., Kim, T.-W., Lee, H., and Lee, T. (2007) *Phys. Rev. B* **76**, 205320.
- [97] Cui, X. D., Primak, A., Zarate, X., Tomfohr, J., Sankey, O. F., Moore, A. L., Moore, T. A., Gust, D., Harris, G., and Lindsay, S. M. (2001) *Science* **294(5542)**, 571–574.
- [98] Haiss, W., vanZalinge, H., Bethell, D., Ulstrup, J., Schiffrin, D. J., and Nichols, R. J. (2006) *Faraday Discuss.* **131**, 253–264.
- [99] Leung, T. Y. B., Gerstenberg, M. C., Lavrich, D. J., Scoles, G., Schreiber, F., and Poirier, G. E. (2000) *Langmuir* **16(2)**, 549–561.
- [100] Kobayashi, K., Yamada, H., Horiuchi, T., and Matsushige, K. (1999) *Applied Surface Science* **144-145(0)**, 435–438.
- [101] Carro, P., Creus, A. H., Munoz, A., and Salvarezza, R. C. (2010) *Langmuir* **26(12)**, 9589–9595 PMID: 20397655.
- [102] Pires, E., Macdonald, J. E., and Elliott, M. (2013) *Nanoscale* **5**, 9397–9403.
- [103] Long, D., Lazorcik, J., Mantooth, B., Moore, M., Ratner, M., Troisi, A., Yao, Y., Ciszek, J., Tour, J., and Shashidhar, R. (2006) *Nat Mater* **5(11)**, 901–908.
- [104] Leary, E., Höbenreich, H., Higgins, S. J., vanZalinge, H., Haiss, W., Nichols, R. J., Finch, C. M., Grace, I., Lambert, C. J., McGrath, R., and Smerdon, J. (2009) *Phys. Rev. Lett.* **102**, 086801.
- [105] Xu, B. Q., Li, X. L., Xiao, X. Y., Sakaguchi, H., and Tao, N. J. (2005) *Nano Letters* **5(7)**, 1491–1495.
- [106] Peng, G., Strange, M., Thygesen, K. S., and Mavrikakis, M. (2009) *The Journal of Physical Chemistry C* **113(49)**, 20967–20973.

REFERENCES

- [107] Zhou, Y. X., Jiang, F., Chen, H., Note, R., Mizuseki, H., and Kawazoe, Y. (2007) *Phys. Rev. B* **75**, 245407.
- [108] Tang, Y.-H., Bagci, V. M. K., Chen, J.-H., and Kaun, C.-C. (2011) *The Journal of Physical Chemistry C* **115(50)**, 25105–25108.
- [109] Haiss, W., vanZalinge, H., Habenreich, H., Bethell, D., Schiffrin, D. J., Higgins, S. J., and Nichols, R. J. (2004) *Langmuir* **20(18)**, 7694–7702.
- [110] Foster, T. J., Leadbeater, M. L., Eaves, L., Henini, M., Hughes, O. H., Payling, C. A., Sheard, F. W., Simmonds, P. E., Toombs, G. A., Hill, G., and Pate, M. A. (1989) *Phys. Rev. B* **39**, 6205–6207.
- [111] Levenberg-Marquardt algorithm http://en.wikipedia.org/wiki/Levenberg-Marquardt_algorithm Accessed: 04/04/2013.
- [112] Zhang, Y., Dou, C., and Wang, Y. (2011) *Applied Surface Science* **257(15)**, 6514 – 6517.
- [113] Kaliginedi, V., Moreno-Garca, P., Valkenier, H., Hong, W., Suarez, V. M., Buitter, P., Otten, J. L. H., Hummelen, J. C., Lambert, C. J., and Wandlowski, T. (2012) *Journal of the American Chemical Society* **134(11)**, 5262–5275.
- [114] Yamada, R., Kumazawa, H., Noutoshi, T., Tanaka, S., and Tada, H. (2008) *Nano Letters* **8(4)**, 1237–1240.
- [115] Ie, Y., Endou, M., Lee, S. K., Yamada, R., Tada, H., and Aso, Y. (2011) *Angewandte Chemie International Edition* **50(50)**, 11980–11984.
- [116] Lee, S. K., Yamada, R., Tanaka, S., Chang, G. S., Asai, Y., and Tada, H. (2012) *ACS Nano* **6(6)**, 5078–5082.
- [117] Taniguchi, S.-i., Minamoto, M., Matsushita, M. M., Sugawara, T., Kawada, Y., and Bethell, D. (2006) *J. Mater. Chem.* **16**, 3459–3465.
- [118] Rattalino, I., Cauda, V., Motto, P., Limongi, T., Das, G., Razzari, L., Parenti, F., Di Fabrizio, E., Mucci, A., Schenetti, L., Piccinini, G., and Demarchi, D. (2012) *RSC Adv.* **2**, 10985–10993.

REFERENCES

- [119] Mayer, A. C., Scully, S. R., Hardin, B. E., Rowell, M. W., and McGehee, M. D. (2007) *Materials Today* **10(11)**, 28 – 33.
- [120] Lilliu, S., Agostinelli, T., Hampton, M., Pires, E., Nelson, J., and Macdonald, J. E. (2012) *Energy Procedia* **31(0)**, 60 – 68.
- [121] Lilliu, S., Agostinelli, T., Pires, E., Hampton, M., Nelson, J., and Macdonald, J. E. (2011) *Macromolecules* **44(8)**, 2725–2734.
- [122] Lilliu, S., Agostinelli, T., Verploegen, E., Pires, E., Hampton, M., Al-Hashimi, M., Heeney, M. J., Toney, M. F., Nelson, J., and Macdonald, J. E. (2011) *Macromolecular Rapid Communications* **32(18)**, 1454–1460.
- [123] Agostinelli, T., Lilliu, S., Labram, J. G., Campoy-Quiles, M., Hampton, M., Pires, E., Rawle, J., Bikondoa, O., Bradley, D. D. C., Anthopoulos, T. D., Nelson, J., and Macdonald, J. E. (2011) *Advanced Functional Materials* **21(9)**, 1701.
- [124] Agostinelli, T., Ferenczi, T. A. M., Pires, E., Foster, S., Maurano, A., Muller, C., Ballantyne, A., Hampton, M., Lilliu, S., Campoy-Quiles, M., Azimi, H., Morana, M., Bradley, D. D. C., Durrant, J., Macdonald, J. E., Stingelin, N., and Nelson, J. (2011) *Journal of Polymer Science Part B* **49(10)**, 717–724.
- [125] Guilbert, A. A. Y., Reynolds, L. X., Bruno, A., MacLachlan, A., King, S. P., Faist, M. A., Pires, E., Macdonald, J. E., Stingelin, N., Haque, S. A., and Nelson, J. (2012) *ACS Nano* **6(5)**, 3868–3875.
- [126] Arroyo, C. R., Tarkuc, S., Frisenda, R., Seldenthuis, J. S., Woerde, C. H. M., Eelkema, R., Grozema, F. C., and van derZat, H. S. J. (2013) *Angewandte Chemie International Edition* **52(11)**, 3152–3155.
- [127] Aouchiche, H. A., Djennane, S., and Boucekkine, A. (2004) *Synthetic Metals* **140(2 - 3)**, 127 – 133.
- [128] Roncali, J. (1997) *Chemical Reviews* **97(1)**, 173–206.

REFERENCES

- [129] Sedghi, G., Garcia-Suarez, V. M., Esdaile, L. J., Anderson, H. L., Lambert, C. J., Martin, S., Bethell, D., Higgins, S. J., Elliott, M., Bennett, N., Macdonald, J. E., and Nichols, R. J. (2011) *Nat Nanotechnol* **6**, 517.

Appendix A

Here is listed the Fortran code for the numerical calculation of the quantum mechanical transmission through an arbitrary one-dimensional potential barrier. The code embodies the equations outlined in Section 2.2.2.1 and was originally developed by Dr Martin Elliott, and subsequently modified by the author. A potential defined by $V(x)$ is fed from Python into the Fortran method, `tau()`, which then returns the absolute transmission for a given energy and mass, E (in eV) and μ (in units of m_e).

```
function tau(n, E, V, x, mu)

!Physical constants & variables
real (kind=8), parameter :: m_e=9.1093826e-31 !kg
real (kind=8), parameter :: q_e=1.60217653e-19 !C
real (kind=8), parameter :: hbar=1.05457168e-34 !Js
real (kind=8) :: tau, E, V(n), x(n), mu, dx, k1, k2
real (kind=8) :: alpha2(n), Pi(2,2)

!Barrier segment width
dx=(x(n)-x(1))/(n-1)

!Assume E > V in incoming and outgoing regions (travelling waves)
k1=sqrt(2*mu*(E-V(1))*(m_e*q_e/hbar**2))
k2=sqrt(2*mu*(E-V(n))*(m_e*q_e/hbar**2))

alpha2=(2*mu*(V-E)*(m_e*q_e/hbar**2))

!Start with identity matrix
```

```

Pi(1,1)=1.0; Pi(1,2)=0.0
Pi(2,1)=0.0; Pi(2,2)=1.0

do i=1,n
  Pi=matmul(Pi, KK(alpha2(i), dx))
end do

tau=4/((Pi(1,1)+Pi(2,2)*(k2/k1))**2 + (Pi(1,2)*k2-Pi(2,1)/k1)**2)

end function tau

```

The method `tau()` makes `n` calls (number of rectangular segments) upon `KK()` in order to calculate the K matrices (after Equation 2.28) for each segment. The product of these matrices is computed, allowing the transmission to be determined (after Equations 2.26 and 2.29).

```

function KK(alpha2, w)

real (kind=8) :: alpha2, w, alpha, alphaw, beta, betaw, KK(2,2)

if (alpha2 >= 0.0) then !Decaying solution ...

  alpha=sqrt(alpha2); alphaw=alpha*w
  KK(1,1)=cosh(alphaw)

  if (abs(alpha) < 1e-20) then
    KK(1,2)=-1.0*w
  else
    KK(1,2)=-sinh(alphaw)/alpha
  endif

  KK(2,1)=alpha2*KK(1,2); KK(2,2)=KK(1,1)

else !Propagating solution ...

  beta=sqrt(-alpha2); betaw=beta*w

```

```
KK(1,1)=cos(beta*w)

if (abs(beta)<1e-20) then
    KK(1,2)=-1.0*w
else
    KK(1,2)=-sin(beta*w)/beta
endif

KK(2,1)=alpha2*KK(1,2); KK(2,2)=KK(1,1)

endif

end function KK
```

If the computation is repeated for different energies, then the resultant transmission function, $T(E)$, can be integrated in accordance with the Landauer equation (Equation 2.13) to calculate the $I(V)$ characteristics for the system.

Appendix B

Preliminary single molecule conductance measurements under ultra high vacuum were performed on the porphyrin dimer, 2LE099; the structure of which is shown in Figure 1.

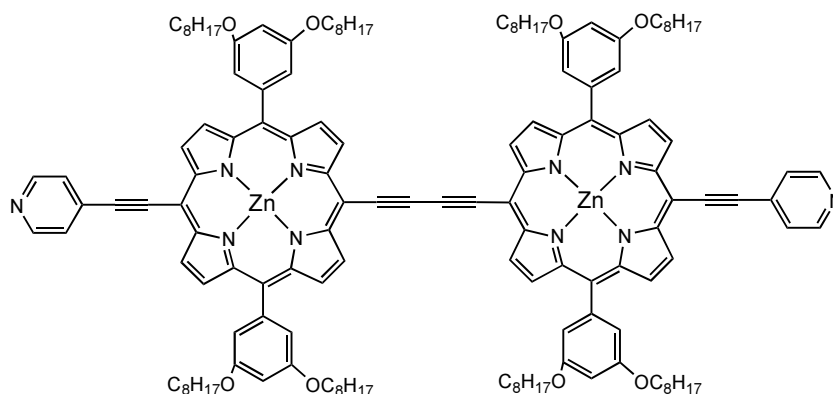


Figure 1: Structural diagram of the 2LE099 porphyrin dimer. Pyridyl anchoring groups are present instead of the more commonly used thiol groups.

The investigations on this species were not thorough and little information can be extracted from the data. However, one conductance group was isolated over the bias range ± 0.3 V; the key attributes of which are presented in Figure 2. Interestingly, despite a molecular length of roughly 3 – 4 nm, Figure 2b suggests an average break off distance of roughly 1.7 nm. Thus, it is likely that the conductance group in question corresponds to transport across only one porphine unit.

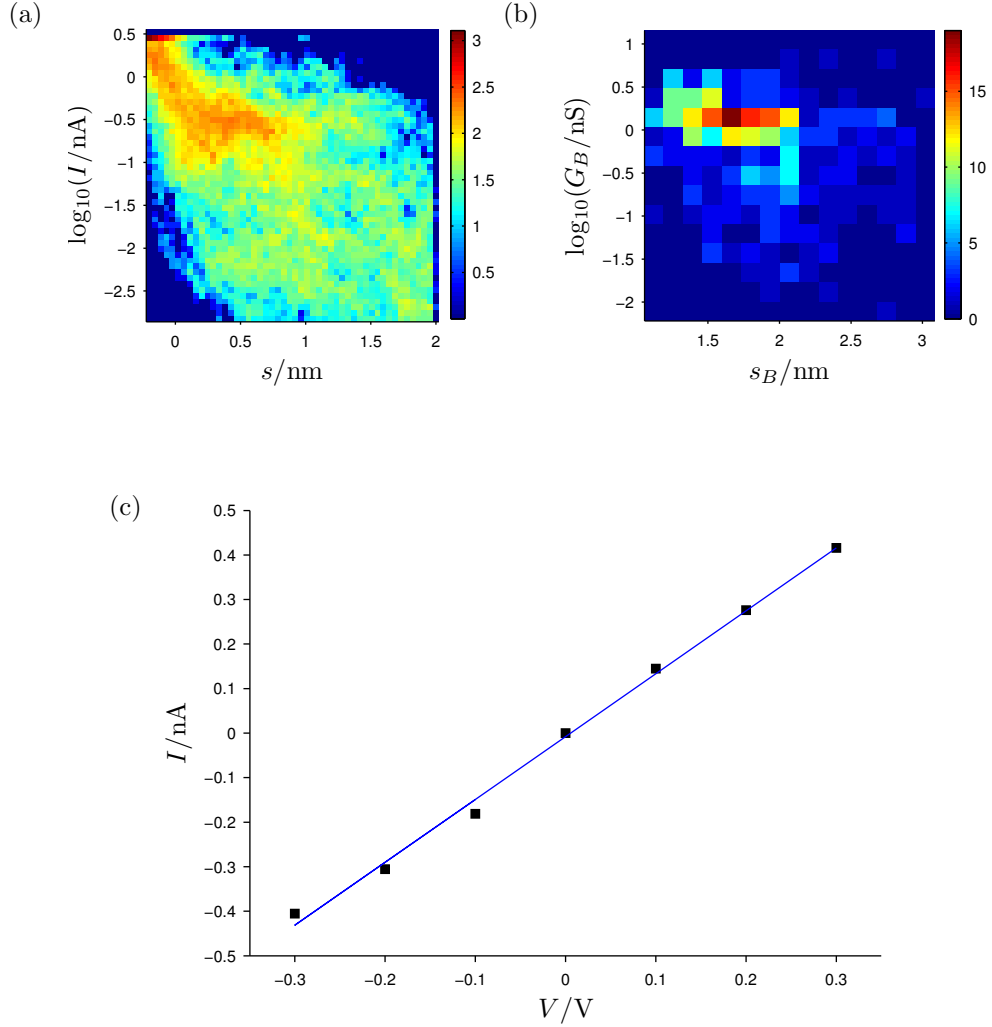


Figure 2: a) An example $I(s)$ data set after filtering for current plateaus, measured with a tip bias of -0.2 V. b) Plot of conductance against distance at the point of molecular break off *i.e.* the end point of a current plateau, comprising data from approximately 400 curves measured with tip biases between -0.3 and $+0.3$ V. Absolute tip-sample separations were calculated using Equation 3.1 with a measured decay constant of 10.8 nm^{-1} . c) The $I(V)$ characteristics for the conductance group in a) and b), determined by reading the position of histogram peaks at different biases. (Zero current is assumed for the zero bias data point.) The gradient of the linear fit is $(1.41 \pm 0.03) \text{ nS}$.